Physical and Chemical Sciences Center

Research Briefs

January 1999

Sandia National Laboratories
Albuquerque, New Mexico

A Department of Energy Multiprogram Laboratory

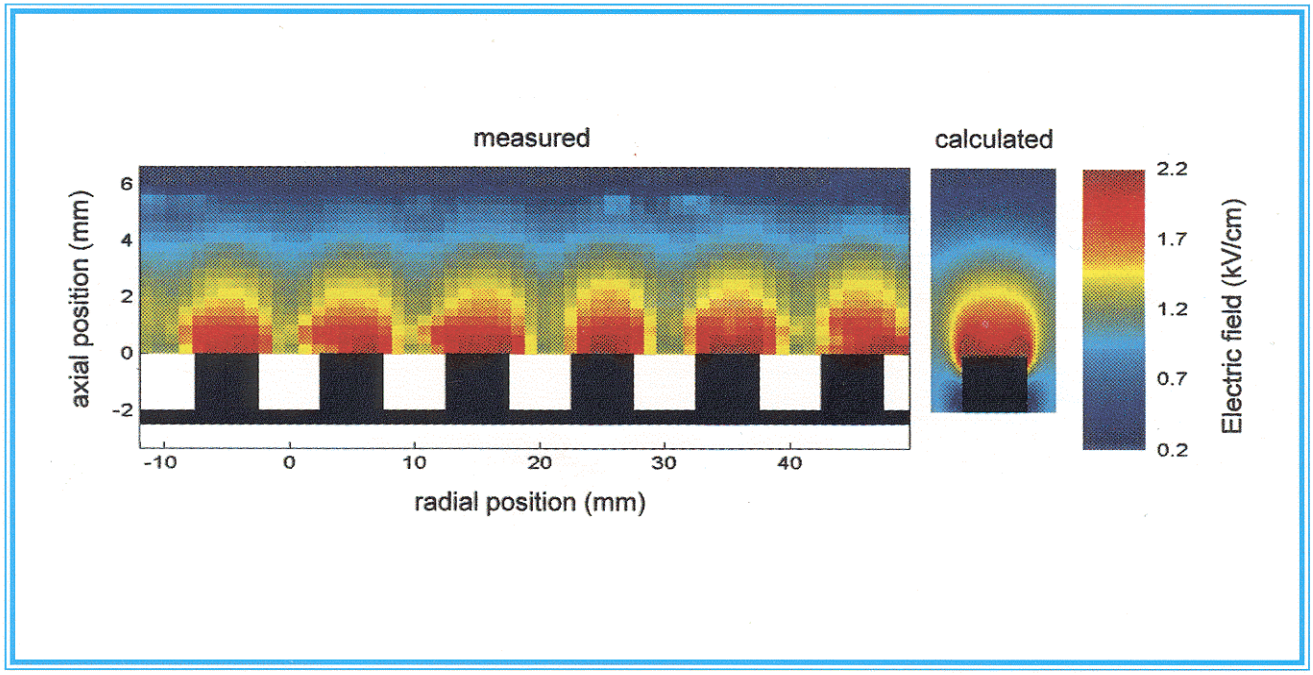

Research Briefs for the Physical and Chemical Sciences Center is published by Sandia National Laboratories. Additional complimentary copies are available by contacting:

S. Tom Picraux
Physical and Chemical Sciences Center, 1100
Sandia National Laboratories
Albuquerque, NM 87185-1427

Phone: (505) 844-7681
Fax: (505) 844-6098
E-mail: picraux@sandia.gov
url: http://www.sandia.gov/1100/1100hp.htm

Research Briefs

Editors
S. T. Picraux
J. A. Nichelason

Production
Bernadette Fulton

Cover Page: Magnitude of the electric field strength above an aluminum grooved electrode (see page 75).

Message from the Director

The Physical and Chemical Sciences Center provides new scientific knowledge in support of Sandia's missions for the Department of Energy. We emphasize research to create and enable emerging technologies. We also provide new understanding needed to support predictive reliability for existing systems. The focus of our work derives from Sandia's role as a multiprogram laboratory with broad-based research and development responsibilities for nuclear weapons, nonproliferation, energy, environment and other areas of importance to the nation.

Within our portfolio of research investments, this issue of Research Briefs highlights our recent accomplishments supporting longer term/exploratory activities. We address a focused set of strategic themes: science underlying materials performance and reliability, nanoscale structures and devices, advanced sensing science, and the science of semiconductor technologies. We employ a wide range of multidisciplinary capabilities based on the physical and chemical sciences, from first principles modeling and atomic scale measurement to remote laser sensing and the science of complex adaptive behavior. Looking to the future, we are investing in the science that underlies future generations of integrated microsystems, and the microscopic-based physical models needed for predictive reliability of systems in a new era of teraflop computing.

The activities of the Physical and Chemical Sciences Center are supported by a diverse set of funding sources, and are managed to assure integration and synergy between projects. The research described here provides examples that illustrate the importance of a strong science base in physics and chemistry to the success of DOE's Stockpile Stewardship mission. This work also provides insights into the connections between science and the wide range of DOE technologies. In essentially all the research described, our partnerships with colleagues in universities, industry, and in program areas across the Labs have been critical, and we acknowledge with gratitude their collaboration.

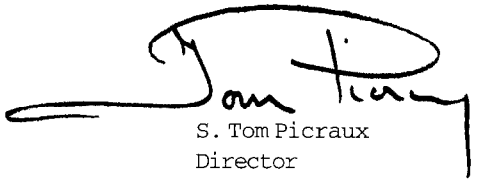

S. Tom Picraux
Director

Table of Contents

Science Base for Enhanced Materials Performance and Reliability

Nanoscale Materials Science

Advanced Sensing Science

Science of Semiconductor Technologies

Science Base for Enhanced Materials Performance and Reliability

Simultaneous Measurement of Friction and Adhesion

A. R. Burns, J. E. Houston, R. W. Carpick, and T. A. Michalske

Motivation--As mechanical devices shrink to ever smaller dimensions, their performance and reliability increasingly depend on the nanoscale characteristics of the contacting surfaces. Modification of the surfaces with "lubricant" monolayers of long-chain alkanes is now integrated into the release step of microelectromechanical (MEMS) devices. Our program is designed to obtain molecular-level information on friction and adhesion so that we can understand both dynamical and chemical factors of energy dissipation.

Accomplishment--With a novel scanning probe microscope, we have been able to observe the onset of friction forces and attractive (adhesive) forces simultaneously. As shown in Fig. 1, friction is monitored by measuring the vibrational amplitude of an oscillating glass probe tip which has a diameter <100 nm. Lateral shear forces at the tip/sample contact will dampen the vibrational amplitude. A mechanically-stable interfacial force microscope (IFM) sensor is used to measure normal forces at the tip independently and decoupled from the lateral forces, allowing one to observe friction from the early stages of the purely attractive regime to the latter stage of repulsive compression. Measurements on model lubricant silane and alkanethiol self-assembled monolayers indicate that friction dramatically increases with the strength of attractive interactions between the tip and the monolayers. These interactions result in significant energy losses due to the tensile deformation of the lubricant chains, collective chain motion, and dissipative bond breaking.

A highly schematic depiction of the tip's interaction with a molecular monolayer is shown in Fig. 2. When the tip initially approaches the film, there are attractive forces which result in tensile deformation (left). The tip will eventually compresses the film under repulsive forces (right). The relative importance of the attractive forces in creating friction is due to the strength of the chemical bonding between the tail groups on the end of the chains and the tip. Strong bonding results in large energy dissipation due to the collective motion of the chains and dissipative processes during bond rupture. Weak bonding has little effect and most of the friction is due to compression of the film under higher loads. Modeling of the friction-normal force relation within the formalism of continuum mechanics allows us to see that the tip-surface interaction can be understood as a single asperity contact, and it allows us to quantify the work of adhesion and shear stress. However, limitations to the model due to finite-range attractive forces and modes of deformation unique to molecular films will require future study.

Significance--We have shown that the molecular origins of friction can be examined in detail with a novel instrument which allows the complete adhesive interaction between tip and surface to be examined. Correlation of normal forces with lateral shear forces reveals both the adhesive and repulsive nature of friction between the contacting surfaces. An important insight gained from the initial experiments on self-assembled model lubricants is the significant friction, which steeply increases with attractive forces, that must be attributed to tensile molecular deformation, collective molecular chain motion, and dissipative bond ruptures.

Sponsors for various phases of this work include: LDRD
Contact: Alan R. Burns, Surface and Interface Sciences Dept., 1114
Phone: (505) 844-9642, Fax: (505) 844-5470, E-mail: aburns@sandia.gov

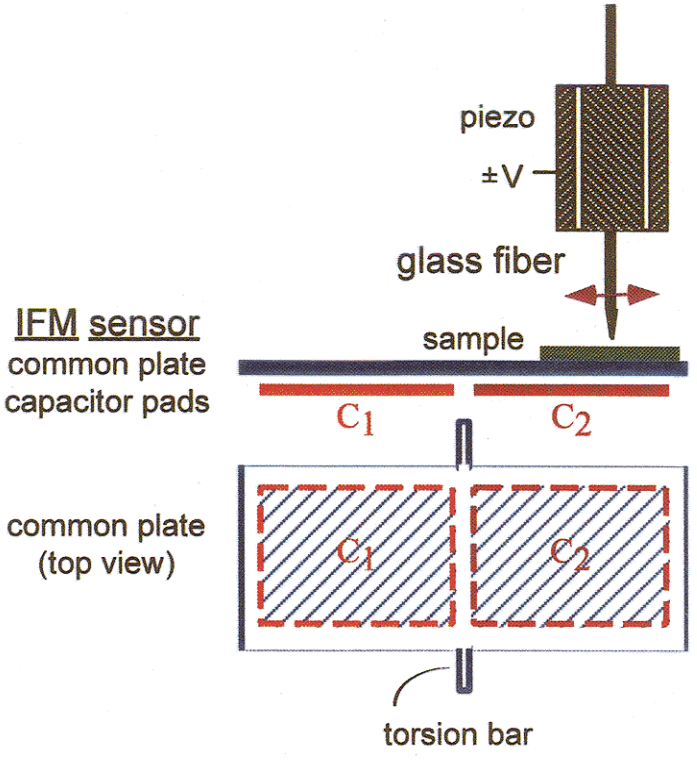

Figure 1. A vibrating glass fiber with a tip diameter <100 nm is brought into contact with a sample resting on an IFM sensor. The sensor measures the attractive and repulsive forces by maintaining an electrostatic balance between two capacitances C_1 and C_2.

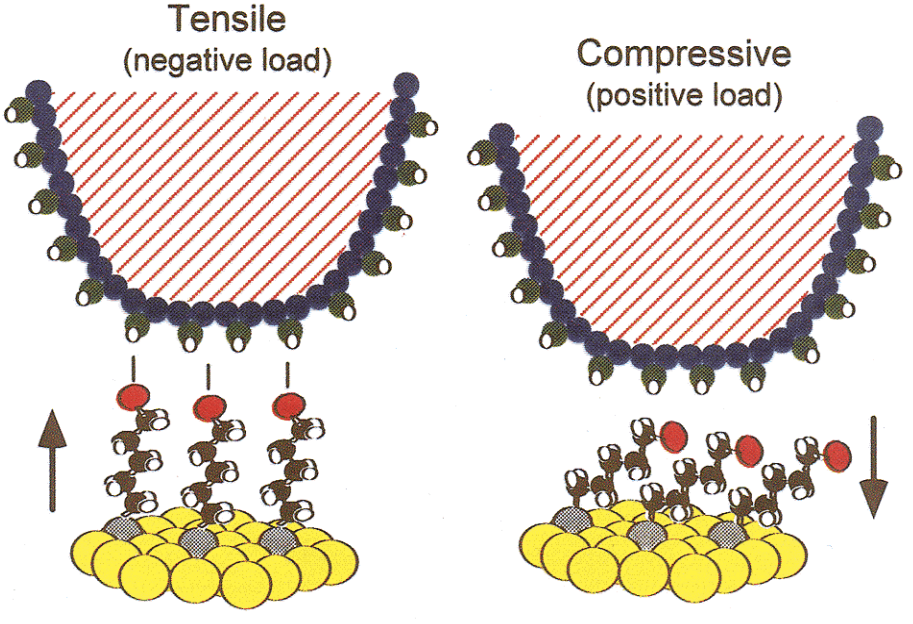

Figure 2. Representation (not to scale) of glass tip interaction with molecular lubricants anchored to substrate. They will undergo tensile deformation under attractive forces (negative loads at left), and compression under repulsive forces (positive loads at right). The tensile stress is directly related to the strength of the attractive forces due to chemical bonding.

Corrosion Behavior of Plasma-Passivated Copper

J. C. Barbour, J. W. Braithwaite, K. -A. Son, N. Missert, J. P. Sullivan, N. R. Sorenson, J. S. Nelson, and W. G. Breiland

Motivation--Predictive understanding of corrosion is needed to ensure reliability in both electronics and microelectronics components. To date, modeling has been hindered by limited knowledge of primary corrosion mechanisms and the large number of coupled chemical reactions which depend on complex interactions of materials with environment. This multi-dimensional problem requires new approaches for quantitative identification of critical phenomena occurring in corrosion phase space. We are examining combinatorial techniques as a first step toward developing these new experimental approaches and determining mechanisms critical to copper sulfidation.

Accomplishment--Parallel experimentation was used in which the thickness of Cu oxide and the level of irradiation-induced defects were varied to efficiently identify mechanisms for Cu sulfidation. This work specifically examined accelerated aging of Cu for 5.5 hrs. in a 65% relative humidity air environment containing 600 ppb H_2S as the sulfidizing agent. A Cu film was deposited on an SiO_2 covered Si wafer and then masked and oxidized in an electron cyclotron resonance (ECR) plasma to form different thicknesses of CuO_x on Cu. The sample was then implanted with 200 keV Cu^+ ions with different fluences to create different levels of point defects in the oxide and Cu. A schematic representation of this combinatorial matrix experiment is shown in Fig. 1. A 200 keV Cu^+ ion beam was used because the projected range was large enough (~60 nm) to minimize the amount of Cu coming to rest in the oxide layer and to eliminate possible doping effects in the Cu layer. Also, a control sample was deposited and exposed to air to form a native oxide, and then exposed to the H_2S environment. The air-oxidized sample begins corroding after only 0.5 hrs., and showed the greatest amount of Cu_2S formation. Figure 2 shows portions of the combinatorial sample exposed to $1x10^{12}$ Cu/cm^2, $1x10^{13}$ Cu/cm^2, and $1x10^{14}$ Cu/cm^2. The variation in oxide thickness had little effect on the formation of and quantity of Cu_2S, while the level of irradiation affected the Cu_2S formation greatly. The as-grown ECR-passivated Cu showed no signs of corrosion, even after 24 hours in this aggressive corrosion environment. For fluences greater than $1x10^{12}$ Cu/cm^2, the sample forms a Cu_2S layer on top of a Cu_2O layer. This fluence corresponds to a point defect level of 0.002 vacancies/atom in Cu_2O. Analysis showed that the surface of ECR-passivated Cu is $CuO/Cu_2O/Cu$. This structure is corrosion resistant until broken or penetrated, such as by ion irradiation. Air oxidized Cu is predominantly Cu_2O with a small quantity of CuO. This structure, with Cu_2O at the exposed surface, is not corrosion resistant.

Significance--For the first time, a Cu film with an undamaged oxide surface prevented sulfidation in H_2S. The plasma-oxidized Cu yields a surface which is more resistant to sulfidation than an air-oxidized Cu, thus providing a means to treat Cu for minimizing corrosion in sulfidizing environments. Further, the results of this experiment show that the type of Cu-oxide (CuO vs. Cu_2O) and defect level in oxide are more important for controlling the sulfidation reaction than is the oxide thickness. These results suggest that either defects in CuO enable Cu diffusion through CuO to drive the reaction between Cu and H_2S at the surface, or irradiation reduces the oxidation state of Cu^{++} in CuO to allow sulfidation.

Sponsors for various phases of this work include: DP - Phys. Sci. & Tech., BES
Contact: J. Charles Barbour, Radiation Solid Interactions and Processing Dept., 1111
Phone: (505) 844-5517, Fax: (505) 844-7775, E-mail: jcbarbo@sandia.gov

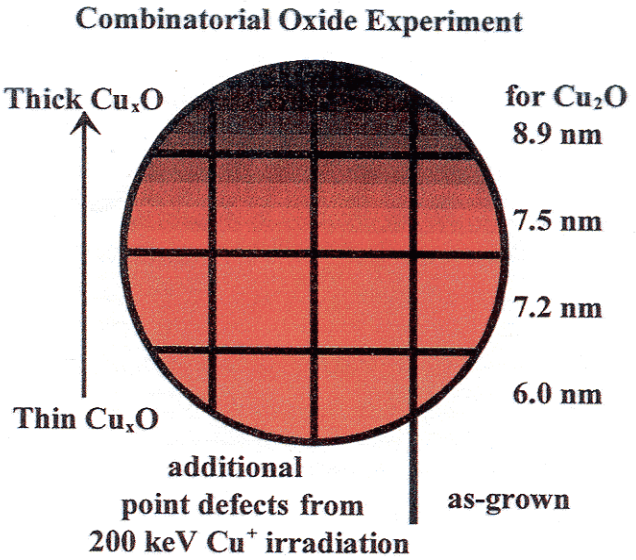

Figure 1. Schematic depiction of the sample geometry for a combinatorial experiment in which the parameters of copper oxide thickness and defect density are varied.

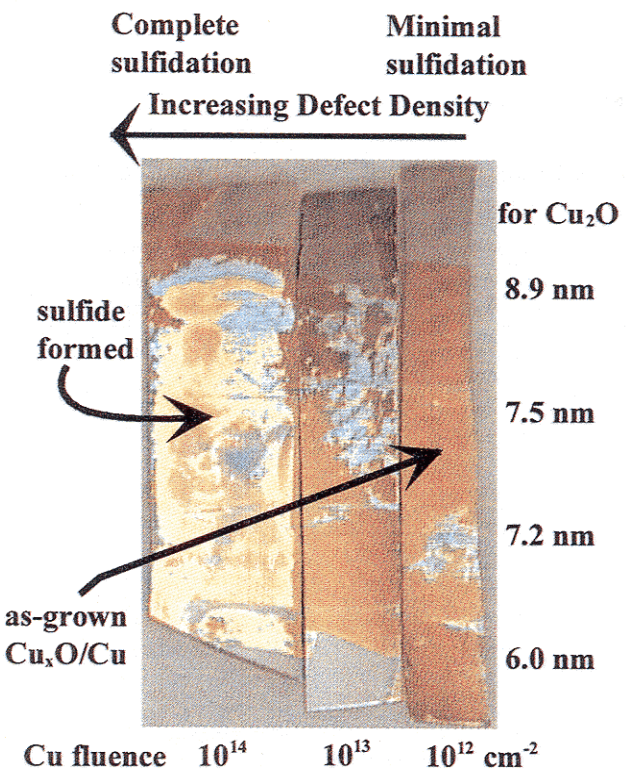

Figure 2. Results of the combinatorial matrix depicted in Fig. 1. The as-grown oxide exhibited no corrosion and so it is not shown in this figure. The level of corrosion product increases with Cu-ion irradiation fluence, and changes only slightly as a function of oxide thickness.

Extreme Strengthening of Ni Surfaces by Al_2O_3 Nanoparticles Introduced Through Ion Implantation

*S. M. Myers, D. M. Follstaedt, J. A. Knapp, and G. A. Petersen**

Motivation--Theoretical consideration of plastic deformation in Ni indicates that levels of strength well beyond those realized by current metallurgical processing might be attained without loss of ductility by introducing a dense dispersion of very small hard particles to impede dislocation motion. Ion implantation provides a means of manipulating microstructure on the nanometer scale at depths up to ~1 μm, while micromechanical testing allows the elastic and plastic properties of the treated zone to be quantified. In this study, the possibility of extreme dispersion strengthening of Ni was explored by using ion implantation of Al and O to form nanometer-size precipitates of Al_2O_3 at volume fractions exceeding 10%. Motivations included testing of the theory of dispersion hardening in the regime of extreme particle refinement, exploring the limits of strength in Ni, and surface hardening of Ni components in micro-electromechanical systems.

Accomplishment--Room-temperature ion implantation of Al and O at multiple energies produced an approximately 200-nm-thick layer containing Al_2O_3 particles with a size of ~2 nm at a volume fraction of about 13%. The Al_2O_3 particles appear thermally stable, remaining virtually unchanged after annealing at 550°C. The microstructure is seen in the cross-section transmission-electron-microscope image of Fig. 1, where a condition of slight underfocus causes the less-dense oxide inclusions to appear as light features. The mechanical properties of the implanted region were evaluated by nanoindentation testing. A pyramidal diamond indenter impinged to a depth of 160 nm with force being measured as a function of position. Resulting data were analyzed by using finite-element modeling to describe the combined response of the hardened layer and the much softer substrate, thereby revealing the intrinsic elastic and plastic properties of the particle-containing layer. Young's elastic modulus remained comparable to that of untreated Ni, increasing from about 210 to 270 GPa. Yield strength was more greatly affected, going from about 0.15 to 4.9 GPa.

The above increase can be understood in terms of oxide-particle blocking of dislocation motion during plastic flow. Indeed, application to the observed microstructure of a published formula for dispersion hardening by spherical hard particles yields an estimated resolved flow stress of ~5 GPa, consistent with the above experimental value. In Fig. 2, the yield strength of the Ni(Al_2O_3) matrix is compared to those of untreated Ni and a hard bearing steel, Type 440C; the exceptional strengthening effect of the nanoparticle dispersion is evident. The yield strength obtained above is comparable to that previously reported by us for amorphous Ni(Ti,C), where the hardening effect of structural disorder is believed to be augmented by Ti-C atomic pairing. A further important finding is that the hardened Ni(Al_2O_3) layer retained substantial ductility, as evidenced by the absence of cracking or decohesion under severe deformation by a diamond probe.

Significance--This work shows that the strength of Ni can be extended to at least 5 GPa with retention of ductility through nanoparticle dispersion hardening. The implantation hardening demonstrated here may enhance the performance and lifetime of micro-electromechanical systems constructed from Ni.

*In collaboration with Sandia National Laboratories Orgs. 1832 and 2643

Sponsors for various phases of this work include: BES, DP - Phys. Sci. & Tech., LDRD

Contact: Sam M. Myers, Nanostructure & Semiconductor Physics Dept., 1112
Phone: (505) 844-6076, Fax: (505) 844-7775, E-mail: smmyers@sandia.gov

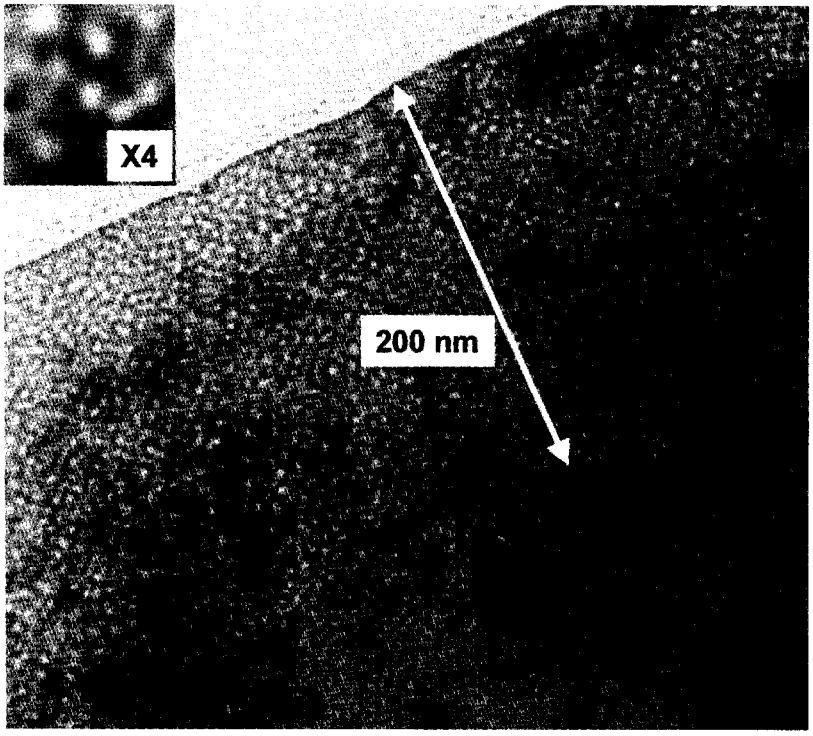

Figure 1. Cross-section transmission-electron micrograph showing Al_2O_3 nanoparticles in Ni implanted with Al and O and annealed at 550°C.

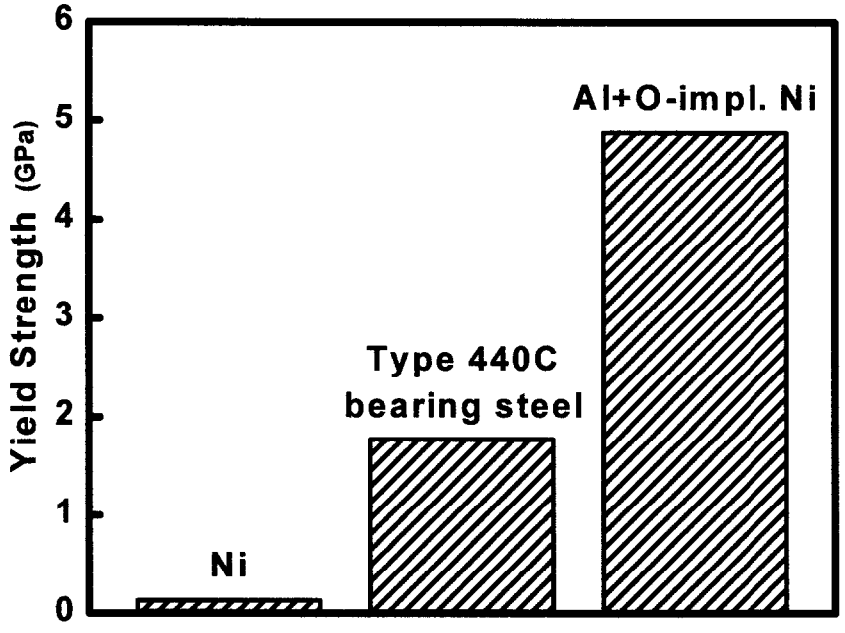

Figure 2. Intrinsic yield strength of Al+O-implanted Ni compared with untreated Ni and with Type-440C hard bearing steel.

Micromachine Adhesion in Humid Environments

*T. A. Michalske**

Motivation--(Micro-electromechanical Systems) or MEMS are now being used in selected commercial products and are being considered for many other device designs and applications. However, auto-adhesion, or spontaneous sticking between MEMS structures is known to limit manufacturing yield and reliability of this new class of engineering devices. In many applications, the MEMS structures will be exposed to ambient conditions and it is important to understand how interactions with the surrounding environment will influence MEMS performance. In this study we use MEMS test structures to directly measure adhesion energies and stiction as a function of the ambient humidity.

Accomplishment--We characterized in-situ the adhesion of surface micromachined polysilicon beams subject to controlled humidity ambients. Singly supported beams were made free using a wet chemical etch followed by supercritical CO_2 drying. Beams of various lengths were fabricated with an electrostatic actuation pad that was used to pull the freed beams into contact with the substrate. We equiped our electrical probe station with an optical interference microscope so that we could measure beam deformations and determine the adhered length of beams that remained attached to the substrate after the electrostatic actuation was removed. Our probe station also incorporated a gas flow system that allowed us to actively control the relative humidity (RH) during adhesion testing. The adhered length of beams was then used to calculate an adhesion energy using a previouly developed mechanics analysis. Our data indicates that adhesion energies increased exponentially with RH from 30% to 95%, giving values that ranged from 1 mJ/m^2 to 50 mJ/m^2. Figure 1 shows the increasing adhesion length associated with increasing humidity. We used the Kelvin equation to model these results assuming both smooth and rough beam surfaces. We showed that the adhesion energy should be independent of RH for a smooth beam/substrate interface. This prediction is consistent with the adhesion of atomically smooth mica surfaces. Alternatively, a model that takes into account finite surface roughness predicts an exponential increase in adhesion with increasing humidity. By modeling a rough interface as a collection of independent asperities consistent with atomic force microscopy data (~2.0 nm rms roughness) for our beam surfaces, the exponential trend was satisfactorily explained (see Fig. 2).

Significance--Our ability to use MEMS devices in high consequence defense and national security applications will depend greatly on our understanding and control of factors that influence their reliable performance. Since surface forces play such an important role in the performance of miniaturized mechanical structures, we must be able to accurately model and predict phenomenon such as stiction, adhesion and friction. This study demonstrates the importance of the nanometer scale surface topography on fundamental adhesion processes in MEMS devices. These understandings allow us to better predict how MEMS devices will perform in various operating conditions which may in the futureinclude not only ambient humidity but also corrosive chemicals.

*In collaboration with Org. 1725

Sponsors for various phases of this work include: DP - Phys. Sci. & Tech., BES, LDRD

Contact: Terry A. Michalske, Surface and Interface Science Dept., 1114
Phone: (505) 844-5829, Fax: (505) 844-5470, E-mail: tamicha@sandia.gov

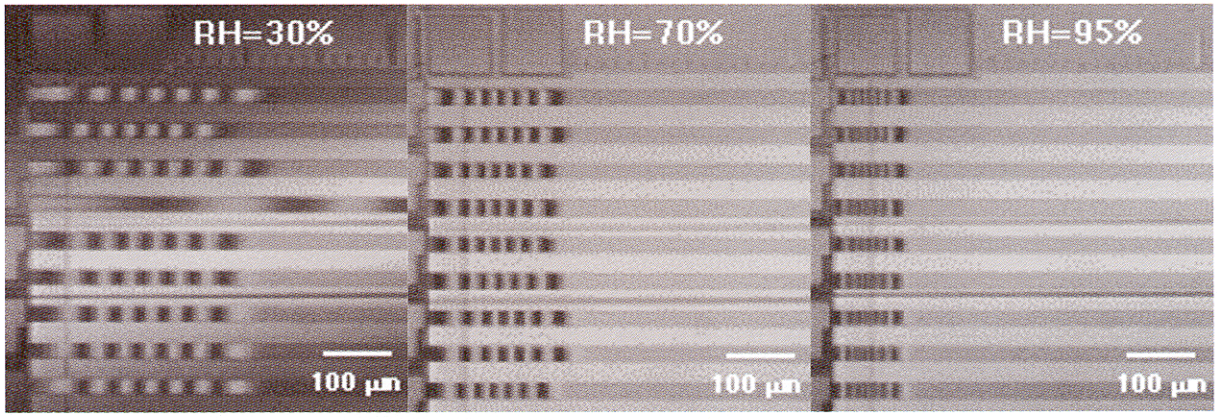

Figure 1. Adhesion of polysilicon micromachined beams at differing relative humidities. Increased adhesion is indicated by compression of the optical interference fringe pattern on the left side of each array of beams.

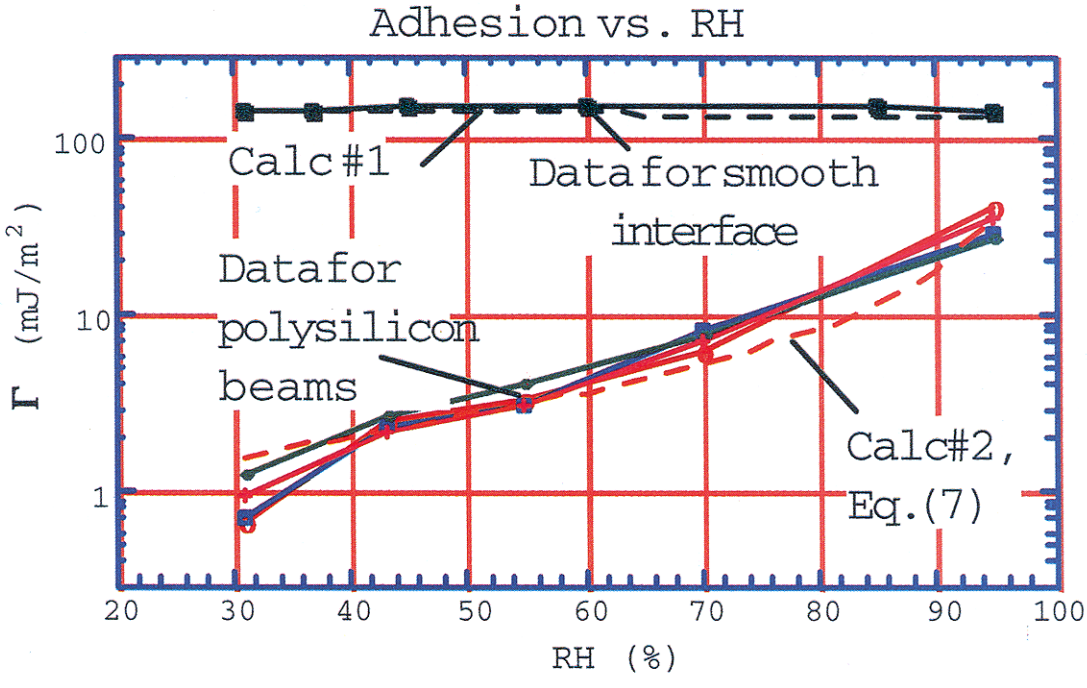

Figure 2. Comparison of calculated and measured values of adhesion energy as a function of relative humidity. Calculated values for smooth interfaces (Cal #1) and for rough interfaces (Cal #2) are compared with measured values for cleaved mica interfaces and polysilicon beams respectively.

Growth Strategies for Reducing Defects in Gallium Nitride

M. E. Bartram, M. E. Cotrin, J. Han, C. C. Willan, M. H. Crawford, N. Missert, J. J. Figiel, A. G. Baca

Motivation--Recent advances in chemical vapor deposition (CVD) techniques for growing gallium nitride (GaN) based materials have finally provided a solid state device capable of emitting blue light. This critical advance in providing the last primary color needed to produce the full visible spectrum has opened the doors to a vast number of important commercial applications. Examples include vertical cavity surface emitting lasers, high density flat panel displays, traffic lights, microsensors, and high density storage devices.

Improvements in the light emitting properties have been achieved by reducing the defect density in GaN materials with a technique known as selective area growth (SAG). As shown in Fig. 1 (A-D), this method uses inert masking materials to confine nucleation to specific regions (A). This directs growth to proceed from a limited number of "seed crystals" on the surface (B). The lateral growth which results, lessens the detrimental effects of the lattice mismatch between GaN and the underlying substrate (C). Unfortunately, defects are formed at the convergence lines due to growth front mismatch. In addition, defects in the nucleation regions continue to propagate vertically, as the film thickness increases (D). Both of these effects reduce the quality of the luminescence. Our approach is to optimize this method and extend the approach into more versatile growth strategies for improved GaN materials.

Accomplishment--We have exploited growth conditions in a manner which reduces nucleation zone defects and growth front mismatch convergence defects in SAG based GaN CVD. As shown in Fig. 2 (E-H), the proper combination of deposition temperature and flow rates of reactants to the surface results in growth features having sloped sides (E). Upon convergence of the growth fronts (F), nucleation of a second growth mode is stimulated from a single point and proceeds vertically layer by layer (G). This appears to occur at a rate accelerated relative to the initial lateral/vertical growth. This overtakes the propagation of the initial growth features and results in coalescence with reduced defects (H).

Significance--Although the growth strategy and the quality of our films is not yet fully optimized, the uniform luminescence obtained from GaN grown in this manner suggests that defect lines normally associated with SAG based CVD are reduced substantially with this method. This demonstrates that we have increased both the useful area on the GaN surface for constructing devices and the overall materials quality. Precedents showing that initial nucleation features can be grown in a triangular fashion suggest that the propagation of nucleation defects can be terminated fully. This will be tested as a further refinement of our approach in future work.

In addition, related aspects of these studies are key steps in establishing the materials science of GaN. These include an understanding of growth modes, the stability of crystal faces, real-time growth rate measurements for constructing kinetics models of the deposition process and morphology evolution, and new masks for implementing SAG strageties in more complex GaN alloys such as AlGaN.

Sponsors for various phases of this work include: BES, DP - Phys. Sci. & Tech., LDRD
Contact: Michael E. Bartram, Chemical Processing Sciences Dept., 1126
Phone: (505) 844-1619, Fax: (505) 844-3211, E-mail: mebartr@sandia.gov

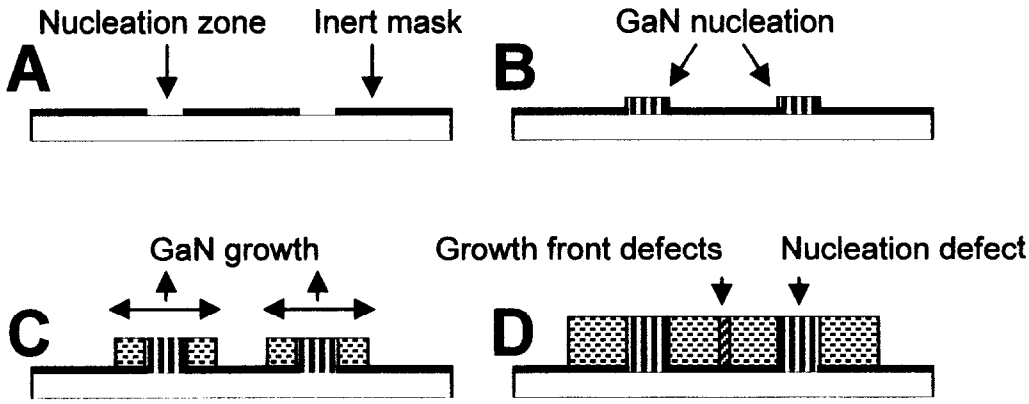

Figure 1. Chemical vapor deposition (CVD) of GaN using selective area growth (SAG), proceeding through steps "A" to "D".

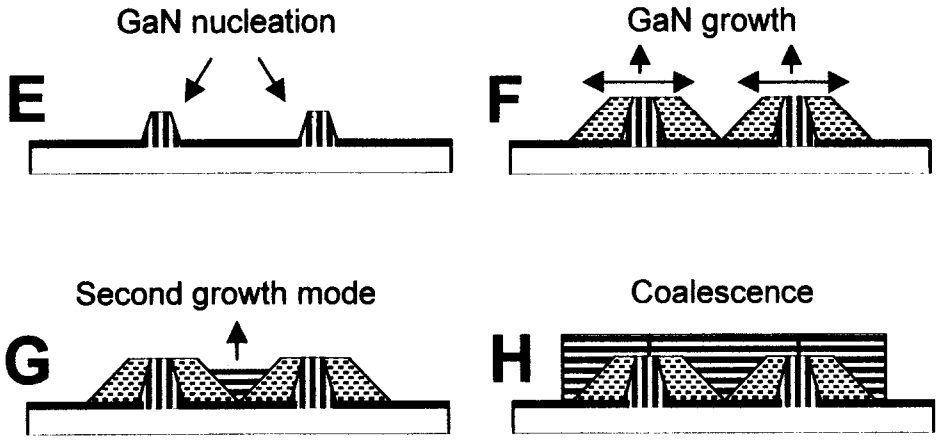

Figure 2. SAG using conditions which promote a second growth mode for GaN. Coalescence results in a film with reduced defect densities. (Proceeding through steps "E" to "H")

Electric Field Control of Phosphor Efficiency at Low Electron Energies

C. H. Seager

Motivation--With the maturing of field emission tip arrays for the production of energetic electrons under cold cathode conditions, the use of these arrays for flat panel displays has received increasing attention. Ideally, these displays would be used to excite phosphors at low electron energies. However, essentially all phosphors now used for conventional cathode ray tubes become increasingly inefficient as electron energies are reduced below 5 keV. It is generally accepted that lower energy electrons, because of their short penetration distances, allow excited electron-hole pairs to access surface or near-surface defects. This results in non-radiative de-excitation losses and low light output. However to date, there has been no demonstration that these losses can be explained in a detailed fashion or experimentally modified by the manipulation of the cathodoluminescence (CL) measurement conditions.

Accomplishment--We have developed a method for applying an electric field internal to phosphors which affects large changes in the CL efficiency. Conventional methods for accomplishing this, which include evaporated metal electrodes, are unsuitable for impressing fields on phosphor powders. Metal films thick enough to cover our phosphor screens would be too thick to permit electron beam penetration at the energies of interest. The technique we have developed involves pressing a thin metal mesh over the phosphor screen; electrons penetrate through the holes in the mesh and excite the phosphor while the electric field is established by impressing a voltage between the mesh and the metal screen backing plate. Because the holes in the mesh are considerably smaller than the thickness of the phosphor layer, the electric field remains largely internal to the phosphor, and effects on the arriving electrons before they reach the phosphor surface are negligibly small. We find that these impressed electric fields produce large changes in phosphor efficiency. In fact, the brightness of some phosphors can be altered over a two decade range with this effect. We also see that after the initial application of the field, the changes of brightness decay with a time constant of the order of 0.05-0.4 secs. This time constant depends on both the magnitude of the impressed electric field and on the electron beam energy and current density. The decay of the field effect is caused by polarization of the e-beam-created electron-hole pairs; this polarization eventually cancels the internal electric field, leaving the CL output at its zero-field value. The size and beam energy dependence of the CL brightness changes can be understood as the effect of the electric field in changing the population of beam-created electrons and holes at the surface non-radiative loss sites; this alters the recombination rate at these sites.

Significance--This technique has opened new opportunities for studying non-radiative surface losses in phosphors. Several features of the experimental results have already challenged our present understanding of this process, and more sophisticated experiments of this type are expected to shed new light on the nature of these losses.The eventual goal of this program is to develop phosphors which have surface losses much lower than those available at present. In addition, it is possible that the present technique can be directly applied to improving the brightness of field effect displays. A patent disclosure has been filed which describes how this might be accomplished.

Sponsors for various phases of this work include: DARPA
Contact: Carleton H. Seager, Radiation Solid Interactions and Processing Dept., 1111
Phone: (505) 844-9168, Fax: (505) 844-1197, E-mail: chseage@sandia.gov

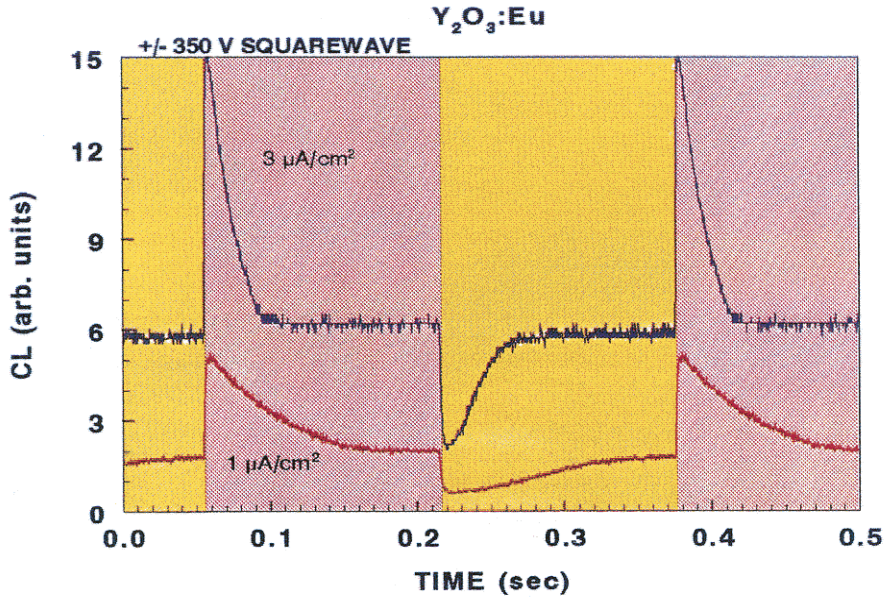

Figure 1. The time dependence of cathodoluminescence for europium doped yttria at two different electron beam currents during the application of +/- 350V voltage pulses across the phosphor layer. At the start of the positive bias part of the voltage cycle (pink), the CL is enhanced, and at the start of the negative half of the cycle (yellow) the CL is reduced. The decay of the effect is due to the build-up of polarization in the phosphor; this happens more rapidly as the beam current is increased.

The Properties and Physics of the Slim-Loop Ferroelectric (SFE) $(Pb_{.71}Ba_{.29})_{.99}(Zr_{.707}Ti_{.293})_{.98}Bi_{.02}O_3$, (PBZT-Bi)

*G. A. Samara and L. V. Hansen**

Motivation--Complex mixed oxides based on $Pb(Zr_{1-x}Ti_x)O_3$, or PZT, find several applications in Sandia components. One such material based on $Pb(Zr_{.70}Ti_{.30})O_3$, is PBZT-Bi which is used in explosively-driven pulsed power sources. The substitution of Ba^{2+} for Pb^{2+} ions and the addition of a small amount of Bi impart unto this material slim loop ferroelectric (SFE) character and properties qualitatively different from those of PZTs and other normal ferroelectrics. These properties had not been studied in any detail and the physics was not understood before this work.

Accomplishment--The combined effects of temperature, hydrostatic pressure, frequency, and dc biasing fields on the electrical properties were investigated along with complementary differential scanning calorimetry, x-ray diffraction and TEM measurements. Highlights of the work include: (1) The dielectric measurements at 1 bar reveal the relaxor ferroelectric nature of this material which is qualitatively different from normal ferroelectric behavior (Fig. 1). Consistent with this finding, there is no structural phase transition across the frequency-dependent peak in the dielectric constant ε' vs. temperature. This peak defines the dynamic glass transition temperature, T_m. (2) Evidence is found for the existence of polar nano-domains at temperatures much higher than T_m. This evidence comes from analysis of the thermal expansion data and the deviation of $\varepsilon'(T)$ from a Curie-Weiss law. (3) By attributing the continuous deviation of the thermal expansion from its high temperature behavior to electrostriction, we calculated the temperature dependence of the local dipolar polarization of the nano-domains (Fig. 2). The results are in agreement with the measured polarization at high fields and make it possible to interpret the field dependence of the measured polarization. (4) The deviation of $\varepsilon'(T)$ from a Curie-Weiss law above T_m is attributed to correlations among the polar nano-domains resulting in the formation of local order. The temperature dependence of the local order parameter was calculated. (5) Analysis of the dielectric data provides a detailed view of the dynamics and energetics of the relaxational response of the polarization. The dipolar relaxation time obeys a Vogel-Fulcher equation. The parameters of this equation and their pressure dependences were determined and understood in terms of the physics. (6) Pressure strengthens the relaxor character of the response resulting in suppression of $\varepsilon'(T)$ and of T_m (Fig. 3). These effects can be understood in terms of a reduction with pressure in the correlation length for the interaction of polar nano-domains. (7) The relaxor behavior of PBZT-Bi results from the lattice disorder produced by the substitution of Ba and Bi in the PZT lattice. This disorder breaks the translational symmetry, reduces the correlation length for the interaction of the polar domains, and prevents the formation of a normal ferroelectric state. Rather, critical slowing down of the dipolar fluctuations sets in at T_m resulting in the formation of the relaxor state.

Significance--The results of the present work make it clear that the properties and physics of PBZT-Bi are very different from those of normal ferroelectrics. Thus, models developed to describe the response of ferroelectrics such as the PZTs will be inappropriate for PBZT-Bi. The present results provide the basis for an appropriate model.

*In collaboration with George Clark (2671) and Steve Montgomery (1567)

Sponsors for various phases of this work include: DP - Phys. Sci. & Tech., DP - Enhanced Surveillance

Contact: George A. Samara, Nanostructures and Advanced Materials Chemistry Dept., 1152
Phone: (505) 844-6653, Fax: (505) 844-4045, E-mail: gasamar@sandia.gov

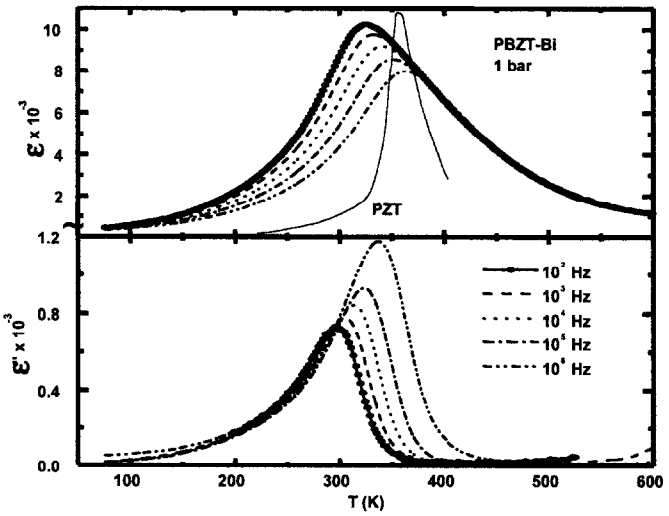

Figure 1

Figure 1. Temperature dependences of the real (ε) and imaginary (ε′) parts of the dielectric function of PBZT-Bi illustrating the relaxor character of this material. Superimposed on the ε′(T) response is a typical frequency-independent response of a ferroelectric PZT ceramic to illustrate the very broad ε′(T) peak of PBZT-Bi.

Figure 2. Temperature dependence of the local dipolar polarization of nano-size domains ($\sqrt{P^2}$) in PBZT-Bi calculated from the anomalous thermal expansion due to electrostriction. Shown for comparison are early polarization data on PBZT-Bi samples of the same composition as the present material. Specifically, the temperature dependences of the remanent polarization P_R and of the polarization at two different field strengths are shown over the ranges of the available data. The agreement between the 40 kV/cm data and the calculated $\sqrt{P^2}$ is indicative of saturating of the polarization at this field strength.

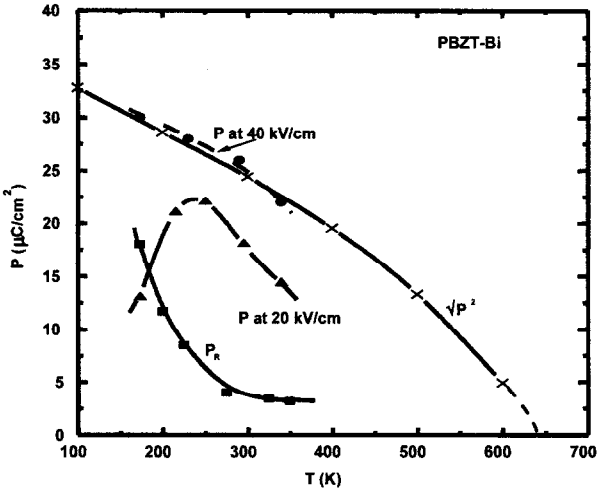

Figure 2

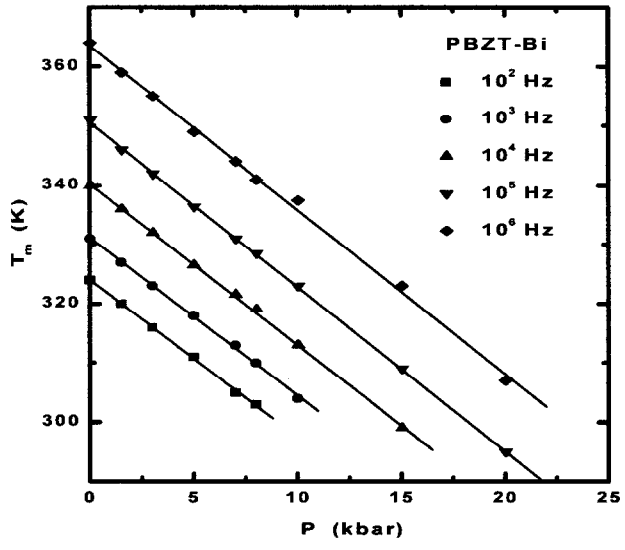

Figure 3

Figure 3. Pressure dependence of the dynamic glass transition temperature T_m of PBZT-Bi showing the frequency dispersion in Tm which corresponds to the peak in ε′(T).

The Shock Properties of PZT 95/5

R. E. Setchell, S. T. Montgomery, M. D. Furnish, and L. C. Chhabildas

Motivation--Although pulsed power devices utilizing shock-induced depoling of the ferroelectric ceramic PZT 95/5 have been in use for many years, an important responsibility currently being addressed at Sandia is the design and certification of several new devices. A strong desire to progress beyond the historical "build and test" approach has resulted in a substantial effort to achieve accurate numerical simulations of device operation. A major challenge at the start of this effort, however, was the fact that very few studies of the complex dynamic behavior of poled PZT 95/5 had been conducted during the past twenty years. Consequently, an extensive experimental program was started two years ago to provide insight and well-characterized data for the development of improved models for PZT 95/5.

Accomplishment--During the first year, this study addressed the mechanical behavior of unpoled PZT 95/5 over the range of axial stresses of interest (5 to 50 kbar). Planar impact techniques were used with both PVDF film gauges and laser interferometry (VISAR) to characterize wave evolution under conditions that examined the FE to AFE phase transition and dynamic pore collapse. In the second year, emphasis was placed on shock-induced depoling of samples that were either normally or axially poled (poled perpendicular or parallel to the intended shock motion, respectively). Twenty experiments examined the depoling process and corresponding wave evolution over the full range of impact stresses. Normally poled samples either had short-circuit conditions or different passive resistive loads so that internal fields could be varied up to 36 kV/cm. Axially poled samples only had short-circuit conditions, but generated even stronger opposed fields on either side of the shock wave. Shock-induced currents passing through an external circuit under short-circuit conditions are shown in Figs. 1 and 2 for the two poling cases over a range of impact stresses. Acoustic transit times through the fixed 4-mm sample thickness are also shown. Normally poled samples exhibit essentially complete depoling during shock passage for impact stresses of 24 kbar or greater (Fig. 1). At lower stresses the phase transition is inhibited, particularly as a threshold impact stress (approximately 5 kbar) is approached. Target configurations resulted in compressive reflected waves after the initial shock transit, and additional depoling occurs at the lower stresses during the reflected wave motion. In contrast, currents through an external circuit from axially poled samples (Fig. 2) are strongly inhibited at impact stresses above 9 kbar. The onset of shock-induced conductivity was suggested for similar observations in early investigations of axially poled PZTs. VISAR data was also recorded in each of the normally and axially poled experiments. At a given impact stress, the waveforms showed only subtle differences due to poling condition and - surprisingly - no observable differences in end states over a broad range of internal field strengths.

Significance--The data base now available represents a substantial challenge to the on-going development of improved models for PZT 95/5. However, successful simulation of these planar experiments, together with a number of multi-dimensional experiments planned for the coming year, will signify the achievement of an essential goal in the effort to accurately simulate the operation of pulsed power devices.

Sponsors for various phases of this work include: DP - MAVEN, DP- Phys. Sci. & Tech.
Contact: Robert E. Setchell, Nanostructures and Advanced Materials Chemistry Dept., 1152
Phone: (505) 844-3847, Fax: (505) 844-4045, E-mail: resetch@sandia.gov

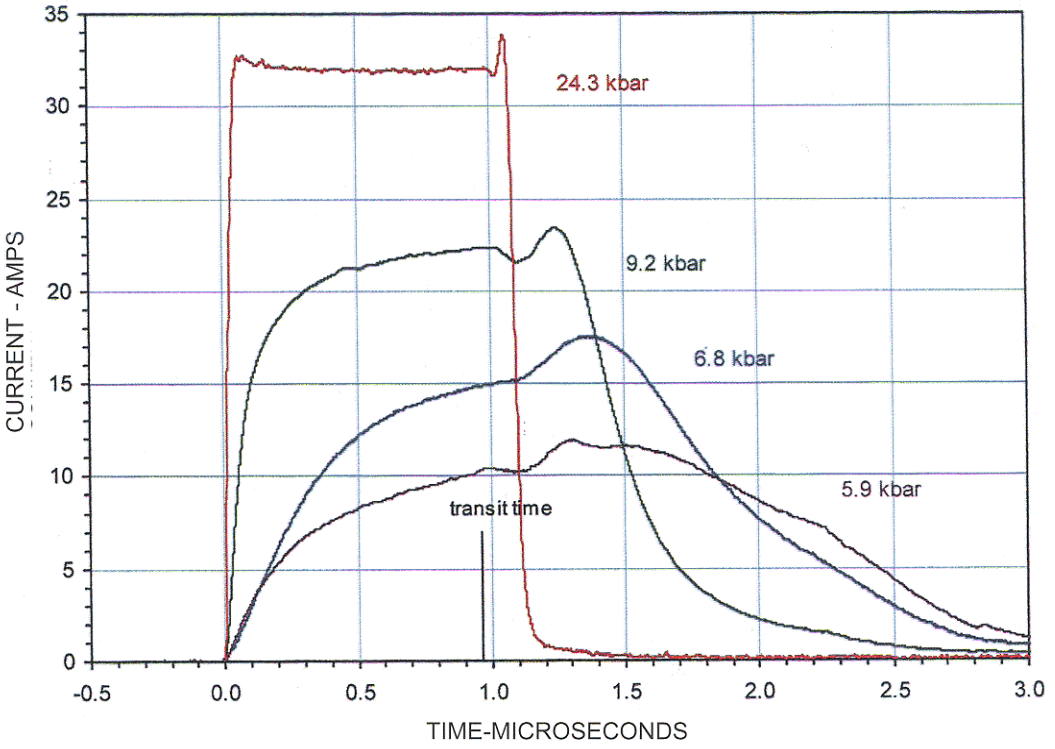

Figure 1. Shock-induced currents from normally poled samples with short-circuit loads.

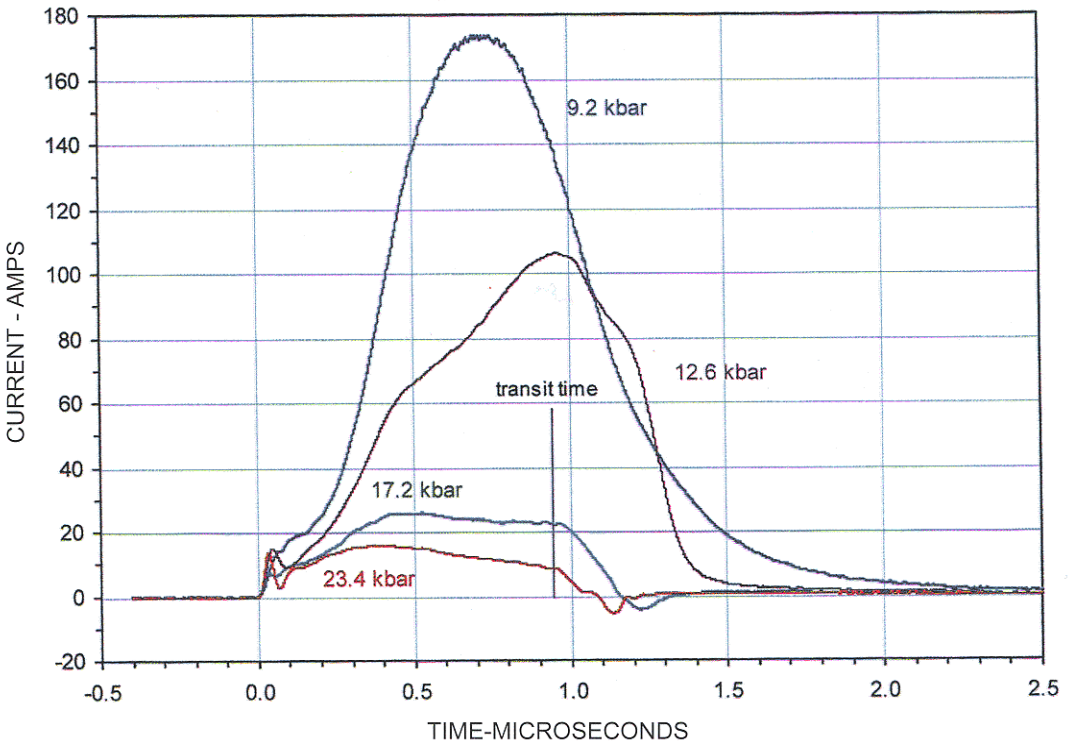

Figure 2. Shock-induced currents from axially poled samples with short-circuit loads.

Nanoscale Materials Science

Electric Field Dependent Diffusion Studied with Atom-Tracking

B. S. Swartzentruber and J. M. Carpinelli

Motivation--A microscopic understanding of local electric field effects on atom and cluster diffusion may provide new ways to control mesoscopic morphology during crystal growth, or predict detrimental electromigration effects. Chemical adsorbates and impurities that can create local electric fields are known to influence crystal growth and electromigration phenomena. Direct observation of electric field effects gives us a window into the fundamental parameters that govern adsorbate diffusion, binding, and chemical reaction processes on surfaces.

Accomplishment--Using atom-tracking scanning tunneling microscopy (STM), we directly measured how an applied electric field alters the diffusion and rotation barriers for adsorbed Si dimers on the Si(001) crystal surface. Atom tracking is a technique in which the probe tip of a STM is locked onto a selected dimer using two-dimensional lateral feedback. When locked, the feedback electronics maintain the tip over the dimer as it diffuses over the substrate, tracking its coordinates and rotational orientation. The time response of the atom tracker is fast enough to record every hop of the dimer. Once the diffusion events are captured, the statistics of the diffusion process can be analyzed directly, without the assumptions implicit in a classical random-walk analysis. Furthermore, because the tip is continuously in position over the dimer, it is easy to systematically vary the tip-induced electric field in both magnitude and direction by changing the applied bias voltage and monitor any change in the activation barriers. In Figure 1 we show the measured response of the activation barriers of dimer rotation, (a), and diffusion, (b). The rotation barrier has an approximately quadratic dependence on the electric field (decreasing with the magnitude, regardless of the sign), whereas the diffusion barrier varies linearly with the field. In neither case is the size of the variation more than ~6% of the barrier height. The smooth quality of the data allows us to extrapolate to the intrinsic, zero-field barriers. We have also measured the response of Si-dimer kinetics on an applied lateral field by offsetting the STM tip laterally by as much as one-half a lattice constant. We find that the response of the dimer in the presence of the offset tip is more sensitive to the more mesoscopic length scale of the tip shape than the detailed structure of the last few atoms of the tip.

Significance--By performing quantitative measurements of the electric-field perturbation on atomic-scale adsorbate kinetics, we determine the influence of the atom-tracking process on the intrinsic energy barriers. For the case of Si on Si(001) we find that the instrument has a very small effect, and therefore is a reliable measurement of the fundamental physics. Because the linear electric field dependence of the diffusion barrier is so remarkably different than the quadratic dependence of the rotation barrier, we conclude that the electronic structure of the transition state is primarily responsible for the change in energetics. These quantitative measurements will enable us to couple with first-principles electronic-structure calculations to determine the details of the kinetic processes from the stable binding sites through the transition states.

Sponsors for various phases of this work include: BES, LDRD
Contact: Brian S. Swartzentruber, Surface and Interface Science Dept., 1114
Phone: (505) 844-6393, Fax: (505) 844-5470, E-mail: bsswart@sandia.gov

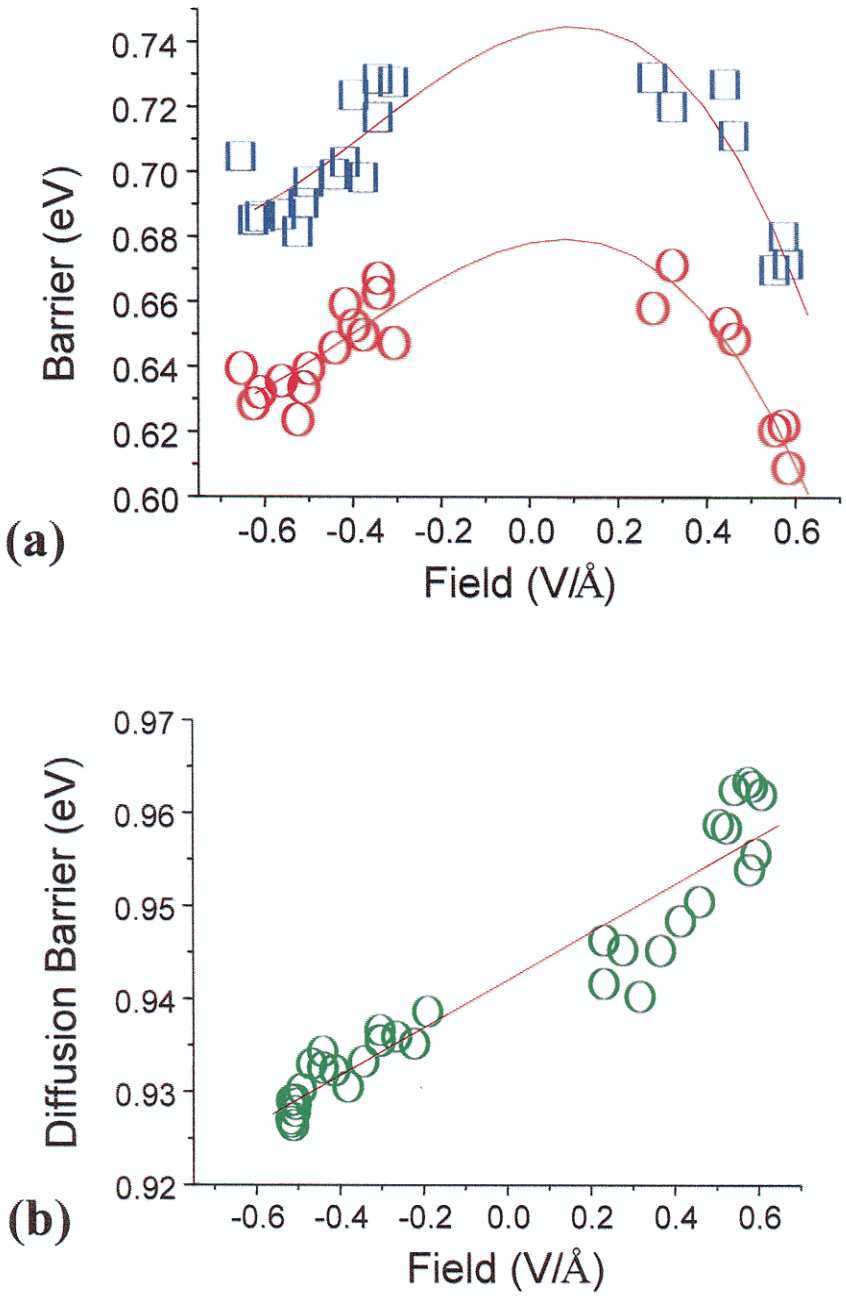

Figure 1. Activation barrier for Si dimer rotation, (a), and diffusion, (b), as a function of applied electric field.

The Behavior of Ion-Implanted H in GaN: Transport, Defect Reactions, and Microstructural Effects

S. M. Myers, J. Han, T. J. Headley, C. R. Hills, G. A. Petersen, C. H. Seager, W. R. Wampler

Motivation--Gallium nitride, a large-bandgap optoelectronic material, is affected in important but poorly understood ways by the interrelated behaviors of defects and H. Ion implantation of H provides a means of introducing both entities at relatively high densities, making their properties accessible to a range of probes; also, at higher doses, such implantation enables microstructural manipulation pursuant to fundamental studies. Moreover, H ion implantation is of interest for the formation of buried insulating layers and for controlled exfoliation in connection with the synthesis of layered structures. We have therefore undertaken a mechanistic investigation of the behavior of ion-implanted H in GaN using transmission electron microscopy (TEM), nuclear-reaction profiling, ion-channeling analysis, and infrared (IR) vibrational spectroscopy.

Accomplishment--Wurtzite-phase GaN was grown epitaxially on sapphire by metal-organic chemical vapor deposition. When this material was implanted with H to concentrations above ~1 at.% and then annealed, faceted bubbles formed, as seen in the high-resolution TEM images in Fig. 1. This microstructure allowed several fundamental properties of the material to be determined: 1) The bubble walls are found to be close-packed (0001) and {1011} surfaces with N-terminated polarity, indicating that such surfaces are energetically preferred in the presence of H. 2) IR spectroscopy reveals two new vibrational modes, shown in Fig. 2, due to N-H bonds on the bubble walls at a coverage of ~1 monolayer; this H passivation is believed responsible for the predominance of N-terminated rather than Ga-terminated surface polarity. 3) Measurement of the release of H from the bubbles during annealing allowed the first determination of the diffusivity-solubility product, or permeability, of H in GaN. The permeability is exceptionally small in this material, resulting in the retention of H to unusually elevated temperatures; at 900°C, for example, we obtain a value of $2^{\sim}10^{6}$ atoms cm^{-1} s^{-1} $bar^{-1/2}$. 4) The partition of retained H between wall chemisorption and pressurized H_2 gas, as revealed by IR spectroscopy coupled with nuclear-reaction analysis of total H, indicates that the chemisorbed state is somewhat less stable than the molecular gas. This contrasts with the greater stability of the chemisorbed state found by us in Si. 5) Ion-channeling analysis coupled with TEM shows that the formation of H_2 bubbles is accompanied by generation of interstitial defects in numbers corresponding to the displaced volume. These defects undergo annealing in the temperature range 500-700°C, giving rise to basal-plane stacking faults containing one extra Ga-N bilayer.

At implanted concentrations below 0.1 at.%, bubbles do not form. The H instead forms N-H bonds within the wurtzite lattice, as shown by us and others using IR spectroscopy; the N-H stretch frequencies are lower than those associated with H on bubble walls, reflecting the different atomic configuration. Ion-channeling results, shown in Fig. 3, indicate a H lattice position within the open [0001] channel, consistent with a N antibonding site.

Significance-This investigation illuminated multiple fundamental aspects of the interrelated behaviors of H and defects in GaN.

Sponsors for various phases of this work include: BES, DP - Phys. Sci. & Tech., LDRD
Contact: Sam M. Myers, Nanostructure and Semiconductor Physics Dept., 1112
Phone: (505) 844-6076, Fax: (505) 844-7775, E-mail: smmyers@sandia.gov

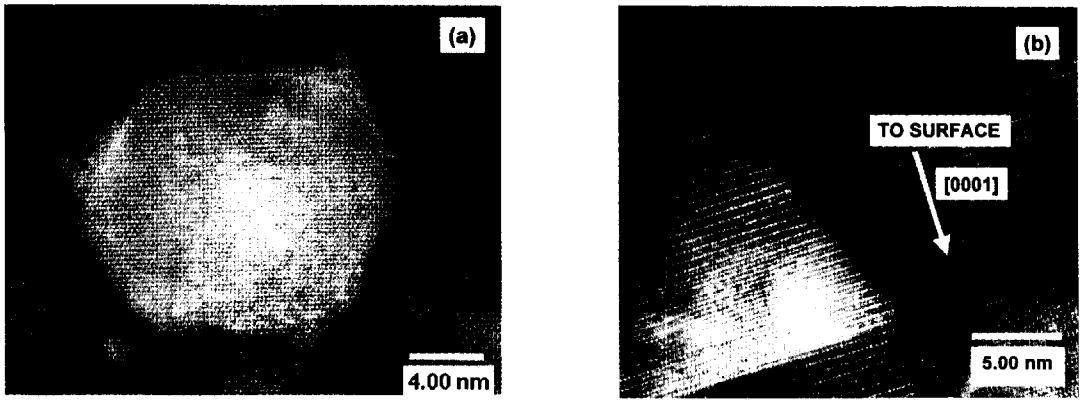

Figure 1. High-resolution TEM images of H_2 bubbles in GaN after implanting H to a concentration of ~1 at.% and then annealing at 900°C for 1 hour. (a) Plan view in [0001] orientation. (b) Cross-section view in $[11\bar{2}0]$ orientation. These images exhibit the energetically preferred (0001) and $\{10\bar{1}1\}$ surfaces.

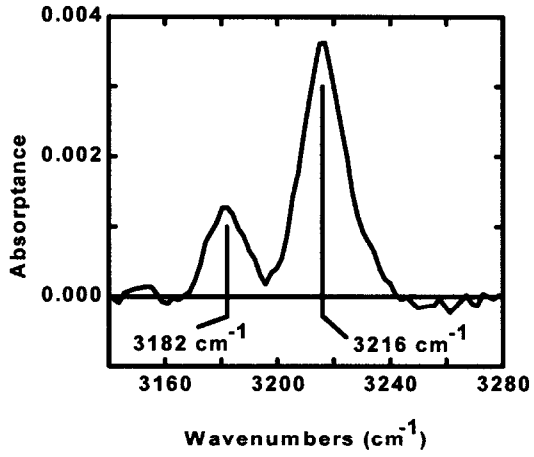

Figure 2. Infrared absorption peaks associated with N-H centers on the walls of H_2 bubbles.

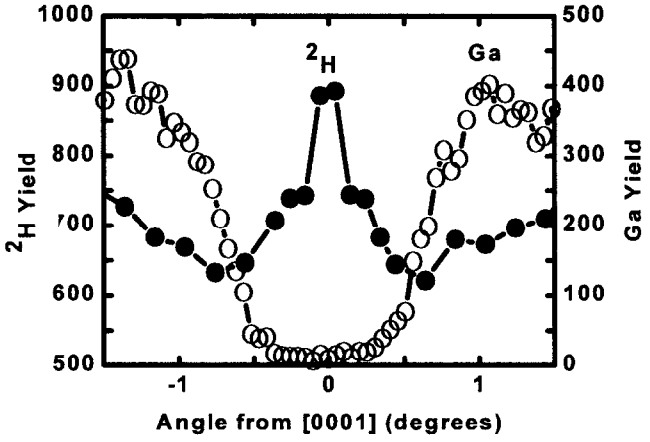

Figure 3. Ion channeling of implanted deuterium (^2H) and host-lattice Ga after room-temperature implantation of ^2H to a concentration of ~0.06 at.%. The central peak in the nuclear-reaction yield from ^2H indicates a ^2H site in the [0001] channel.

Novel Real-Time Diagnostics Demonstrate the Importance of Elastic Repulsion on Coherent Island Evolution

*J. A. Floro, M. B. Sinclair, R. Q. Hwang, and J. A. Hunter**

Motivation--Strain-layer heteroepitaxy is an area of thin film growth that is extremely important for both science and technology. While it has been recognized for a decade that coherent island formation provides a pathway to strain relaxation during lattice-mismatched epitaxial growth, the fundamental thermodynamics of island formation have not been well understood. Small coherent islands exhibit quantum confinement effects that make them useful for tunable light emission/detection applications, provided the size distribution of the island ensemble can be controlled during growth.

Accomplishment--We have developed a comprehensive understanding and quantitative model of island evolution during epitaxial strained-layer growth. This theoretical understanding was fostered by our extensive experimental use of two novel optical probes (see Fig. 1): (1) the Multi-beam Optical Stress Sensor (MOSS), which determines film stress through the measurement of wafer curvature; and (2) the Light Scattering Spectrometer (LiSSp), which measures the spatial period and correlation length of surface roughness. Both techniques were developed at Sandia for in situ, real-time monitoring during thin film deposition. With these diagnostics, we directly measure the kinetics of island nucleation, coarsening, self-organization, and phase transformations within growing SiGe island arrays (Fig. 2). By working in real-time, we can quantitatively examine behavior that would be extremely difficult to observe by standard "cook-and-look" approaches, e.g., island coarsening that accelerates during deposiiton and leads to self-organization of the array. This has allowed us to develop a unified model of island evolution that treats ensembles of islands rather than individual islands in isolation. We have shown that elastic repulsion between islands forms a significant component of the total energy of an ensemble. As a result, islands in an ensemble evolve differently from isolated islands. Since typical growth conditions produce dense island arrays, and since such arrays are desirable for applications, this represents a significant new contribution to the understanding of strain-driven island formation.

Significance--By quantifying the effects of elastic repulsion on the evolution of strained islands, we now have a detailed understanding of the evolution of morphology in strained-layer epitaxy. Furthermore, the experimental approaches pioneered here can be applied to the investigation of other proposed energetic contributions to island formation, such as the role of surface-stress. These elastic effects have implications for the evolution of solid state systems that extend beyond epitaxial film growth, including polycrystalline thin film evolution, coherent precipitate formation and coarsening, and nanocluster synthesis and stability. Our new diagnostics, while designed with the islanding problem in mind, have already demonstrated their value in probing the physics of film growth in many other challenging and scientifically important systems (examples: gallium nitride, interconnect metallization, sputter ripple formation, diamond-like carbon, and magnetic multilayers).

*In collaboration with Professors Eric Chason and L. Ben Freund, Brown University
Sponsors for various phases of this work include: BES, LDRD
Contact: Jerry Floro, Nanostructure and Semiconductor Physics Dept., 1112
Phone: (505) 844-4708, Fax: (505) 844-1197, E-mail: jafloro@sandia.gov

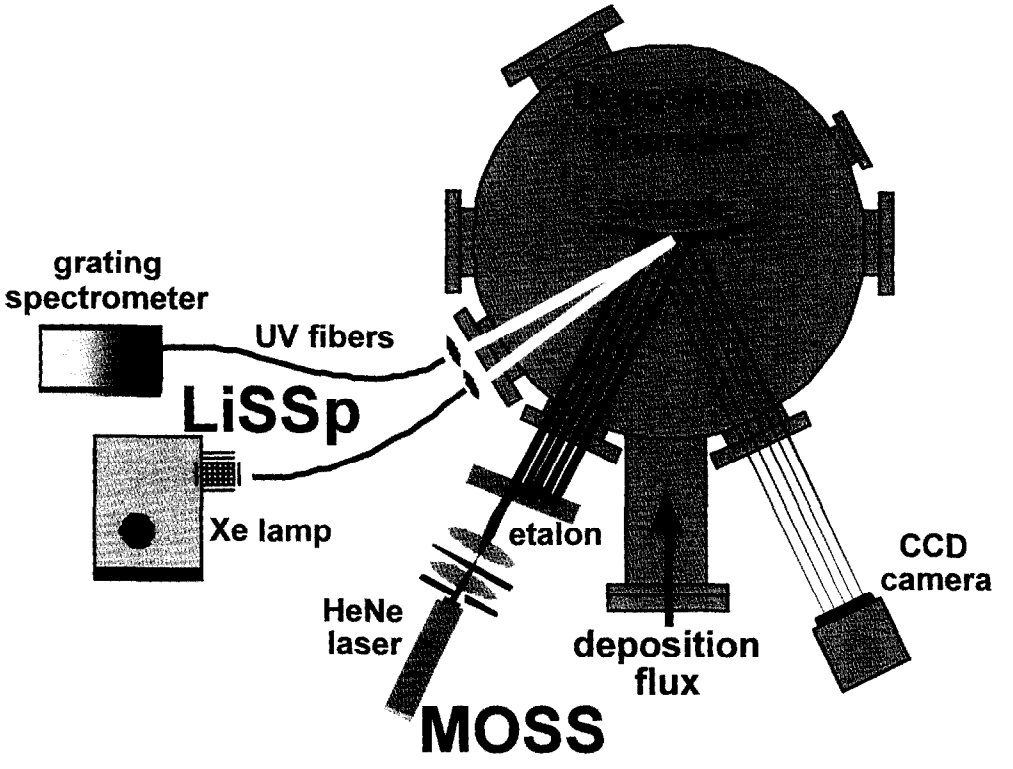

Figure 1. Schematic illustration of MOSS and LiSSp setup on a thin film deposition chamber.

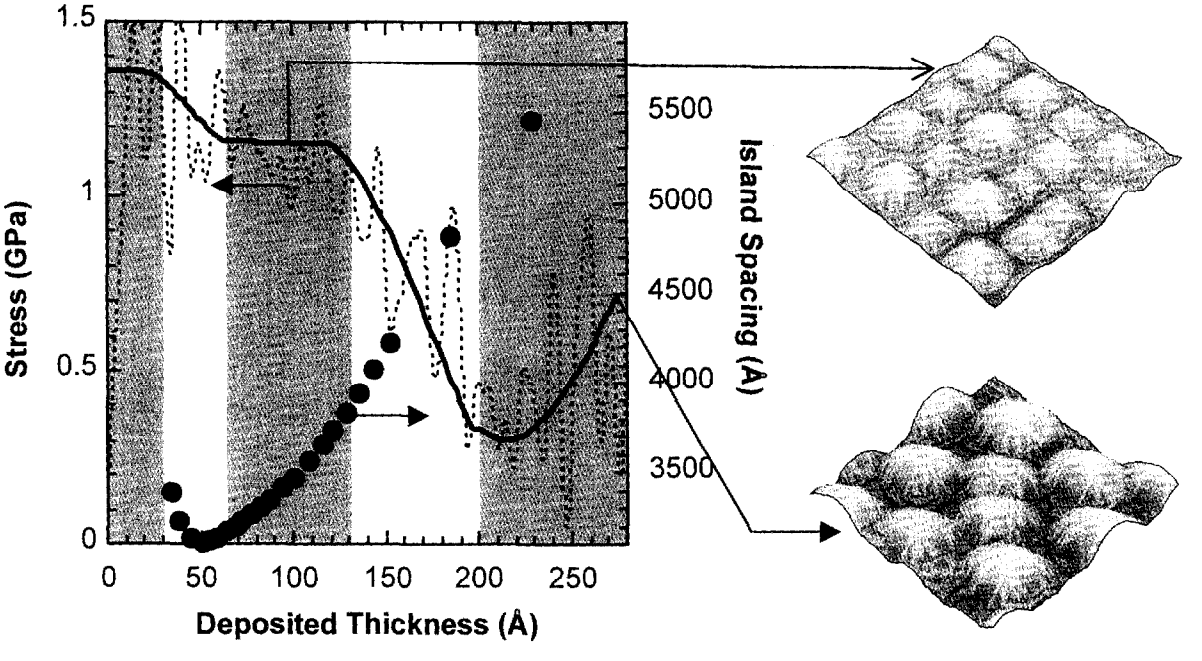

Figure 2. Stress from MOSS (dashed line is data, solid line is guide to the eye), and island spacing from LiSSp (circles) during Si_8Ge_2/Si (001) heteroepitaxial growth. Corresponding island morphologies are also shown (2x2 mm atomic force micrographs).

First-Principles Analysis of Adsorbate-Controlled Diffusion on Imperfect Pt(111)

*P. J. Feibelman**

Motivation--As part of an effort to convert surface impurities from a nuisance to a systematically applicable nano-fabrication tool, we have sought to interpret the discovery that O atoms on a growing Pt(111) crystal foster perfect layerwise growth, when without them, epitaxy produces 3-dimensional pyramidal mounds (see Fig. 1). This required that we discover where O atoms reside on imperfect Pt(111), how Pt atoms migrate both on perfect terraces and near defects, and how Pt-atom migration is affected by the presence of O atoms.

Accomplishment--We learned in considerable detail how O atoms attach to the one-atom-layer-high Pt islands that appear as material is first deposited on a growing Pt(111) crystal. Our first-principles calculations not only explain the unusual O-related features seen in high resolution scanning tunneling microscope images of O-covered islands, but also account quantitatively for corresponding measurements of O vibration frequencies. Significantly, the calculations reveal what basic energies determine the O atoms' binding-site preference.

With these successes as a background we wanted to know how easy it is for Pt atoms initially deposited on top of an island to migrate to its edge and "fall off" onto the terrace below. If this process is only activated at high temperatures, one expects islands to nucleate on top of islands, leading to the formation of pyramidal structures. Thus a possible explanation of the effect of O atoms on Pt growth is that O atoms near island edges facilitate the "falling off" process, so that a complete Pt layer can form before an island can nucleate on top of an island and start pyramid formation.

Surprisingly, our computed results starkly conflicted with the basic information we hoped to explain. We found that falling off (100)-microfacet steps (see Fig. 2) is very easy. Thus: 1) In contradiction to experiment, pyramids bounded by such steps should never grow (the atoms comprising the upper islands should migrate to lower terraces), and 2) O atoms cannot make it any easier than it already is for Pt atoms to fall over them. We therefore suggested that there was an experimental problem. Gratifyingly, the group that published the original Pt growth study has now reported that a) below 450K, their steps were saturated with CO molecules from the background, and b) when the CO is removed, the island morphology changes into agreement with our predictions!

Significance--Our results show that in contrast to widely applied "semi-empirical" simulations, current first-principles structural calculations are predictive for rather complex, "real-world" surfaces, to the extent that they can be trusted to critique the validity of experimental results. The discovery that the real effect of the O is to remove small coverages of CO emphasizes the importance of our initial problem: Trace amounts of relatively weakly bound background gases can play an important, and in principle controllable role in determining the morphology of growing crystalline films.

*Experimental data provided by Drs. Thomas Michely and Stephanie Esch, Juelich (GERMANY)

Sponsors for various phases of this work include: DP - Phys. Sci. & Tech., BES, LDRD

Contact: Peter J. Feibelman, Surface and Interface Sciences Dept., 1114
Phone: (505) 844-6706, Fax: (505) 844-5470, E-mail: pjfeibe@sandia.gov

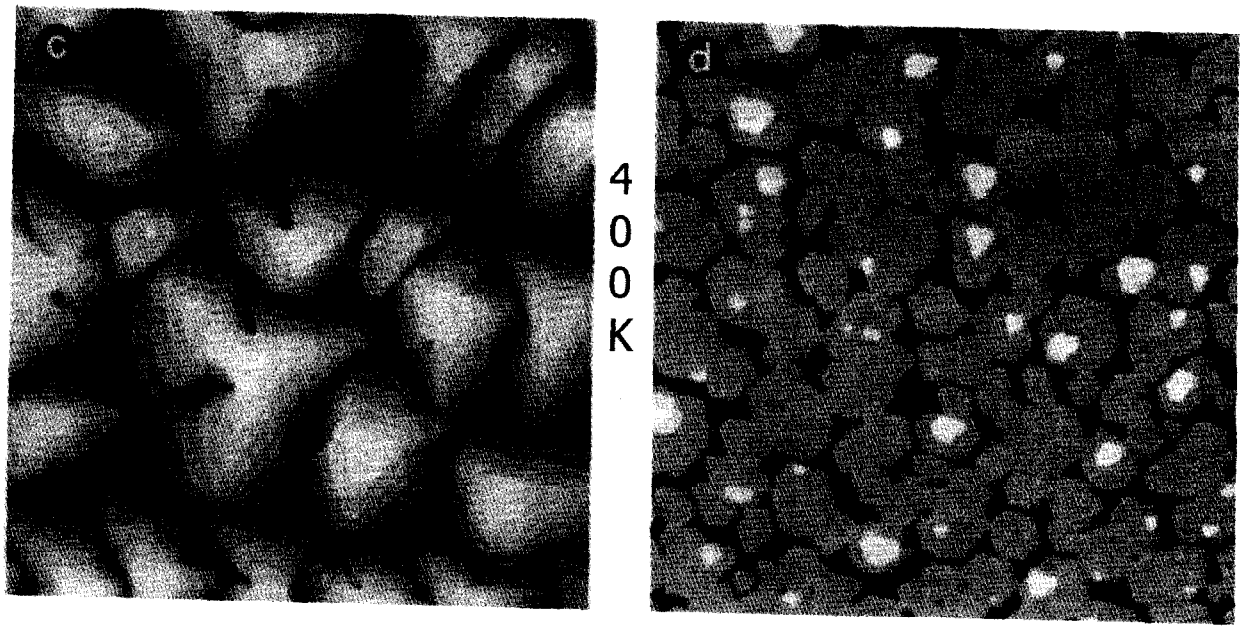

Figure 1. After Esch, et al., scanning tunneling micrographs showing pyramidal growth in Pt epitaxy on clean Pt(111) and layer-by-layer growth, when the surface is precovered with oxygen atoms. The pyramid boundaries are (100)-microfacet steps as shown in Fig. 2.

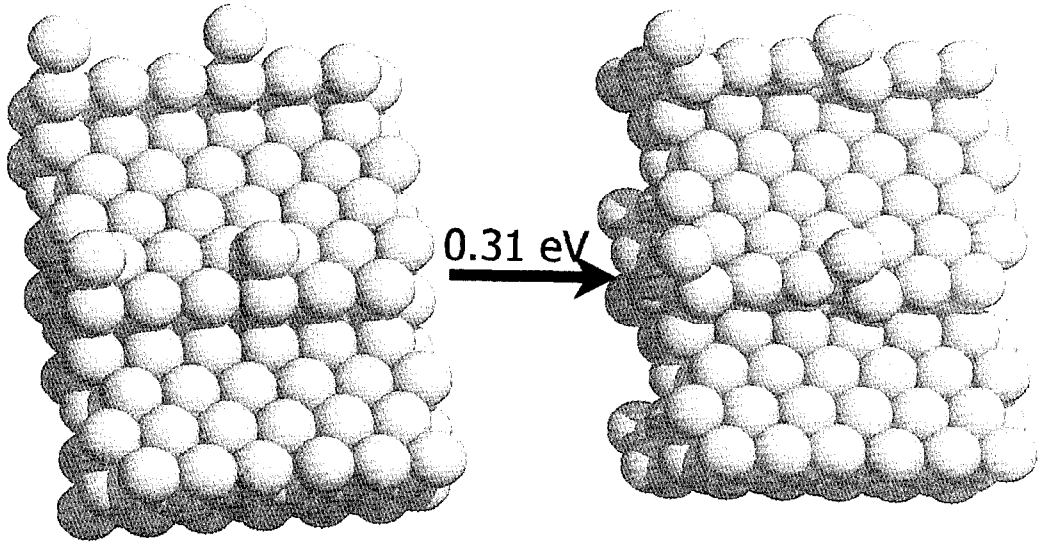

Figure 2. A low energy process whereby a Pt atom bound near a (100)-microfacet step is incorporated into the step as an atom of the step edge emerges onto the terrace below. The energy cost of this process, 0.31 eV, is only 0.02 eV more than the barrier to migration on a perfect terrace.

Low Energy Electron Microscope Study of Si(001) Etching by Molecular Oxygen

J. B. Hannon, M. C. Bartelt, N. C. Bartelt and G. L. Kellogg

Motivation--Exposure of the Si(001) surface to low pressures of molecular oxygen at temperatures exceeding 800C produces volatile SiO leading to a net removal of Si from the surface. Despite its importance as a potential procedure for cleaning Si, a comprehensive understanding of the kinetic processes underlying this etching phenomenon is still lacking. Current models are based on experiments in which the state of the surface during etching is unknown. This problem can be addressed using the unique imaging capabilities of the low energy electron microscope (LEEM).

Accomplishment--We have combined low energy electron microscopy with kinetic Monte Carlo simulation and diffusion equation analysis to identify the mechanism and determine the energetics by which molecular oxygen etches Si(001) surfaces. Our results show that oxygen adsorption leads to vacancy creation on the terraces followed by diffusion of the vacancies to single-atom high steps. This mechanism allows us to model the etching process as a temperature-dependent flux of vacancies onto the surface and apply standard nucleation and growth theory to extract kinetic parameters.

On typical Si(001) terraces (~0.5μ wide or less), vacancy creation/diffusion leads to step flow similar in appearance to ordinary sublimation. However, on large terraces (~5μ or larger), vacancy concentration during etching can reach levels sufficient high to nucleate vacancy islands. LEEM measurements of the growth rate of these islands provides quantitative information on the vacancy flux, and, in turn, the rate of etching. Figure 1 shows a sequence of LEEM images illustrating the time evolution of the growth of 25 vacancy islands on an 11.1μ wide Si(001) terrace. The large terraces were prepared by a novel procedure involving the formation of square pits in the Si wafer and subsequent etching of the pit bottoms by oxygen exposure at elevated temperatures. The key observation from these measurements is that the growth rate of a given island depends on its location with respect to neighboring islands (e.g., island A grows faster than C in Fig. 1). Specifically, the growth rate is defined by a capture area within which vacancies are supplied to the island. The observed growth rates are faithfully reproduced by kinetic Monte Carlo Simulations and a diffusion equation analysis (Fig 1). The validity of the diffusion equation analysis is established by the ability to fit the simultaneous growth of up to 25 islands with just one adjustable parameter (the vacancy flux). A plot of the flux (effective etch rate) vs. inverse temperature for three different oxygen pressures is shown in Figure 2. From these data we determine that the activation energy for Si etching is 2.0 ± 0.4 eV. This result is significantly lower (by a factor of 2) than that measured in molecular beam experiments.

Significance--This large discrepancy in measured activation energies shows that etching of Si(001) surfaces by molecular oxygen is much more complicated that can be inferred from measurements of desorption products alone. Real-space imaging of surfaces that are both well-defined and reproducible along with the ability to observe dynamic processes under steady state conditions avoids the uncertainties inherent in past investigations leading to a new understanding of the etching process.

Sponsors for various phases of this work include: BES, DP - Phys. Sci. & Tech., LDRD
Contact: Gary L. Kellogg, Surface and Interface Science Dept., 1114
Phone: (505) 844-2079, Fax: (505) 844-5470, E-mail: glkello@sandia.gov

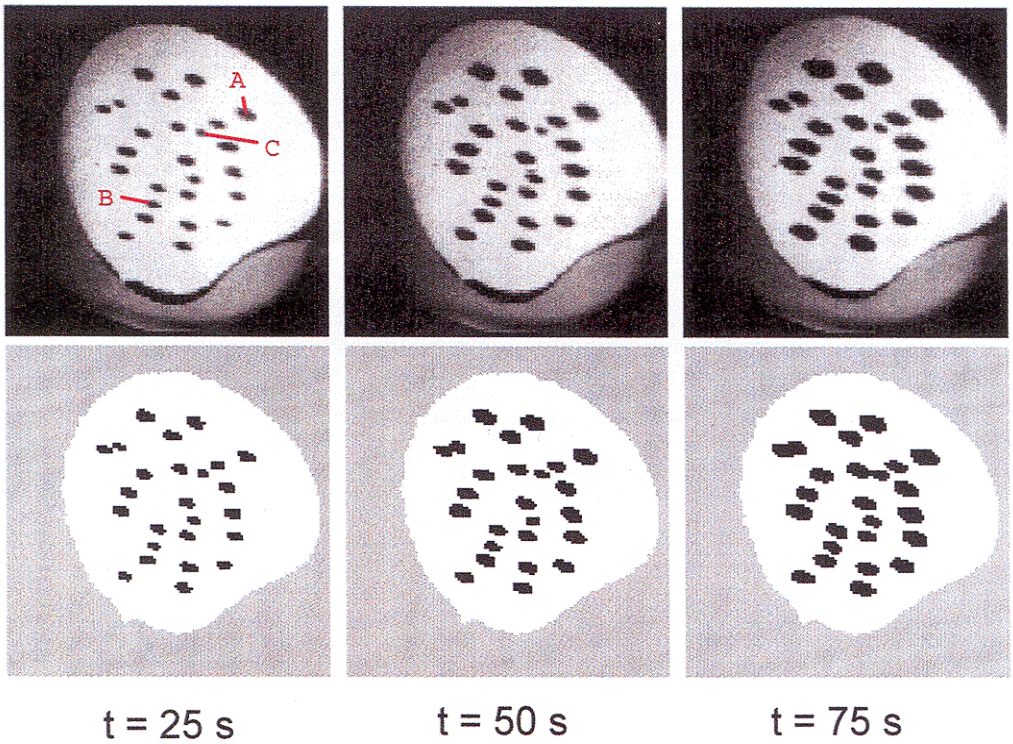

Figure 1. (Top) LEEM images showing the growth of vacancy islands on an 11.1m wide terrace on Si(001). The sample temperature is 815C and the oxygen pressure is 7.8×10^{-8} Torr. (Bottom) Simulation of island growth with diffusion equation analysis. The growth rate of 25 islands is reproduced with just one adjustable parameter.

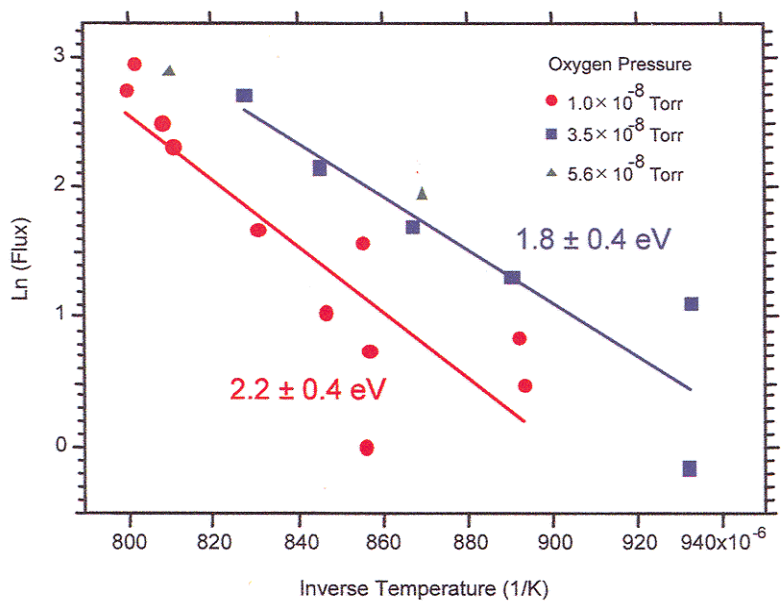

Figure 2. Arrhenius plots of the effective flux of vacancies for three oxygen pressures. The activation energy of Si removal is 2.0± 0.4 eV.

Photooxidation of Organic Waste by Semiconducting Nanoclusters

*J. P. Wilcoxon and T. R. Thurston**

Motivation--The use of organic chemicals as solvents in a variety of manufacturing, agricultural, and DOE applications has led to the water contamination with these chemicals - the most pernicious and ubiquitious being chlorinated hydrocarbons and polycyclic aromatics. These robust, long-lived chemicals are present in large volumes of water and are difficult and/or expensive to remove by any extant technology. Our goal is to use novel types of nanosize semiconductors, first synthesized at Sandia, as photooxidation catalysts to affect the complete mineralization of these chemicals to CO_2 and dilute mineral acids using sunlight as the sole energy source.

Accomplishment--Photooxidation of organic chemicals to CO_2 and dilute mineral acids (mineralization) occurs readily upon exposure to deep UV (i.e. <300 nm) radiation. Unfortunately, the costs associated with UV-lamp-driven photooxidation is prohibitive for the large volumns of contaminated water which must be treated at DOE sites. Thus, a photocatalyst is needed to allow the direct utilization of (free) solar energy. However, prior to this work the only available materials which could catalyze the photooxidation of stable chlorinated hydrocarbons were conventional bulk metal oxide powders such as TiO_2 or SnO_2. However, these wide-bandgap materials absorb less than 3% of the solar spectrum at sea level. Other bulk semiconductor materials which are photostable and thus could be used as photocatalysts such as MoS_2 or WS_2 absorb in the near IR and have insufficiently positive valence (hole) bands to photooxidize most organics of interest. We synthesized tunable bandgap nanosize MoS_2 and WS_2 for the first time and demonstrated the successful destruction of very stable aromatics such as phenol and pentachlorophenol (a major environmental pollutant) using only light with wavelengths >450 nm. This accomplishment (Fig. 1) is the first where such chemicals have been mineralized to CO_2 using a photo-stable, totally inorganic, photocatalyst. By constrast, as shown in Fig. 1, the best available TiO_2 photocatalyst, has no activity.

A further accomplishment was the successful synthesis of a hybrid TiO_2/MoS_2 semiconductor photocatalyst and its use in the photodestruction of phenol. Figure 2 shows our results with this catalyst compared to pure TiO_2. This synthesis provides a route to a practical fixed-bed photocatalyst based upon available TiO_2 monoliths which could be doped with tunable bandgap nanoparticles of MoS_2. Such a system, with a range of MoS_2 bandgaps spanning the near UV to the near IR should be capable of oxidizing even extraordinarily robust chemicals such as DDT or polychlorinated biphenols.

Significance--We have developed a new class of nanosize photocatalysts which can destroy robust organic pollutants in the environment using only visible light. This development has the potential to significantly reduce remediation costs compared to current photooxidation schemes using UV-lamp driven photooxidation. We have also demonstrated the ability to deposit nanoclusters of MoS_2 on conventional metal oxide supports such as TiO_2 which then function as hybrid photocatalysts for the destruction of organic molecules.

*In collaboration with ER/EM, D. F. Kelley, Colorado State University

Sponsors for various phases of this work include: EM/BES

Contact: Jess P. Wilcoxon, Nanostructures and Advanced Materials Chemistry Dept., 1152
Phone: (505) 844-3939, Fax: (505) 844-4045, E-mail: jpwilco@sandia.gov

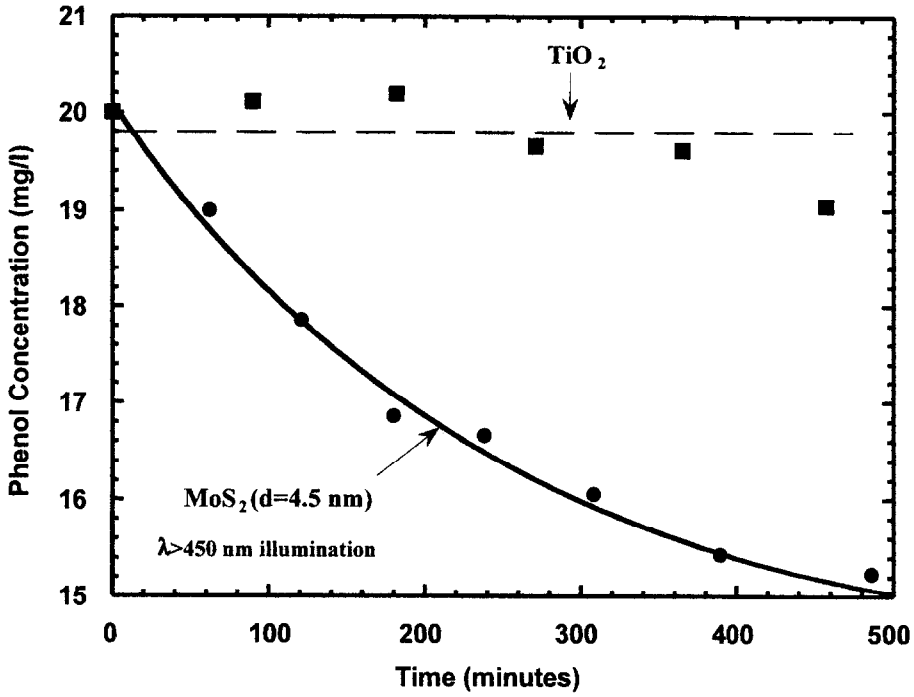

Figure 1. Phenol destruction as a function of time for nanosize MoS_2 and a conventional TiO_2 photocatalyst. TiO_2 does not absorb visible light so no photooxidation is possible. Nanosize, d = 4.5 nm MoS_2 absorbs visible light from 400 to 550 nm and photooxidizes the phenol. No attempt has been made thus far to optimize the conditions for this reaction.

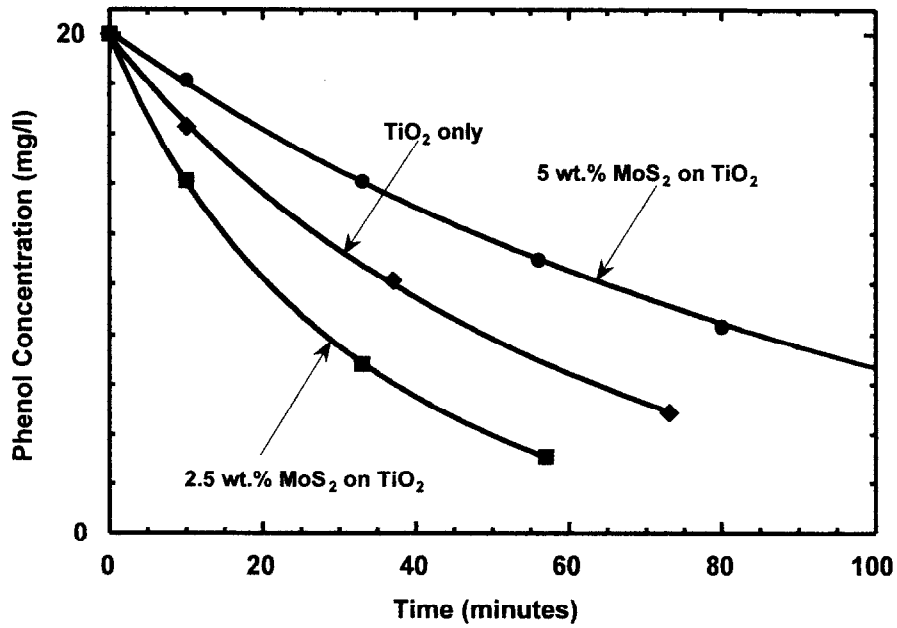

Figure 2. Phenol concentration as a function of time for a conventional TiO_2 powder loaded with d = 8 nm MoS_2 nanoclusters. Near UV radiation at 365 nm was used to exploit both the TiO_2 near-UV absorbance and the nanocluster absorbance.

Tailorable Visible Light Emission from Silicon Nanoclusters

J. P. Wilcoxon, P. N. Provencio, and G. A. Samara

Motivation--Because it is an indirect bandgap semiconductor, silicon (Si) has a major drawback: its inability to emit light efficiently, and furthermore, its weak emission is in the near IR. There is presently a large research effort aimed at exploring physical and chemical means to break silicon's lattice symmetry and mix different momentum (k) states in order to induce a useful level of luminescence and optical gain. One of the approaches has been using nanoclusters; however, the synthetic approaches used have been largely unsuccessful. Success in this endeavor is a major challenge to materials science, one that could have profound technological implications.

Accomplishment--We have successfully grown size-selected Si nanoclusters in the size range 1.8 to 10 nm in the hydrophilic interior of inverse micellar cages. The clusters were separated into chemically pure, monodisperse populations by high pressure liquid chromatography. High resolution TEM fringe images show that the nanoclusters are of high crystalline quality, and electron diffraction and optical absorption data suggest that these nanocrystals retain their bulk-like properties and structure down to the smallest sizes produced (~1.8 nm diameter containing about 150 Si atoms).

Unlike Si clusters prepared by other techniques which exhibit featureless optical absorption spectra, our clusters exhibit well-defined absorption features. The different electronic transitions exhibited various quantum confinement effects. The indirect bandgap shifts from 1.1 eV in the bulk to ~2.1 eV for nanocrystals ~2 nm in diameter, and the direct transition blue shifts by 0.4 eV from its 3.4 eV bulk value over the same size range (Fig. 1). The blue shift of the indirect bandgap with decreasing cluster size is in qualitative agreement with theoretical predictions.

We have observed room temperature photoluminescence (PL) from Si nanocrystals at various wavelengths across the visible range, 700 - 350 nm (1.8 - 3.5 eV). The largest quantum efficiencies (compared to coumarin dye molecules) were ~4% for d = 1.8 nm Si. No post synthesis surface treatment was employed to achieve this significant emission. The most intense PL is in the blue region of the spectrum at ~400 nm (Fig. 2). Its short radiative lifetime (t = 1.5 ns with a faster initial component) is comparable to that for GaAs and suggests a direct recombination mechanism. This is the first observation of direct recombination in Si and is a consequence of quantum confinement and zone folding. A relatively strong PL centered around 580 nm is observed which is fairly insensitive to cluster size and is attributed to surface (or defect) recombination.

Significance--Our Si clusters are the first to exhibit well-defined features in their optical properties, a fact that should challenge theorists to improve models for this important material. The useful level of tailorable visable luminscence observed is very significant and could possibly be improved by surface treatment of the nanoclusters. It opens up the potential of using these clusters in novel detectors and quantum dot arrays. This work represents our first exploratory study of these intriguing clusters. More studies are needed to more fully understand the effects of size and surface termination on the optical and electronic properties.

Sponsors for various phases of this work include: BES, LDRD
Contact: Jess P. Wilcoxon, Nanostructures and Advanced Materials Chemistry Dept., 1152
Phone: (505) 844-3939, Fax: (505) 844-4045, E-mail: jpwilco@sandia.gov

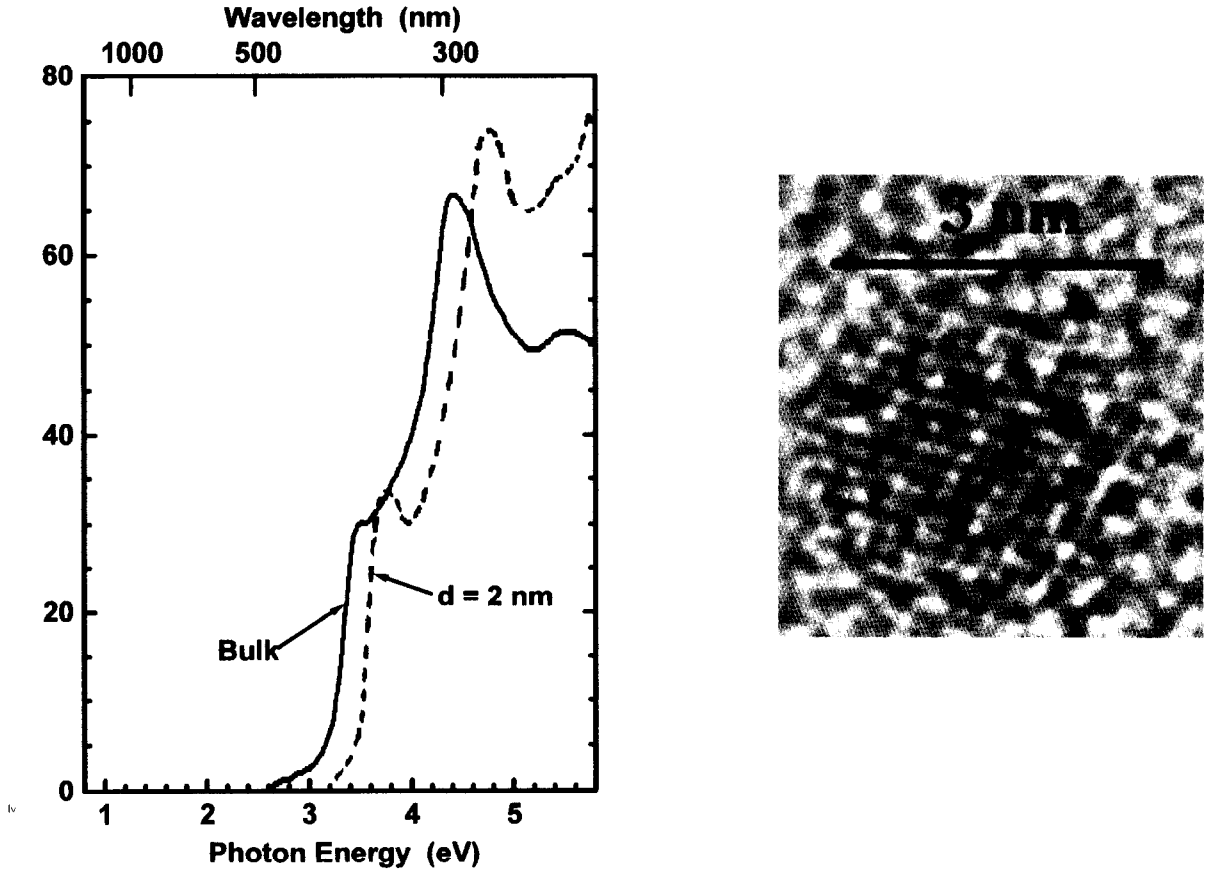

Figure 1. The optical absorption spectrum of a d = 2nm Si nanocrystal sample compared to that of bulk Si. The inset is a high resolution TEM image of a 2 nm crystal showing atomic lattice fringes.

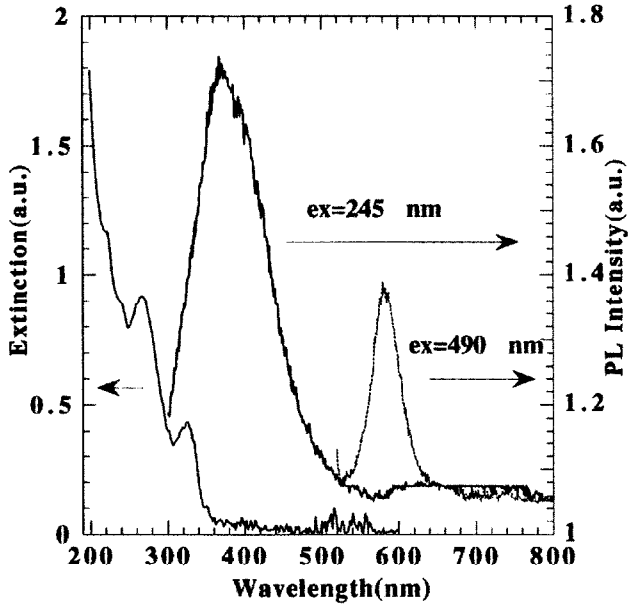

Figure 2. Co-plot of the extinction and photoluminescence spectra (for two excitation wavelengths) for d = 2 nm Si nanocrystals.

Discontinuous Structural Defects for Maximum Current in Superconducting Films

*E. L. Venturini, P. Newcomer Provencio, and B. L. Doyle**

Motivation--Strong magnetic fields penetrate superconductors in discrete, quantized cylinders termed vortices. Maximum performance of high-temperature superconducting (HTS) thin films requires the introduction of structural (lattice) defects to immobilize (pin) these vortices. We are gaining physical insight into this problem by determining the vortex pinning force associated with different microstructural defects.

Accomplishment--Irradiation of HTS films and crystals with neutrons or light ions produces localized defects with a relatively weak vortex pinning force while continuous, amorphous linear tracks generated by high-energy heavy ions provide strong vortex pinning. By changing the incident energy of heavy ions, we introduce controlled microstructural damage ranging from short, discontinuous defects to linear tracks. The maximum (critical) current density in an HTS film at a given temperature and applied magnetic field is proportional to the vortex pinning force, allowing a direct comparison of the pinning produced by different defect structures.

The damage production by irradiation is governed primarily by the electronic energy loss rate, dE/dx, as the heavy ions traverse the HTS film. Calculated dE/dx values are 9.0 keV/nm for gold (Au) ions incident at 30 MeV, 15.2 keV/nm for 60 MeV and 19.5 keV/nm for 88 MeV. Figure 1 shows high resolution cross-sectional transmission electron microscope images comparing the damage produced by 30, 60 and 88 MeV Au ions. The parallel, alternating, light and dark bands are lattice images that show the layered structure of the Tl-Ba-Ca-Cu-O HTS film. The repeated bands are 1.5 nm apart, the spacing between Tl-O layers in this particular HTS film.

The amorphous damage regions are the dark elongated cylinders oriented normal to the layered crystalline structure and parallel to the incident heavy ion direction. The damage regions are ~10 nm wide for all three incident energies. Their average length ranges from a relatively short ~20 nm for 30 MeV Au to ~80 nm for 60 MeV Au and nearly continuous, linear tracks for 88 MeV Au.

Figure 2 compares the vortex pinning force density per unit length in an as-grown Tl-Ba-Ca-Cu-O HTS film with that in films irradiated by 0.001 Au ions per square nm at incident energies of 30, 60 and 88 MeV. The data were calculated from the maximum (critical) current density at 40 K versus magnetic field. Irradiation defects provide much stronger vortex pinning than those in the as-grown film. The short, discontinuous defects from 30 and 60 MeV Au ions are more effective than the linear tracks from 88 MeV Au.

Significance--Maximizing the vortex pinning force is one of the major challenges in the application of HTS materials. Correlating different microstructural defects with changes in pinning force provides crucial physical insight into this problem. We have shown that continuous, linear tracks do not result in the maximum pinning force in Tl-Ba-Ca-Cu-O HTS thin films. A probable explanation arises from the short "effective" vortex length in this highly anisotropic, layered material. The practical implication is that amorphous linear tracks from high-energy, heavy ion irradiation are not essential. We are exploring simpler techniques to produce relatively short, extended defects.

*In collaboration with James Daley, DOE/EERE and Prof. Anatoly Frenkel, New Mexico Highlands Univ.

Sponsors for various phases of this work include: BES

Contact: Eugene L. Venturini, Advanced Materials and Devices Sciences Dept., 1153
Phone: (505) 844-7055, Fax: (505) 844-4045, E-mail: elventu@sandia.gov

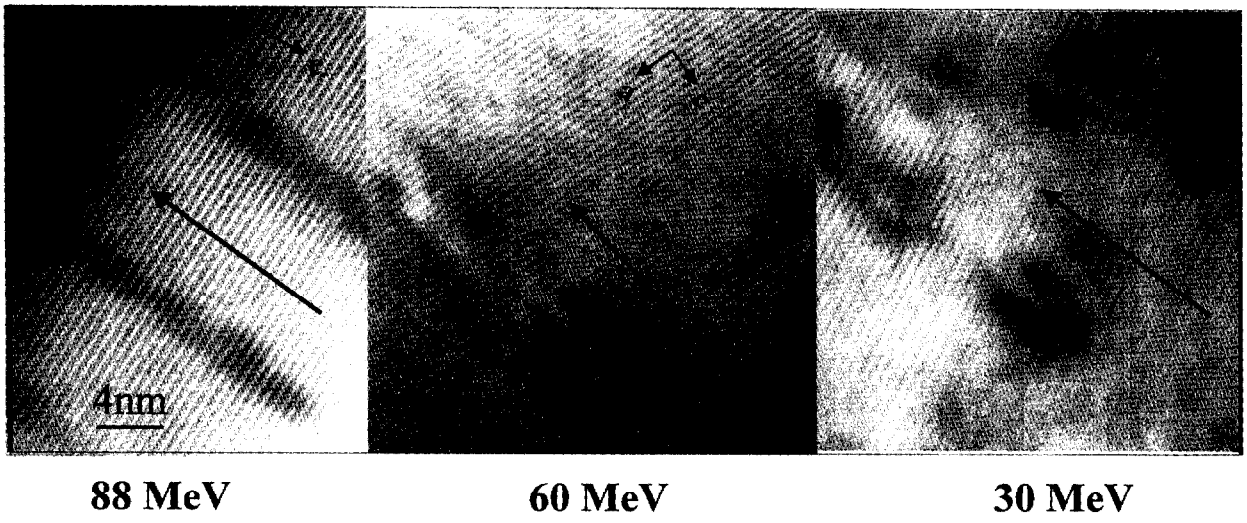

Figure 1. High-resolution cross-sectional transmission electron microscope lattice images of structural damage produced by gold ions incident at 88, 60 and 30 MeV, respectively.

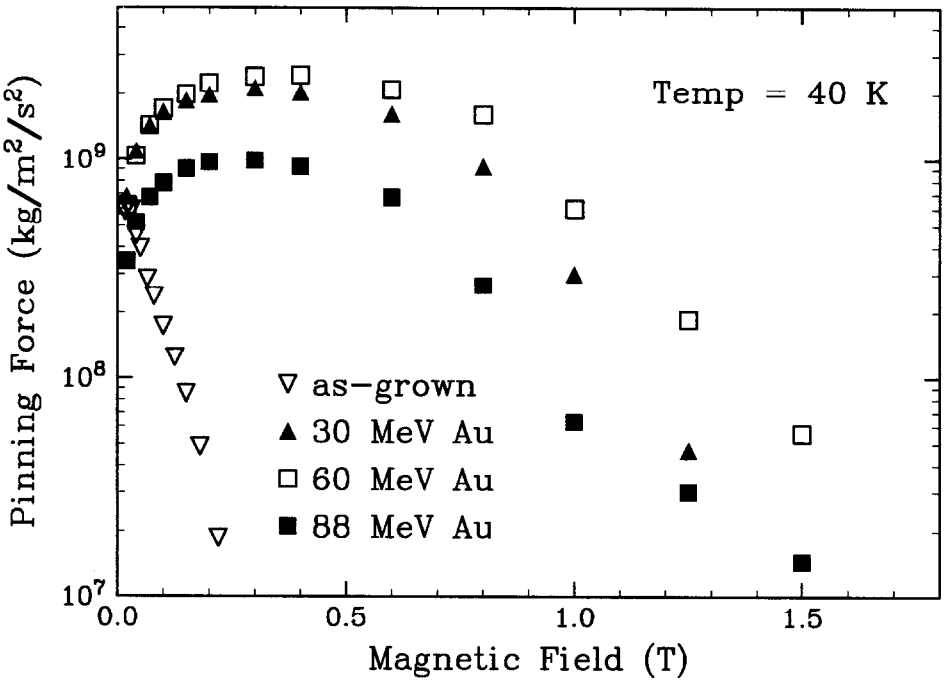

Figure 2. Magnetic vortex pinning force density per unit length at 40 K versus applied magnetic field for HTS films as-grown and after irradiation by gold ions incident at 30, 60 and 88 MeV.

In-situ Stress Relaxation During Annealing of Amorphous Carbon Films

T. A. Friedmann and J. P. Sullivan

Motivation--Amorphous carbon thin films grown by pulsed laser deposition can have properties approaching those of diamond. In particular, we have measured thin films of this material that are 90% as hard and stiff as crystalline diamond classing them as the second hardest material known to man. In addition, these films are electrically resistive, have low friction coefficient, and have extremely low wear rates, thus earning the name of amorphous diamond.

One major limitation of these films is that very large compressive stresses (10 Gpa) are generated during growth. These stresses are intrinsic to the growth process yet they limit the ultimate film thickness to ~0.1-0.2 μm due to adhesion failure at the film substrate interface. This ultimately limits many applications of amorphous diamond (in particular tribological applications) since thicker films are often required.

Accomplishment--Previously, we found that simple thermal annealing treatments can *completely* relax the residual stress in these films. Surprisingly, the films retain their diamond-like nature with only minor changes in the bonding structure due to the annealing procedure

To obtain a more complete understanding of the stress relaxation in this material, we have applied an in situ technique (developed at Sandia) for measuring the residual stress reduction in these materials as a function of annealing time and temperature (see Fig. 1). From the data, we see that the stress reduction appears to follow an activated behavior such that the initial reduction in stress is quite rapid (seconds), followed by an exponential decay that extends over quite long time frames (days). Surprisingly, samples annealed at the highest temperatures actually become tensile - the first report ever of tensile films of this material.

Using this data, and inferences from other measurements of changes in the films with annealing, we have derived a simple model of the stress relaxation that has been fit to the data (see Fig. 1) over 4 decades in time and from 100 to 600 °C in temperature. The model shows that the energy barriers to stress relaxation are broadly distributed (0.5-3.3 eV) but peaked near 1.7 eV. This broad distribution is quite consistent with the amorphous structure of this material, that consists of carbon atoms in a range of bonding environments.

One interesting prediction of this model is that amorphous diamond samples should stress relax at room temperature over long time frames. Experimental measurements confirmed that indeed samples stored at room temperature for over 1.4 years showed reduced stress and the magnitude of the stress reduction was consistent with the model prediction.

Significance--A detailed understanding of the stress relaxation in amorphous diamond is emerging from this work. Importantly, this understanding is predictive and is being used to guide applications development for this new material. In particular, stress relief enables the production of arbitrarily thick films and very thin large-area free-standing membranes (see Fig. 2). We have demonstrated 11 μm thick films and thin free-standing membranes over 1 inch in diameter. These thick films and membranes have applications in tribological coatings, x-ray and/or electron transparent windows, and sensors. Sandia has applied for a patent on the stress-free amorphous diamond material.

Sponsors for various phases of this work include: LDRD, DP - Phys. Sci. & Tech.
Contact: Thomas A. Friedmann, Nanostructure and Semiconductor Physics Dept., 1112
Phone: (505) 844-6684, Fax: (505) 844-1197, E-mail: tafried@sandia.gov

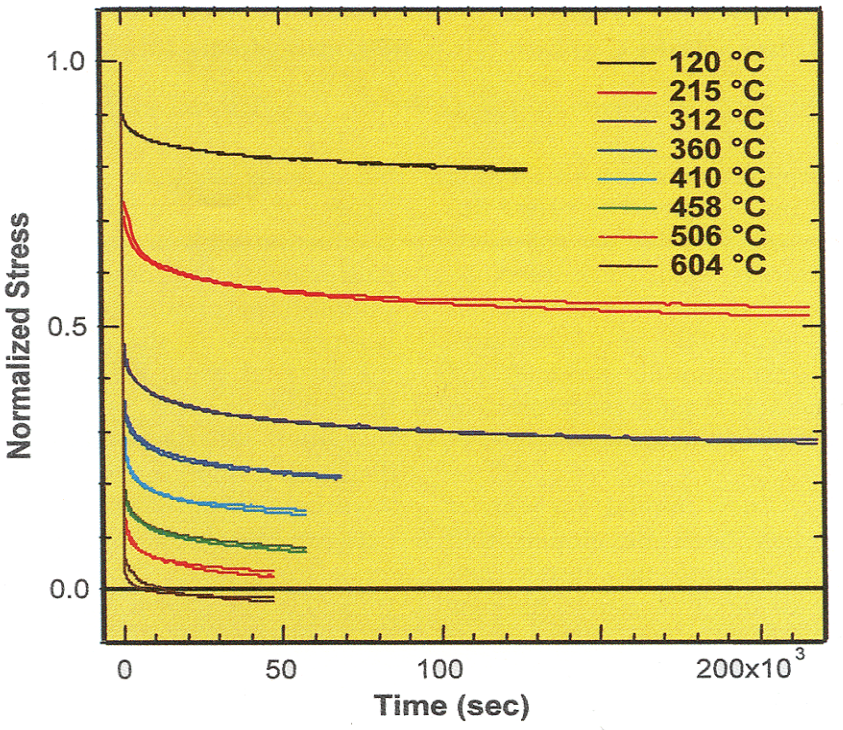

Figure 1. Measured stress relaxation as a function of time for annealed samples. Overlaying the data are curves derived from a fit to the stress relaxation model.

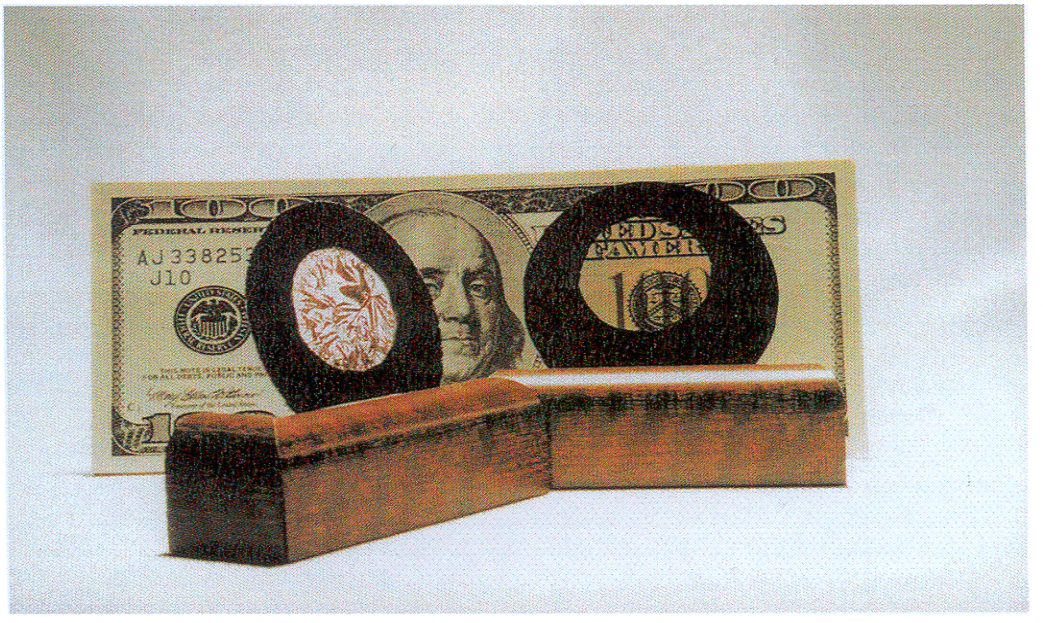

Figure 2. Two free-standing membranes of stress-free amorphous diamond. The membranes are 0.1 micrometers thick and one inch in diameter.

A Model for Hopping Conduction Between Extended Three-Fold Carbon Sites in Amorphous Diamond

J. P. Sullivan, T. A. Friedmann, R. G. Dunn, P. A. Schultz, and E. B. Stechel

Motivation--Amorphous diamond (a-D) is a new material with unique physical properties that make it particularly valuable for tribology, vacuum microelectronics, and, most recently, membrane-based sensors. Detailed understanding of the physical properties of a-D requires new understanding of the atomic structure, and this has been achieved through measurement of the electrical properties of this material.

Accomplishment--A new model for carrier transport in a-D has been developed that provides unique insight into the atomic and electronic structure of this material. This new understanding finally permits the explanation of some of the unusual electrical and optical properties of this material, including the observed dependence of electrical conductivity and film stress on anneal temperature, the anomalous optical absorption, and the spatial heterogeneity of the electrical conductivity.

Recent first principles calculations of the atomic structure of a-D indicate the material has an unusual bonding structure: the majority of the carbon atoms are four-fold coordinated, but embedded within this matrix are three-fold coordinated carbon atoms that tend to cluster in predominantly chain-like configurations (see Fig. 1). The carrier transport behavior follows directly from this atomic structure. The four-fold coordinated matrix phase has a wide band gap that approaches 5.5 eV. The three-fold coordinated material has a smaller local band gap, E*pi-pi**, that arises from the splitting of bonding and anti-bonding *pi* states. Importantly, E*pi-pi** varies with the number (N) of carbon atoms within the chain, as ~ 1/N. Carrier transport is due to thermally activated hopping between the extended three-fold carbon sites, but not all sites are equally important. The largest chains have the smallest E*pi-pi**, so the conduction path is determined by the shortest path between the longest three-fold sites in the sample. This conduction process leads to spatial heterogeneity in the observed conductivity of the material when the conduction path through the sample is short (~ 100 nm). Moreover, the logarithm of the conductivity is normally distributed, implying that - as the model predicts - variations in chain size, not the distance between chains, determines the conductivity.

It can also be shown that ripening of the chains by thermal annealing leads to both the observed increase in electrical conductivity and stress relaxation in this material. This model also neatly solves one dilemma in this material, the anomalous optical absorption which, unexpectedly, shows no sharp band edge as a function of photon energy. The model suggests that this absorption naturally arises from a distribution in three-fold carbon chains in which the number of chains decreases exponentially with increasing chain size (see Fig. 2). Finally, the dominant chain size which contributes to the electrical conductivity can be estimated from the model and is found to be 12 carbon atoms in size, which agrees very closely with the number derived from combined stress relaxation and electrical measurement.

Significance--The new model for transport in a-D explains the unusual optical and electrical properties of this material. The model also permits prediction of the atomic structure of the material based on readily measurable quantities. The behavior of this system may serve as a model for a large class of heterogeneous hopping conduction systems.

Sponsors for various phases of this work include: LDRD, DP - Phys. Sci & Tech.
Contact: John P. Sullivan, Advanced Materials and Devices Sciences Dept., 1153
Phone: (505) 845-9496, Fax: (505) 844-4045, E-mail: jpsulli@sandia.gov

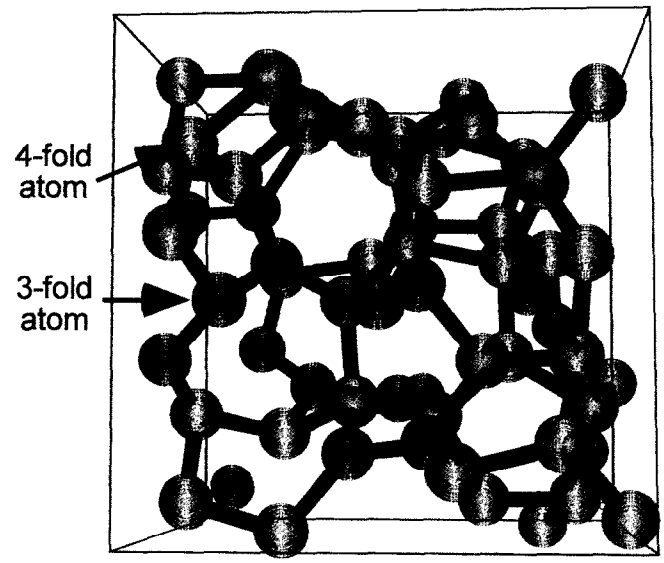

Figure 1. Atomic structure of amorphous diamond calculated from first principles for a material density of 3.1 g/cm^3. The four-fold coordinated carbon atoms are shown as gray, and the three-fold coordinated carbon atoms are shown as blue. The three-fold carbon atoms tend to link in chain-like configurations.

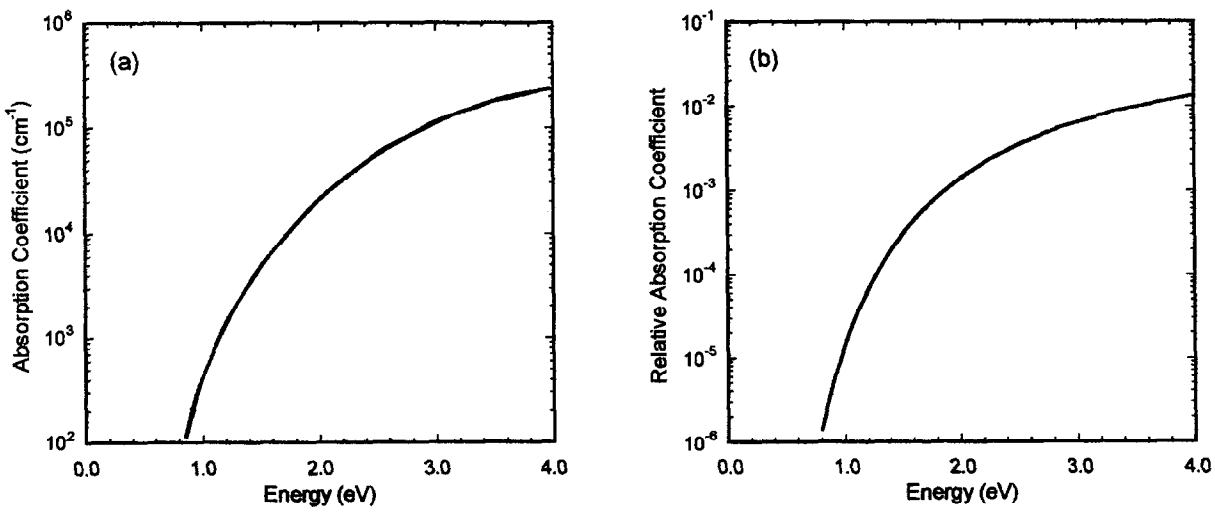

Figure 2. (a) Measured optical absorption for amorphous diamond (from Smith, J. Appl. Phys., 1984) and (b) predicted optical absorption based on a model of an exponential distribution of chain sizes.

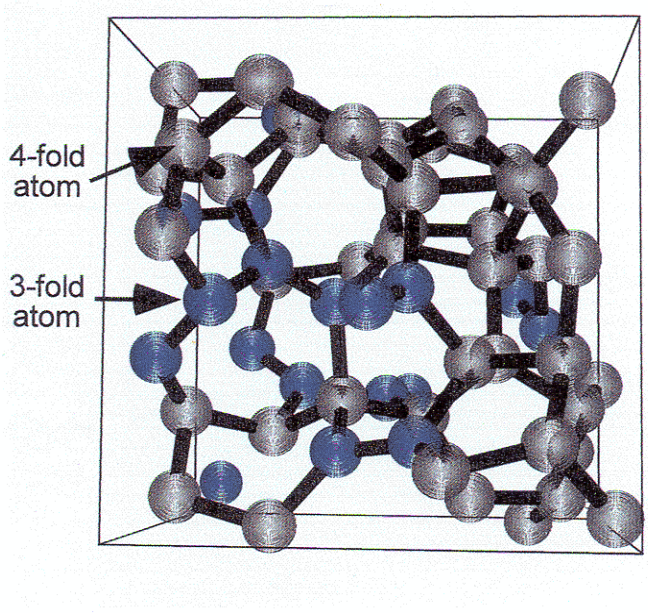

Figure 1. Atomic structure of amorphous diamond calculated from first principles for a material density of 3.1 g/cm^3. The four-fold coordinated carbon atoms are shown as gray, and the three-fold coordinated carbon atoms are shown as blue. The three-fold carbon atoms tend to link in chain-like configurations.

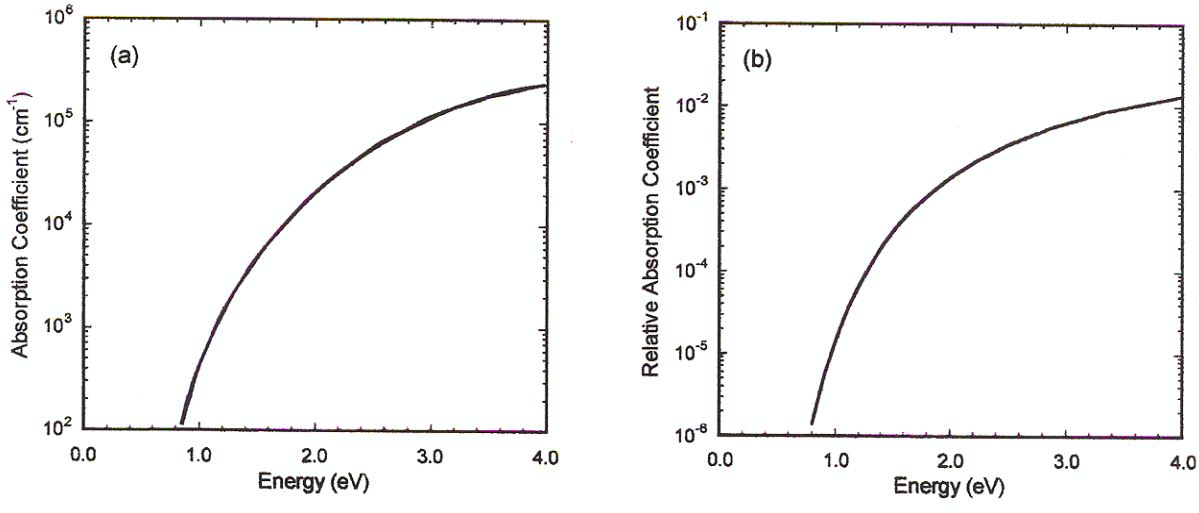

Figure 2. (a) Measured optical absorption for amorphous diamond (from Smith, J. Appl. Phys., 1984) and (b) predicted optical absorption based on a model of an exponential distribution of chain sizes.

Advanced Sensing Science

Swarm Intelligence Research

*G. Osbourn**

Motivation--The field of swarm intelligence (also known as collective intelligence or emergent behavior) has attracted much interest in the past decade. Swarms of simple, autonomous agents can exhibit complex collective behaviors by interacting with each other and with the environment. Such swarms typically do not have a "leader" or a command hierarchy, and also typically have no prior knowledge of the environment in which they operate. The complex and adaptive behavior of many interacting agents can be observed in natural systems (social insects, immune systems) and man-made systems (internet, financial markets). Swarms of autonomous agents provide a novel approach to achieving intelligent behavior from simple components, and can adapt to changing environmental conditions when the agents contain appropriate sensors. Swarms also provide robustness against the failure of some of the agents, and do so without the inefficiency associated with conventional hardware redundancy. These properties have motivated the development of software and hardware agent systems that exhibit useful and robust collective behaviors. Sandia National Laboratories has initiated an LDRD Grand Challenge project with the goal of developing swarm intelligence surety software and hardware systems for high consequence applications.

There are many issues to address in order to design useful swarm behaviors. A key issue is the design of effective agent communications. It is assumed here that communication bandwidth is limited, so that each agent can only exchange a limited amount of data per unit time with a limited number of the other swarm agents. Which of the available agents should communicate with each other, and what types of information should be exchanged to facilitate useful complex behaviors?

Accomplishment--We have developed the concept of a cluster network of agents that facilitates general purpose communication and navigation. There are two properties of the cluster network that are illustrated in Fig. 1. First, each agent uses a cluster algorithm to determine with which of the nearby agents it will communicate. Such clusterings are illustrated in the figure by connecting lines between the agents. The algorithm is chosen to ensure that every agent clusters with at least one other agent, yet the maximum possible number of cluster agents to communicate with is small. Second, a communication channel is maintained for any location of interest to the swarm. Each channel is used to exchange single numbers that represent the "cluster proximity" of each agent to the location of interest. These values provide a simple guide for navigation to any location that the swarm detects and monitors with a communication channel, since an agent can approach the location by simply moving in the direction of its cluster neighbor agents with decreasing proximity values. Each agent is also informed of the presence of a location of interest by valid proximity values on the relevant communication channel. We have tested the performance of this approach by computer simulation. We find that useful and robust swarm behaviors, e.g. finding and surrounding targets, emerge directly.

Significance--We have developed a general approach for agent communication and navigation. This approach is applicable to the control of autonomous robotic swarms.

*In collaboration with R. Robinett, Robotics Dept. 9000

Sponsors for various phases of this work include: LDRD

Contact: Gordon C. Osbourn, Vision Science, Pattern Recognition and Multisensor Algorithms Dept., 1155
Phone: (505) 844-8850, Fax: (505) 844-5459, E-mail: gcosbour@sandia.gov

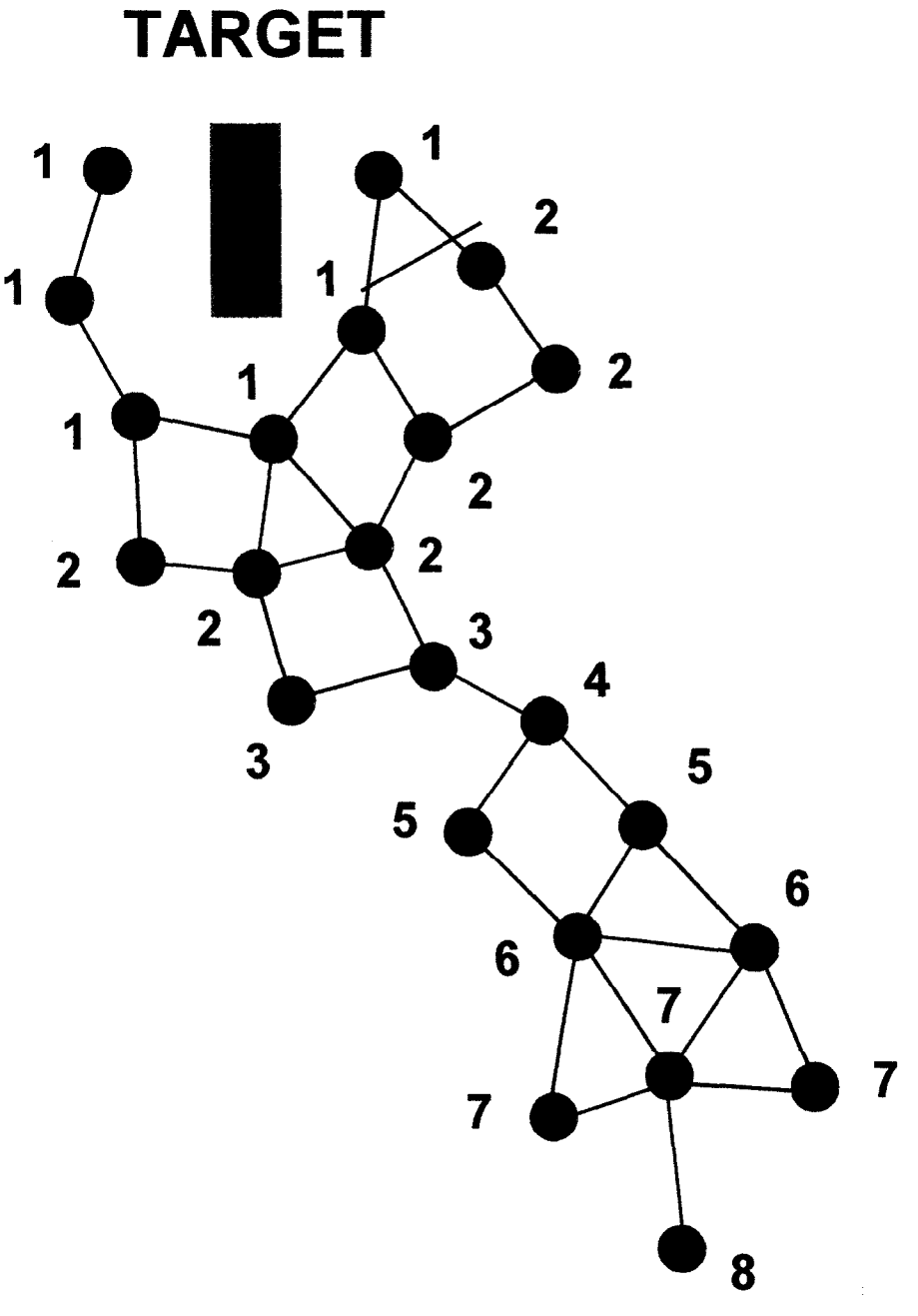

Figure 1. Cluster network for an agent swarm. The circles are agents and the blue bar is a target of interest. The numbers are computed proximity values for each agent relative to the target.

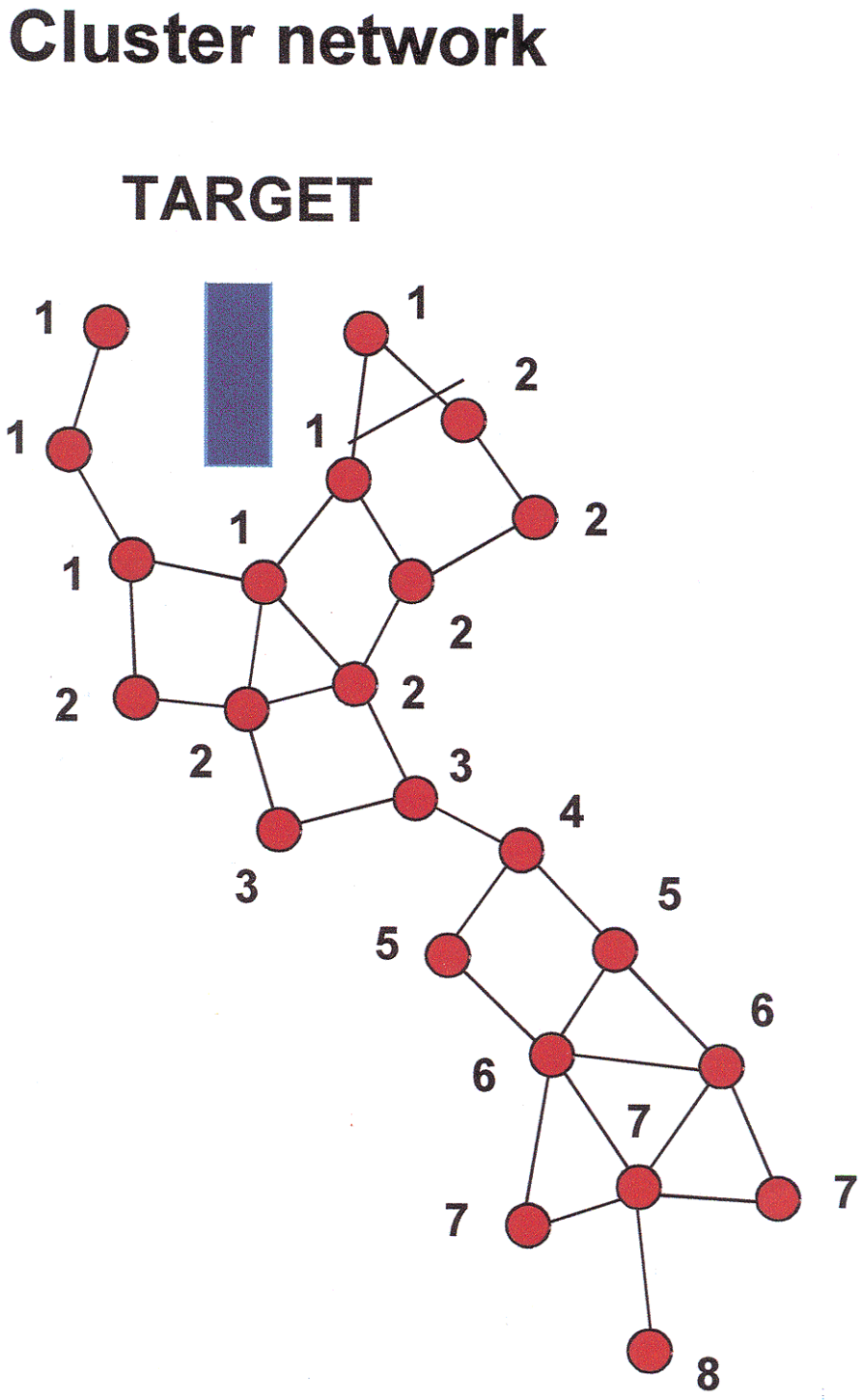

Figure 1. Cluster network for an agent swarm. The circles are agents and the blue bar is a target of interest. The numbers are computed proximity values for each agent relative to the target.

Diode-Laser-Based Blue Sources

*T. D. Raymond, W. J. Alford, M. H. Crawford, A. A. Allerman and R. E. Allman**

Motivation--Compact sources of coherent blue light with good beam quality are vital for advanced chemical sensors, high density optical storage devices, and projection display devices. Current commercially available sources are based on frequency-doubled near infrared diode lasers or frequency-doubled near infrared solid-state lasers pumped by diode lasers. It is highly desirable to develop sources that are significantly more efficient, have a smaller parts count, and are more compact. Toward that end we are exploring intracavity frequency doubling of Vertical External Cavity Surface Emitting Lasers (VECSELs) based on semiconductors.

Accomplishment--We have developed an optically pumped blue light source based on a frequency doubled VECSEL. As shown in Fig. 1, the cavity is comprised of two pieces: a semiconductor element incorporating a distributed Bragg reflector (DBR) and a multiple quantum well gain region, and a nonlinear optical crystal with polished and dielectric coated surfaces. The high reflectivity (HR), DBR mirror and the HR, curved output surface of the crystal form a stable laser cavity which leads to high intracavity power and good beam quality. The semiconductor wafer is grown in house by metal-organic vapor phase epitaxy. The DBR is made up of 27 alternating layers of quarter-wave thick GaAs and AlAs and provides >99.9% reflectivity around 980 nm. Atop the DBR is grown 15 repetitions of $Al_{0.08}Ga_{0.92}As$ pump light absorbing layers, 8-nm thick compressively-strained $In_{0.16}Ga_{0.84}As$ quantum wells, and GaAsP strain-compensating layers. The quantum wells are positioned to coincide with the electric field maxima formed by the standing wave in the laser cavity. Pump photons are absorbed in the $Al_{0.08}Ga_{0.92}As$ layers creating carriers that then pump the quantum wells. Finally, a thick $Al_{0.5}Ga_{0.5}As$ layer mitigates carrier diffusion to the wafer surface, and an $In_{0.49}Ga_{0.51}P$ cap layer prevents Al oxidation. The $KNbO_3$ nonlinear crystal is oriented to provide noncritical phasematching for frequency doubling of 980 nm light near room temperature. The flat intracavity surface is antireflection (AR) coated for minimum reflectivity, while the HR surface is polished convex with a 15 mm radius of curvature. The cavity supports a TEM_{oo} mode ~90 microns in diameter. The semiconductor wafer is mounted with heat sink compound onto a copper mount and a thermoelectric cooler (TEC). The wafer is pumped by a 0.5 Watt, 803 nm, single-stripe diode laser incident at Brewster's angle and focussed to a spot ~100 microns in diameter. Although the mount is held at 0C, the excitation region is 10's of degrees higher. Improvements in thermal control may obviate the need for the TEC.

Figure 2 shows the performance of this device under typical operating conditions. Intracavity 980 nm power > 10 Watts leads to milliWatts of blue output. Upwards of 5 mW of 490 nm light has been produced in a high-quality circular beam with 10 milli-radian divergence and > 1% pump-to-blue conversion efficiency.

Significance--This first demonstration of efficient frequency doubling of VECSELs opens the way for extremely compact, and reliable blue sources. While optical pumping looks very promising, we are pursing direct electrical pumping of the quantum wells as this may improve the efficiency and compactness.

*In collaboration with Christopher Bailey, Org. 08358

Sponsors for various phases of this work include: LDRD

Contact: T. D. Raymond, Laser, Optics and Remote Sensing, 1128
Phone: (505) 844-9166, Fax: (505) 844-5459, E-mail: tdraymo@sandia.gov

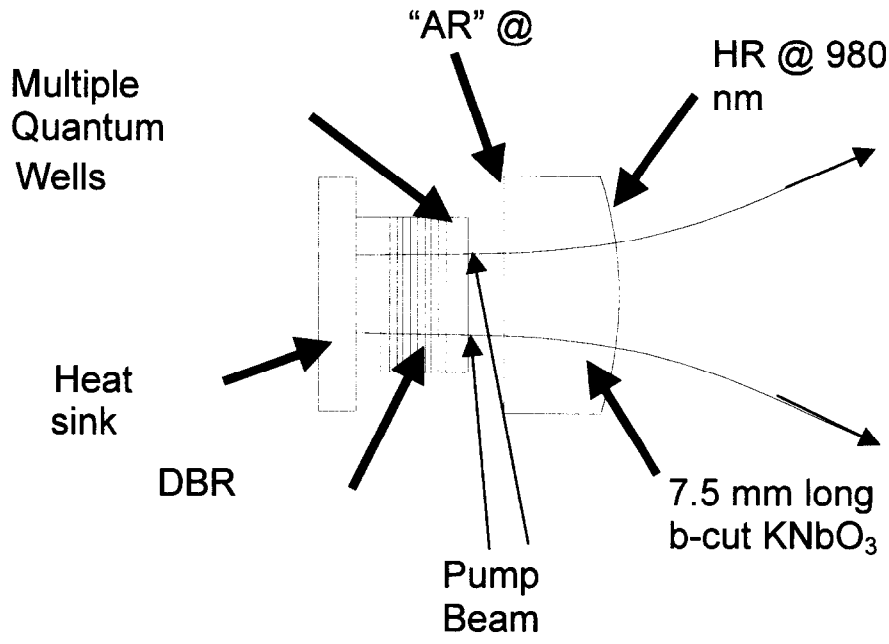

Figure 1. The optically pumped intracavity frequency doubled VECSEL is quite compact. The semiconductor wafer structure provides a high reflector (DBR) and the gain material forming part of the cavity. The nonlinear crystal with its polished and coated surfaces completes the cavity providing transverse mode control for high beam quality.

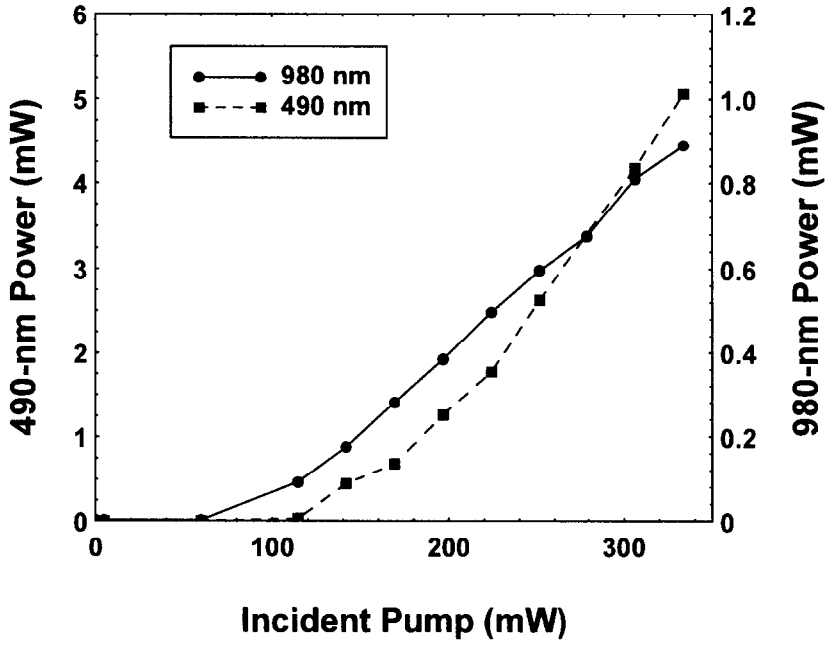

Figure 2. This device produces up to 5 mW of high quality light suitable for chemical sensing.

Physics of Photosensitivity in Novel Thin Films

*K. Simmons-Potter and B. G. Potter, Jr.**

Motivation--Photosensitive (PS) materials permanently change their refractive index upon exposure to intense light, enabling a wide range of integrated optical device structures to be rapidly patterned via a single, direct-write optical process step. We are attempting to merge our development of highly photosensitive films with existing efforts to introduce optical subsystems into the enduring stockpile to produce relevant photonic devices with unique functionality.

Accomplishment--We have demonstrated the ability to produce highly photosensitive germanosilicate thin films using a novel sputtering approach which enables us to obtain the largest reported Δn (-5x10-3) in as-synthesized materials. In addition, control of processing parameters has allowed us to engineer, at an atomic level, the defect interactions responsible for the PS response of our films. As a result, we have the unique ability to control not only the magnitude of the optical response of our films but also the sign of the induced refractive index change. As can be seen in Fig. 1 we can produce films, using a novel reactive-atmosphere sputtering process, which exhibit either a large negative or a large positive Δn upon exposure to the appropriate wavelength of laser radiation. The novelty of such control of PS optical response has enabled us to produce a number of proof-of-principle devices including: in-plane Bragg grating waveguide structures useful as reflective or filtering elements, multimode channel waveguides capable of trapping and routing guided light on an optical chip, and a never-before-demonstrated out-of-plane diffractive grating capable of diffracting normally incident light (Fig. 2). This latter device is of particular interest as a routing element in complex optical paths used in optical weaklink designs. We are presently working to understand the thermal stability of the structural defects that produce the PS optical response observed in our diffractive gratings to address this potential application.

Significance--Optical data transmission and signal manipulation offer significant advantages over more conventional, electronic approaches. Commercial telecommunications and remote sensing technologies rely on the ultrafast data transfer rates, insensitivity to signal interference, and robust physical design that characterize photonic systems based on both optical fibers and waveguides. These characteristics can also provide enhanced nuclear weapons safety in DOE/DP applications as efforts continue at Sandia to integrate optical systems into the enduring stockpile. In this context, optical componentry can provide intrinsically high signal discrimination (for safety and use control) and insensitivity to electrical disruption (e.g. lightning strikes). Our PS glass thin films have the advantages of a large photo-induced Δn and long-term room-temperature stability of the PS defects. We are now exploring the viability of these new glasses for a variety of DOE/DP optical applications, including use as an optical thermal weaklink material. In this case, critical nuclear weapon control circuitry is rendered inoperable under abnormal thermal environments through the destruction of a photo-imprinted grating structure.

*In collaboration with Sandia Defense Programs AF/DS initiative

Sponsors for various phases of this work include: DP - Phys. Sci. & Tech.

Contact: Kelly Simmons-Potter, Lasers, Optics and Remote Sensing Dept., 1128
Phone: (505) 844-1271, Fax: (505) 844-5459, E-mail: kspotte@sandia.gov

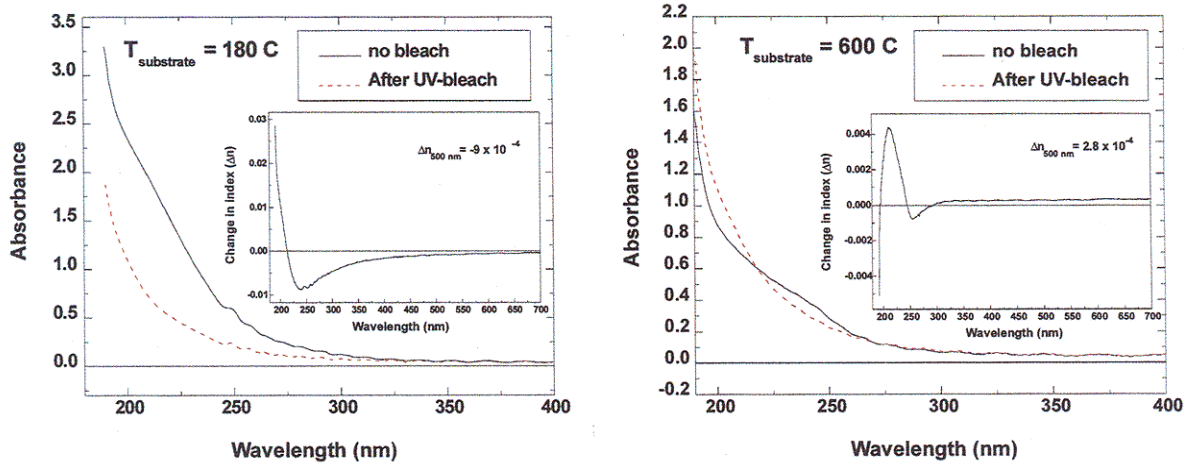

Figure 1. Representative UV absorption spectra taken on Sandia PS films. Both as-deposited spectra (solid lines) and spectra following optical exposure (dashed lines) are depicted. Insets show calculated optically-induced Δn in samples exhibiting a negative Δn over operational wavelengths (left figure) and those exhibiting a positive Dn over operational wavelengths (right figure).

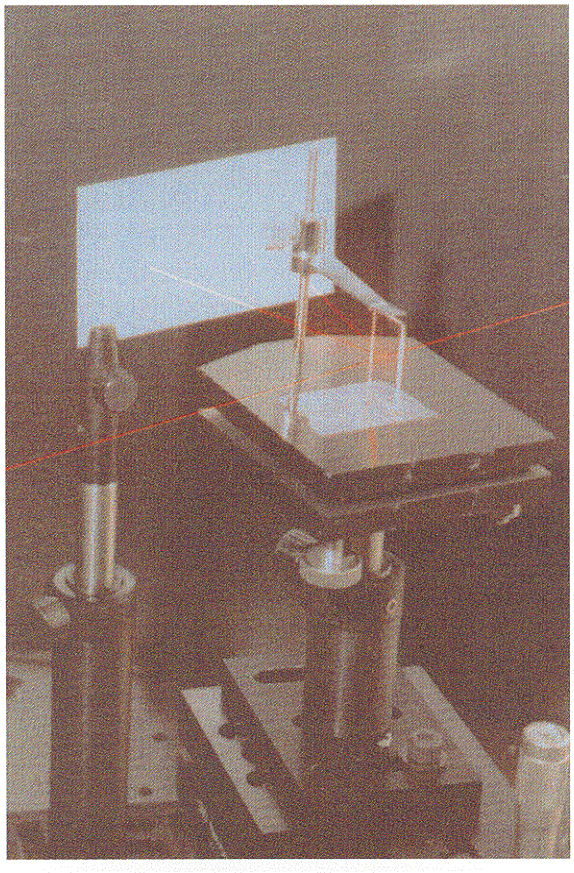

Figure 2. Out-of-plane diffraction of an incident 632.8 nm He-Ne beam into the +1 and -1 order by an optically-imprinted phase grating in a Sandia photosensitive thin film.

Magnetic-Field-Induced Optical Transmittance in Colloidal Suspensions

J. E. Martin, K. M. Hill, and C. P. Tigges

Motivation--When a magnetic field is applied to a suspension of ferromagnetic particles the particles magnetize and form column-like structures. The concomitant increase in the suspension viscosity is of interest because of the industrial applications for magnetorheological fluids (MRFs), such as clutches and vibration dampers. However, even in the quiescent state MRFs might have useful properties, due to significant anisotropies in the fluid permeability, conductivity, and optical transmittance. We have examined the magnetic-field-induced optical transmittance in an MRF of black magnetic particles for two reasons. First, this effect might be useful in applications such as optical-fiber-based magnetic field sensors, and second, it allows us to test theoretical predictions of the kinetics of structure formation in MRFs. The standard theory invokes thermal fluctuations as the mechanism which drives structure formation.

Accomplishment--Our investigations of field-induced optical transmittance included both simulations and experiments. The simulations follow the evolution of structure in an MRF immediately after exposure to a magnetic field. The experiments measure the transmission of light through an MRF exposed to a magnetic field.

The effect of magnetic-field-induced optical transmittance is illustrated in the simulated structures in Fig. 1, which show that the optical attenuation length - the distance over which slightly more than half the incident light is absorbed - increases as the square root of time. The time dependence of the optical transmittance is shown in Fig. 2. These simulations show that structure formation is actually driven by defects, in contrast to analytical theories, which invoke thermal motions as the key factor.

The experiments we performed indicate that a magnetic field can increase the optical transmittance by a factor of 10^5. The increase in the optical transmittance, Fig. 3, is consistent with simulations, but the plateau transmittance is much smaller than expected, indicating particle friction effects that are not accounted for by theory or simulation. Particle friction pins evolving structures into local energy minima, causing the plateau transmittance to be much smaller than expected.

Significance--The simulations demonstrate that defect structures - not thermal fluctuations - drive structure formation in induced dipolar systems, and give an experimentally verified prediction for the time dependence of optical transmittance. However, comparison with experiment demonstrates that particle friction, which is not accounted for in extant models, plays a significant role in structure formation.

Our experiments also show that the field-induced optical transmittance is reversible, suggesting possible applications. The time scale of the experiments shown herein is long, but reasonable response times could be achieved in a device consisting of 10 nm particles suspended in a low viscosity liquid at high applied fields. For example, for a liquid with a viscosity of water, and a field of 5000 Gauss, a response time of 1 ms would be obtained. When the field is turned off, particle diffusion would render this suspension opaque in ~ 100 ns. The rapid reversibility of the induced transmittance with nanoclusters of iron or gadolinium, makes the use of this effect for optical-fiber-based magnetic field sensors a possibility. Such devices would be extremely sensitive to the field direction and homogeneity and would be useful in measuring fields, and thus currents, in a safe fashion, e.g. near high tension power lines.

Sponsors for various phases of this work include: BES
Contact: James E. Martin, Nanostructures and Advanced Materials Chemistry, 1152
Phone: (505) 844-9125, Fax: (505) 844-4045, E-mail: jmartin@sandia.gov

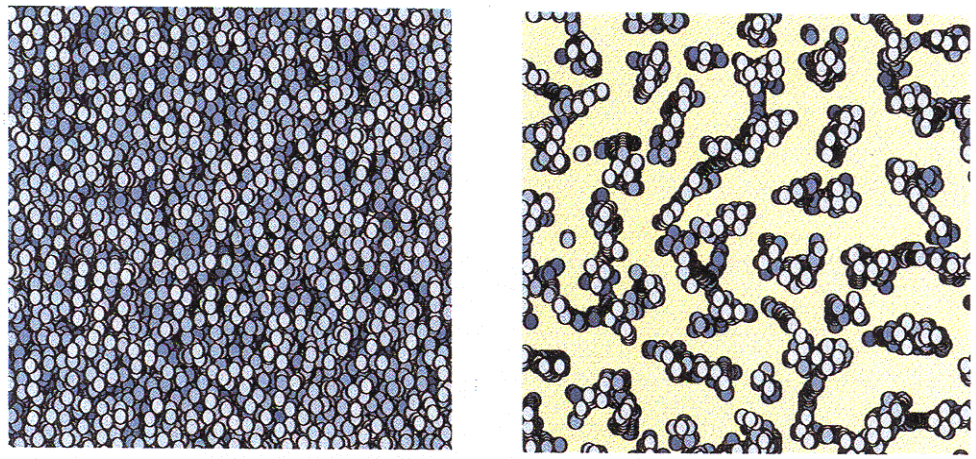

Figure 1. Simulation of field-induced optical transmittance.

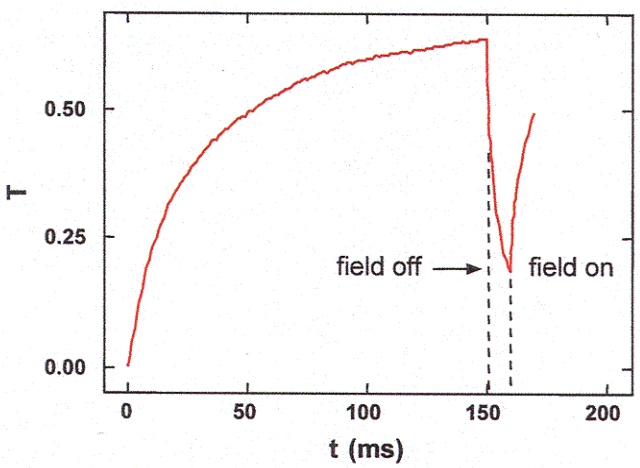

Figure 2. Transmittance from simulation data showing switching behavior.

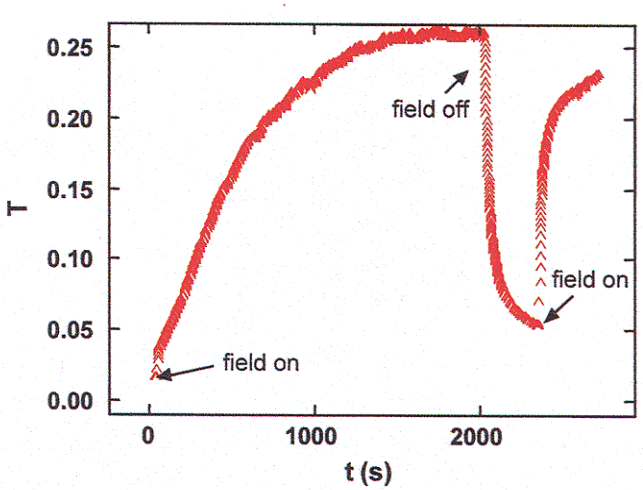

Figure 3. Optical transmittance of a system of 0.2 vol. % Fe_3O_4 particles in a $5.2x10^{-3}$ T field.

Robust Mid-IR Light Source for Chemical Sensing

*M. W. Kimmel and T. D. Raymond**

Motivation--Remote chemical detection of hydrocarbons permits the monitoring of air quality in urban areas, the optimization of chemical processes to minimize emissions, and the reduction of fuel losses due to leaks at refineries, pump stations and pipelines. For example, active sensing using backscatter gas imaging has been demonstrated to rapidly visualize methane leaks in pipeline joints. Critical to the application of this technique and other remote sensing methods to hydrocarbons is the availability of robust, narrow bandwidth coherent light sources tunable in the 3-3.5 μm range. While some sources, such as optical parametric oscillators (OPOs) are available, their frequency stability generally requires the use of frequency standards or wavemeters to ensure the light is resonant with the absorption features of interest and may require optical cavities to be interferometrically stable. For man-portable devices, such sources are unwieldy and impractical.

Accomplishment--We have developed a simple mid-IR source based on optical parametric amplification and a fiber optic Bragg grating filter that will eliminate the need for frequency standards. This source has the additional feature that it has sufficient tunability to permit rapid tuning across absorption features of interest.

Our source uses a diode-pumped high repetition rate, Q-switched Nd:YAG laser to pump a 50 mm-long piece of periodically poled $LiNbO_3$ (PPLN). The period of the PPLN is chosen to produce signal and idler waves at 1.55 and 3.37 μm, respectively, when pumped at 1.06 μm. The device works in three stages as shown conceptually in Fig. 1. The first stage acts as a broadband source of mid-IR light produced via optical parametric generation (OPG). Approximately 0.5 mJ of light from the laser is focussed to a spot about 100 mm diameter into the PPLN. The tight focus and 10 ns pump pulse width create sufficient gain in the PPLN to amplify quantum noise to the mJ level. The light so produced has a much broader bandwidth than is useful for direct detection of chemicals but can be centered on an absorption feature of interest via temperature control of the PPLN. The second stage is a single-mode fiber, into which a Bragg narrow bandwidth reflector (0.5 cm^{-1} FWHM) has been permanently written. These reflectors have the desirable properties that the reflection bandwidth is narrow and the center frequency is very stable to temperature and vibration variations. When the reflected 1.55 μm light is amplified in the final stage, another PPLN crystal acting as an optical parametric amplifier (OPA), the desired narrow bandwidth 3.37μm light is simultaneously produced. In our setup, the OPG and OPA crystals are one in the same. Tuning of the amplified light over several wavenumbers is readily accomplished by stretching the fiber grating. Figure 2 shows the spectral distributions of the Bragg-reflected OPG and the narrow bandwidth OPA stages.

Significance--This demonstration of the production of narrow bandwidth, tunable light suitable for remote hydrocarbon detection without the use of an OPO or a frequency reference represents a major breakthrough in compact remote sensing technology. Hand held sensors could soon be available to image gas clouds.

*In collaboration with T. J. Kulp, Org. 08366
Sponsors for various phases of this work include: Gas Research Institute
Contact: Mark W. Kimmel, Laser, Optics and Remote Sensing, 1128
Phone: (505) 844-4757, Fax: (505) 844-5459, E-mail: mwkimme@sandia.gov

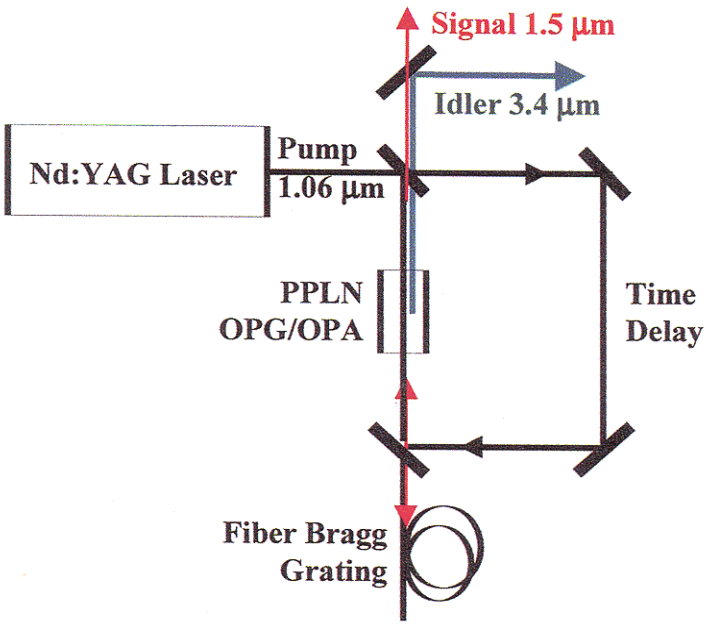

Figure 1. A Q-switched Nd:YAG laser pumps a PPLN crystal that acts as an optical parametric generator (OPG) to generate broadband 1.55 µm light. This is filtered with a fiber Bragg grating. The PPLN serves as an optical parametric amplifier for this light when pumped by a time-delayed portion of the pump light. The amplification produces the desired 3.37 µm light as the idler wave.

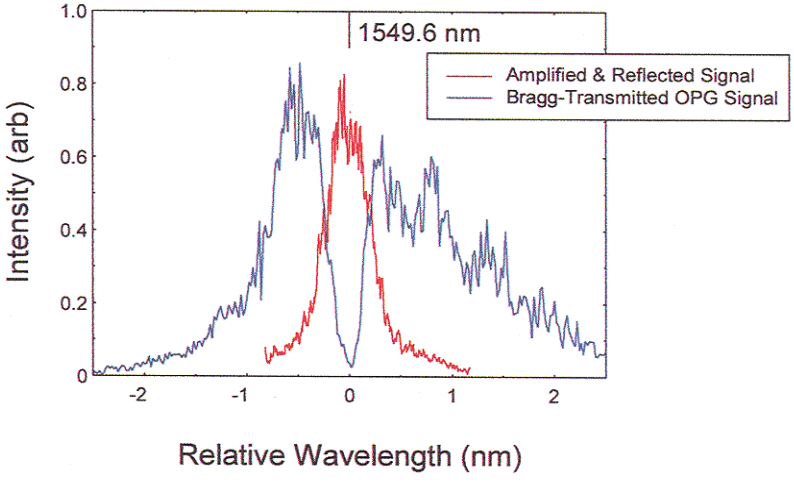

Figure 2. The broader curve shows the broadband spectrum of the OPG output as transmitted through the fiber Bragg grating; the narrow notch at 0 is the reflected portion of the broadband light. The narrow curve is the amplified reflected signal.

Modeling Broad-Bandwidth, Nanosecond Optical Parametric Oscillators

*A. V. Smith**

Motivation--Optical parametric oscillators (OPO's) are versatile devices for converting fixed wavelength laser light to tunable light. Our previous computer model for narrow bandwidth (<1 GHz) OPO's proved valuable for understanding OPO behavior and stimulated OPO design innovation. However, most nanosecond OPO's have a bandwidth of several wavenumbers, a situation not modeled by the previous methods. We have recently developed models that allow broad bandwidths.

Accomplishment--Optical parametric amplification is an interaction of three optical waves that boosts signal and idler waves at the expense of a pump wave. Necessary conditions are that the frequencies obey (fs + fi = fp) and that a medium with a nonlinear response at optical frequencies mediate the mixing. With positive feedback, this gain can drive an optical parametric oscillator. Figure 1 shows the simple OPO that is the subject of our model. Mirrors feed back the signal wave, and a strong pump wave drives the process in a nonlinear crystal. In our previous OPO models, we assumed the three waves were nearly monochromatic, meaning their phase and amplitude varied slowly compared with the crystal transit time. This was appropriate for injection-seeded OPO's that start from monochromatic pump and signal light supplied by lasers. However, most nanosecond OPO's are not seeded. Instead, oscillation builds by amplification of the vacuum quantum fields. These fields are infinitely broadband and so are structured on time scales short compared with the crystal transit time. Consequently, the three interacting waves all develop high frequency structure. Because the waves propagate with different group velocities, the structures slide past one another as they propagate through the crystal. This group velocity effect must be included in any model of broad-bandwidth OPO's because it determines the operating bandwidth of the OPO, and it strongly influences the modulation properties of the output light. We have developed three new plane-wave models that include this effect. They give identical results, but each has its advantages. One method is based on expansion in terms of the longitudinal modes of the empty OPO cavity. This is the method often applied to broad-bandwidth lasers so it provides a historical connection to other models. However, it is much slower than our other two models that are based on split-step integration of the mixing equations using FFT propagation. The latter run in a few minutes on a 300 MHz Pentium II so we can easily make the many runs necessary to study the statistical properties of these OPO's.

Significance--This new design tool will promote better understanding of broad-bandwidth OPO's and foster improved designs. Already it has provided support for our previous experimental observation that unseeded, nanosecond OPO's generate unique light with a broad spectrum but little amplitude modulation (see Fig. 2). Such light may have practical applications in interferometry, in imaging, and in suppressing stimulated light scattering. A version of the new model is included in my nonlinear optics software package, SNLO, which has over 400 users worldwide.

*In collaboration with M. S. Bowers of Aculight Corp., Bothell, WA
Sponsors for various phases of this work include: LDRD, DP - Phys. Sci & Tech.
Contact: Arlee V. Smith, Laser, Optics and Remote Sensing Dept., 1128
Phone: (505) 844-5810, Fax: (505) 844-5459, E-mail: arlsmit@sandia.gov

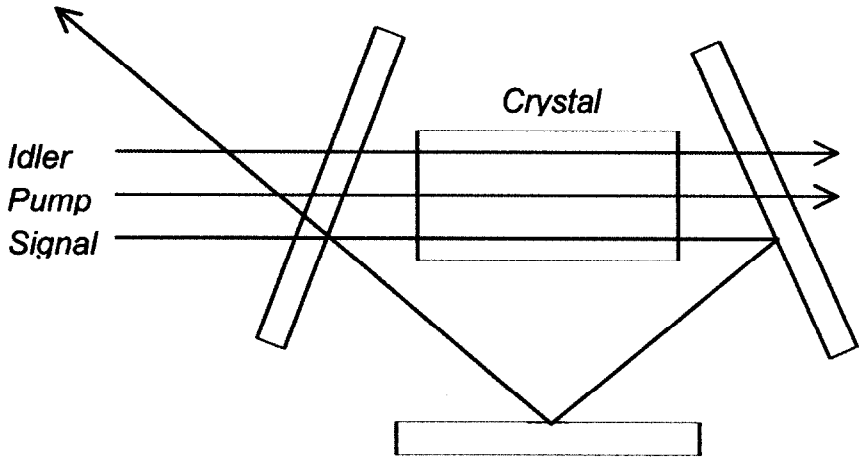

Figure 1. Configuration of the OPO modeled for broad bandwidth operation. The input idler and signal waves include the broad-bandwidth quantum vacuum contributions.

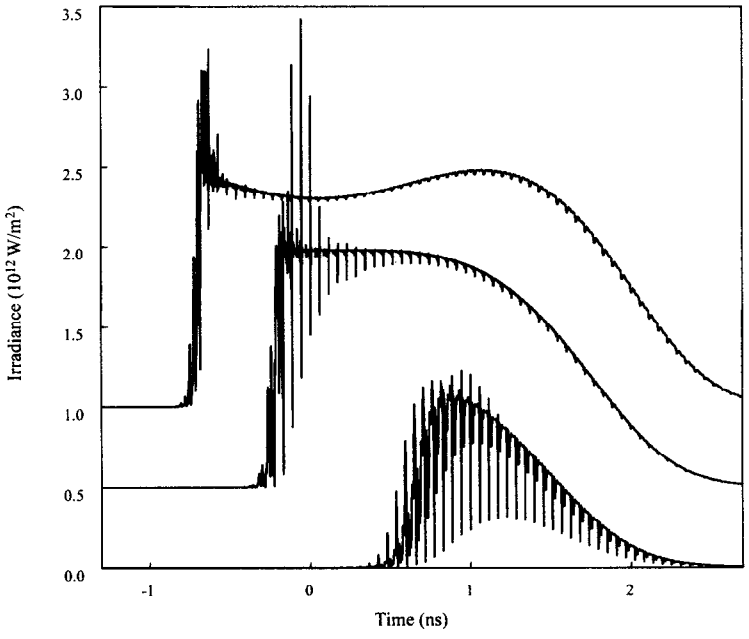

Figure 2. Calculated irradiance versus time for a broad-bandwidth, nanosecond OPO pumped near threshold and at two and four times threshold (bottom to top traces). The spectrum does not change much from low to high pump but the correlation of the modes does, resulting in nearly phase modulated light at high pump levels.

IntraLaser Rheophotonics: A New Tool for Microfluidics

*P. L. Gourley, O. A. Akhil, G. C. Copeland, J. A. Dunne, J. S. Hendricks, and A. E. McDonald**

Motivation--The ability to probe fluid behavior and analyze its constituents at a microscopic level is of current interest for basic scientific understanding and for emerging engineering applications. As dimensions of fluid confining structures shrink to micron sizes and below, new tools must be developed to gain access to microfluidic properties such as average fluid velocity and velocity distribution, and to study basic phenomenon such as the influence of material surfaces on these parameters. Microfabricated fluidic structures are receiving considerable interest for detecting chemical species in surveillance and environmental applications, and for assaying cellular and molecular species for biomedical applications. Microfluidic structures have been successfully made with glass and silicon materials. However, these materials have been limited to mechanical functions such as flow channels and valves. We have integrated compound semiconductors with glass micromechanical structures to form microfluidic cavities that also perform optical functions. These enable generating light and sensing fluid properties by sensitive spectroscopic measurements of physical interaction between fluid and optical field or chemical interactions between molecular species and the material surfaces.

Accomplishment--By using a surface-emitting semiconductor geometry, we were able to incorporate fluid flow inside a laser microcavity for the first time. The microfluidic structures comprise microlithographically defined channels in glass substrates with vertical cavity surface-emitters. These structures emit coherent, intense light from microscopic region where the flow of fluid and light intersect. The microcavities are dichroic, to allow visual imaging of the flowing species while simultaneously recording optical or lasing spectra at longer wavelengths. The microfluidics were experimentally investigated by flowing fluids of various viscosity into the channels. The fluid velocity was found to be linearly dependent upon the hydraulic conductivity of the channels, as predicted by the Hagen-Pouiselle equation. Some differences were observed between the magnitude of the theoretically predicted velocity and that measured experimentally. These differences are due in part to the condition of the solid surfaces that form the channels and can be controlled by surface chemistry.

Significance--A new tool for probing microfluidic phenomenon has been constructed and successfully tested for its utility and ease of use. Preliminary studies of basic fluid dynamics in the microcavity show agreement with standard theory for the dependence of velocity on channel geometry. Additional studies are needed to understand the role of material surfaces. Intracavity laser microfluidics confers significant advantages for high throughput screening of chemical or biological warfare agents for defense applications or assaying cells, particulates and fluid analytes for biomedical applications. Using this new tool, we have demonstrated a simple flow cytometer using blood cells and normal human astrocytes and glioblastoma cells found in brain tissue. These initial demonstrations provide a basis for more substantive research in cellular biology. With Steve Skirboll, MD of the UNM School of Medicine, we have initiated a collaboration via the Sandia-University Research Program to investigate use of the microcytometer as a surgical tool in the precise determination of tumor margins.

*In collaboration with Steve Skirboll, MD, UNM School of Medicine

Sponsors for various phases of this work include: BES, LDRD, DP - Phys. Sci. & Tech., AEP

Contact: Paul L. Gourley, Nanostructure and Semiconductor Physics Dept., 1112
Phone: (505) 844-5806, Fax: (505) 844-1197, E-mail: plgour@sandia.gov

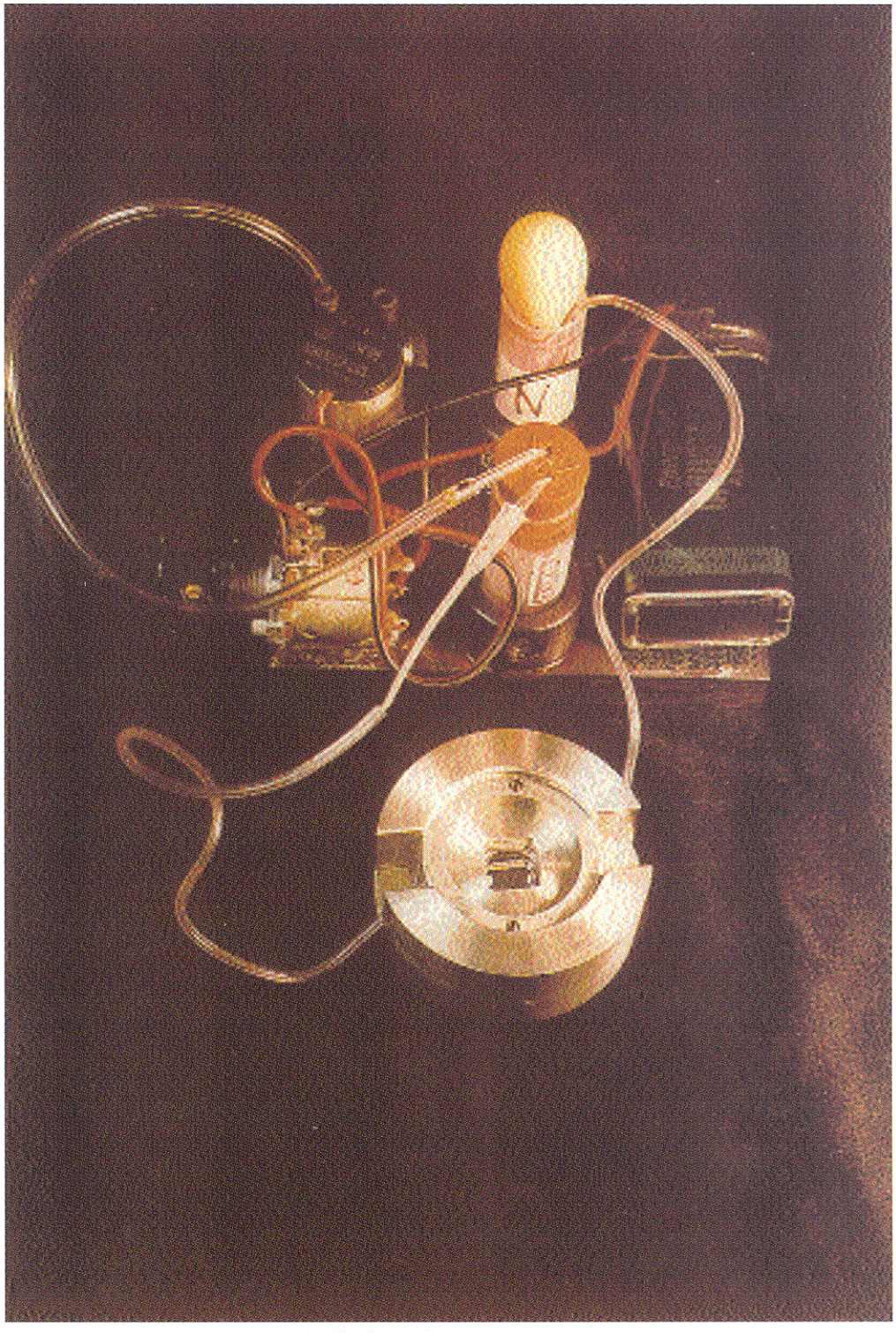

Figure 1. Photograph of an intracavity laser flow cell (lower cylindrical object) with inlet and outlet flow lines connected to a miniature vacuum pump.

Science of Semiconductor Technologies

Experimental Advances in Demonstration of a Practical Double Electron Layer Tunneling Transistor (DELTT)

J. A. Simmons, J. S. Moon, M. A. Bount, J. R. Wendt, and J. L. Reno

Motivation--Quantum transistors based on resonant tunneling have long been of interest due to their multi-functionality, low power, and intrinsically high speed, possibly providing a superior future alternative to today's conventional electronics. Sandia recently developed the double electron layer tunneling transistor, or DELTT. The DELTT operates using resonant tunneling between the two electron layers in an AlGaAs/GaAs double quantum well (DQW) heterostructure. Because both electron layers are strictly two-dimensional, the densities of each layer can be easily modulated with surface gates, controlling the tunneling. Unlike previous tunneling transistors, the DELTT is entirely planar in structure, meaning it is scalable and can be reliably fabricated in large numbers. However, in order for the DELTT to find use in practical applications, a number of obstacles must still be overcome. One of these is the ability to fabricate DELTTs with sufficiently low parasitics to take advantage of their intrinsically high speed. In general, this requires DELTTs with submicron features. Because the DELTT fabrication process entails a flip-chip technique, registration of submicron features on both sides of the structure is a non-trivial task.

Accomplishment--Figure 1(a) shows a schematic of the DELTT. Independent ohmic contacts to the two electron layers are formed by diffusing metallic contacts to both layers, and then depleting electrons from the layer one does not wish to contact, using a metallic depletion gate. While a submicron top side gate is straightforward, a submicron back side gate is a challenge: due to the fringing of electric fields, the distance from gate to electron layer must also be submicron. We have demonstrated the ability to fabricate DELTTs with electron-beam written submicron gates on both sides of active epitaxial layers as thin as 0.24 microns. In the process, the top side features are fabricated first, using a top side alignment mark to register the electron beam writing. The sample is then epoxied top side down onto a host GaAs or Si substrate. The original substrate is thinned using a chemical etch which stops on a grown-in stop etch layer in the structure. Gates are then electron beam written on the exposed back side surface. Because the epitaxial layers are sufficiently thin that the electron beam can easily penetrate them, the top side alignment marks, now buried beneath the epitaxial layers, are also used for the back side electron beam writing. This allows alignment of features on the two sides with an accuracy of a few 100 Å. Figure 1(b) shows a side view of a test structure made using this technique, with electron beam written gates on both sides. Figure 2(a) shows a top view of a working DELTT device written using this technique. I-V data from this device is shown in Fig. 2(b), demonstrating that working DELTTs with good electrical characteristics can be made with this technique.

Significance--The fabrication of working devices with submicron features demonstrates that DELTTs with small parasitics are feasible. Hence devices which are not limited by large RC time constants, but rather take full advantage of the intrinsically high speeds of the tunneling process, are possible. DELTTs designed for speed measurements using microwave probes have been fabricated and are currently being measured. The demonstration of high speed DELTTs will significantly bolster the case for their use in practical applications.

Sponsors for various phases of this work include: LDRD, DP - Phys. Sci. & Tech.
Contact: Jerry A. Simmons, Nanostructure and Semiconductor Physics Dept., 1112
Phone: (505) 844-8402, Fax: (505) 844-1197, E-mail: jsimmon@sandia.gov

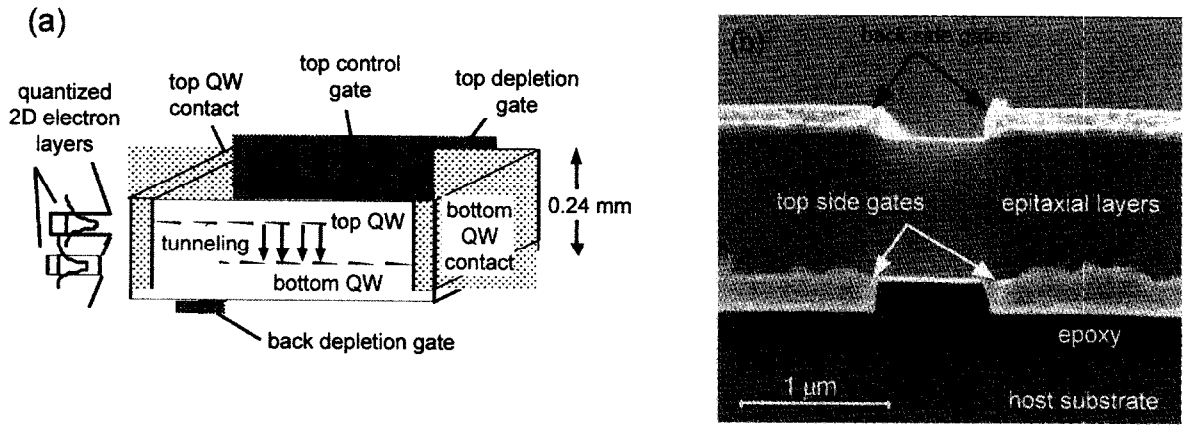

Figure 1. (a) Schematic of the DELTT. The source contacts the top QW only, while the drain contacts the bottom QW only. Individual QW contacts are formed by gate-depletion of the QW one does not wish to contact. Tunneling is controlled by biasing the control gate. Our flip-chip processing technique allows placement of back side gates only 0.24 μm from the bottom QW. At left is a sketch of the band structure. (b) Side view, after cleaving, of a test structure with electron-beam written gates on each side of the epitaxial layers. After flip-chip processing, the top side gates are against the epoxy and buried under the 1.0 μm thick epitaxial layers. Accuracy of the top-to-back alignment is a few 100 Å. Irregularities in the top side gate metal are due to cleaving.

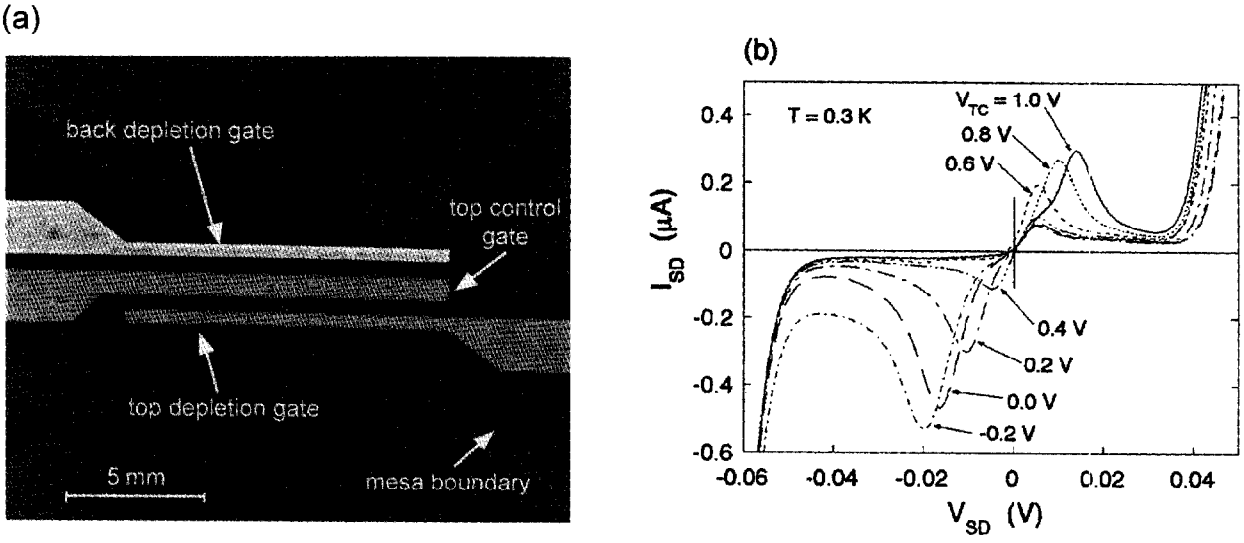

Figure 2. (a) Top view of a DELTT device fabricated using electron beam writing. Because the thickness of the epitaxial layers is only 0.24 μm, the electron beam can easily penetrate them, making the mesa and top side gates clearly visible even though they lie on the other side. The back-side gate, which now lies on the exposed surface, is slightly brighter. The depletion gates are 0.5 μm long and separated from the control gate by 0.5 μm. (b) For the device shown in (a), source-drain currents I_{SD} as a function of source-drain bias V_{SD} at several different control gate voltages V_{TC}. The position and height of the resonant current peak is clearly controlled by V_{TC}, demonstrating that the DELTT can be produced in submicron geometries with low parasitics.

Feasibility of Room-Temperature Double Electron Layer Tunneling Transistors (DELTT)

S. K. Lyo, J. A. Simmons, and J. L. Reno

Motivation--The DELTT is a planar resonant tunneling transistor which takes advantage of the sharp I-V characteristics of two-dimensional to two-dimensional electron tunneling. Large peak-to-valley ratios of the tunneling current at low temperatures arise from the restricted phase space imposed by simultaneous energy-momentum conservation in two dimensions. While 77 K DELTTs have been successfully demonstrated at Sandia, room temperature DELTTs require further work due to thermal and phonon broadening. The feasibility of room temperature DELTTs is assessed.

Accomplishment--A planar quantum transistor DELTT has been developed at Sandia and operates successfully at 77 K. Development of DELTTs at room temperature, however, has required more effort due to the unexpectedly broad I-V charateristics. In order to investigate the origin of this broadening and assess the feasibility of achieving a room temperature DELTT, we have calculated microscopically the tunneling current between two asymmetric quantum wells (QWs) as a function of DC bias between the two QWs. We have examined the mechanism of resonant and nonresonant tunneling and the sources of the room temperature broadening of the I-V curve. Desirable structures for high peak-to-valley ratio DELTTs have been studied based on this theory.

In our model, momentum and energy dissipation in tunneling arises from electron-impurity, electron-electron and electron-phonon scattering. Figure 1 displays the calculated current at 77 K and 300 K for a 120-125-120 Å $GaAs/Al_{0.3}Ga_{0.7}As$ double QWs (sample 1) with 8 and $2x10^{11}cm^{-2}$ electron densities in the QWs. For impurity broadening, a phenomenological width of 10 meV is used for both QWs. Other intrinsic interactions are calculated microscopically. When the effect of the in-plane resistance is included, the theoretical I-V curves become skewed to the right as shown by the observed data at 77 K in Fig. 2. Here, the current rises above 50 mV due to a leakage over the depletion gate. At 300 K, the LO-phonon contribution is dominant and the effect of the impurity is small as seen from Fig. 1. The peak-to-valley ratio and thus the efficiency of DELTT is determined by the position of the second resonance (not shown in Fig. 1) arising from tunneling into the second sublevel of the right QW. It is desirable to have this peak as far above the first peak as possible. It is also important to have the ground sublevel of the right QW much above that of the left QW to maintain a maximum charge difference. Several structures have been identified where the separation of the second and ground sublevels are as much as 150 meV or larger. However, there is an optimum separation, because if the second sublevel is too close to the continuum, the current into this level becomes too large, reducing the efficiency.

Significance--Theoretical studies for the I-V curve for resonant tunneling provide information about the maximum attainable peak-to-valley ratio and the current. The basic limitation to this ratio arises mainly from large electron-LO-phonon broadening at room temperature. The theoretical limit for the efficiency of DELTT can be estimated by calculating the I-V curves for optimum structures.

Sponsors for various phases of this work include: LDRD, DP - Phys. Sci. & Tech.
Contact: S. Ken Lyo, Semiconductor Material and Device Sciences Dept., 1113
Phone: (505) 844-3718, Fax: (505) 844-1197, E-mail: sklyo@sandia.gov

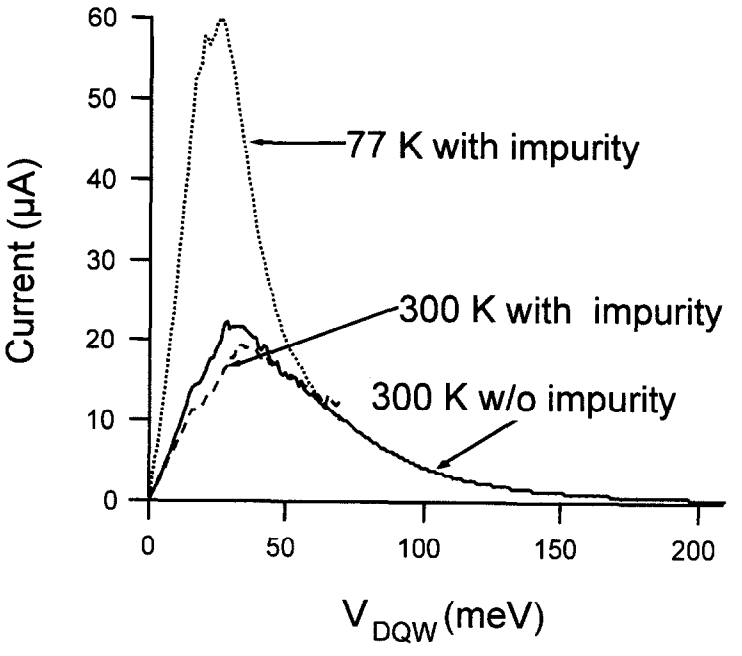

Figure 1. Calculated tunneling current as a function of the bias voltage at 77 K and 300K for sample 1. Curves with impurity scattering (dotted and dashed curves) are plotted up to 70 mV. The intrinsic current (solid curve) with electron-electron and electron-LO-phonon scattering is plotted up to 210 mV. The effect of the impurity scattering is negligible at 300 K above 70 mV.

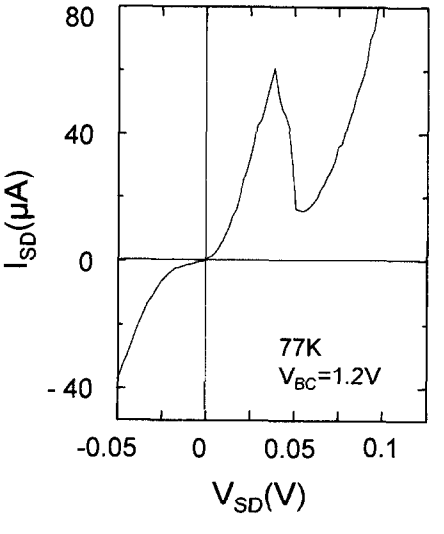

Figure 2. Observed tunneling current from sample 1 as a function of the source-drain voltage at 77 K.

Electronic Structure of Extended Defects in AlGaInN

A. F. Wright and K. Leung

Motivation--GaN and its alloys with AlN and InN are rapidly becoming the dominant material system for making optical emitters operating in the green-to-ultraviolet region of the spectrum. Due to the lack of a lattice-matched substrate, nitride films typically contain large numbers of extended defects such as stacking faults and threading dislocations. While these defects exist to some extent in all semiconductor films, nitride-based light-emitting diodes, for example, are able to tolerate defect densities 100,000 times higher than diodes made from other semiconductor compounds. This surprising result suggests that either group-III nitride materials are not affected by extended defects, or the defects themselves have very unusual properties. One of the most important unanswered questions in this regard is whether dislocations introduce defect levels into the GaN band gap. If they do, then charge carriers (electrons and holes) should recombine non-radiatively at the dislocation drastically reducing the overall radiative efficiency of the material. To answer this question, we have performed state-of-the-art, electronic-structure calculations for a threading edge dislocation in GaN.

Accomplishment--In order to calculate the electronic structure of a dislocation, it is first necessary to know the arrangement of atoms at the dislocation core. Because no experimental information is available, the core structure was determined as part of our electronic structure calculations. In general, the correct structure is the one having the lowest formation energy. However, it is important to note that this energy can depend not only on the structure itself, but also on the growth conditions and the doping in the surrounding material. These dependencies are well understood for the case of point defects in semiconductors, but have not been considered before in theoretical studies of dislocations. Our calculations show that consideration of these effects are crucial in finding the most stable core structure. As an example, our results show that a structure having gallium vacancies at the core is most stable when the crystal is grown under nitrogen-rich conditions with n-type doping. With p-type doping, however, the most stable structure is one without vacancies (see Fig. 1). Another prediction from these calculations is that dislocations in GaN should be charged when dopants are present in the surrounding material. This result challenges previous assumptions about dislocation behavior in semiconductors, yet evidence from recent experimental studies clearly confirms our prediction. To further examine this feature, we have begun to perform Monte Carlo simulations of an edge dislocation in the presence of background dopants. These simulations show that the line charge on the dislocation is strongly dependent on the doping concentration (see Fig. 2). In addition, the charge on individual defect sites is found to vary from one site to another, and this oscillation is also found to be dependent on the doping concentration.

Significance--Continued progress in the development of optical and electronic devices based on the group-III nitrides will rely on improving our understanding of their underlying physics. Their surprising tolerance of extended defects - a feature unique among group IV and III-V compound semiconductors - not only challenges us to broaden our understanding of nitride compounds, but also forces us to re-examine our assumptions of how dislocations behave in other semiconductor systems.

Sponsors for various phases of this work include: LDRD
Contact: Alan F. Wright, Semiconductor Material and Device Sciences Dept., 1113
Phone: (505) 844-0445, Fax: (505) 844-1197, E-mail: afwrigh@sandia.gov

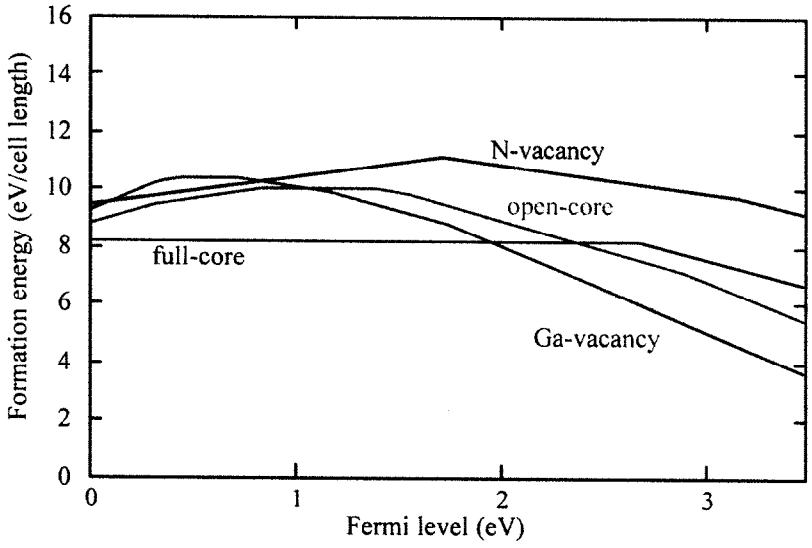

Figure 1. Formation energy versus Fermi level for 4 possible core structures of an edge dislocation in GaN. In n-type material, the Fermi level will be near 3.45 eV and the Ga-vacancy core structure is predicted to be most stable. In p-type material, the Fermi level will be near 0.1 eV and the full-core structure is predicted to be most stable.

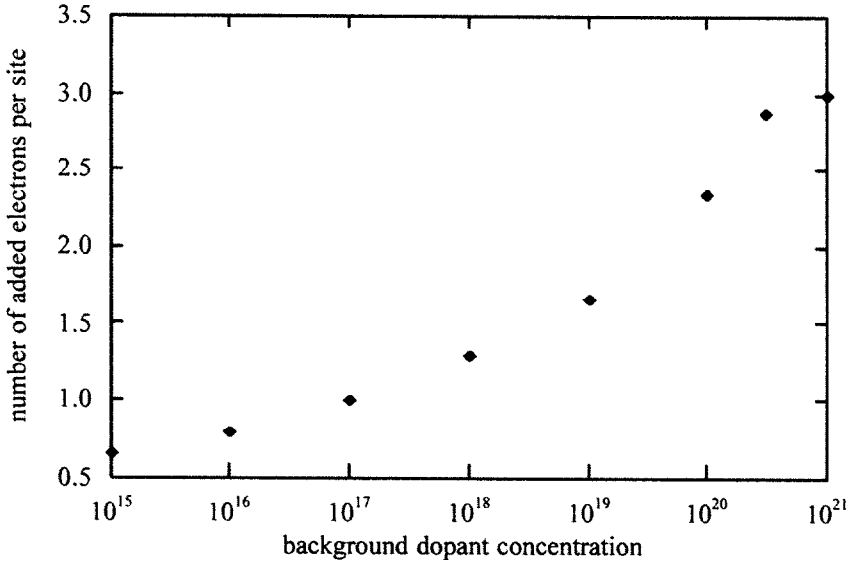

Figure 2. Number of added electrons per defect site along an edge dislocation in GaN, with the Ga-vacancy structure, as a function of the background donor concentration. Each site can accommodate up to three added electrons. Note that the number of electrons varies from site to site so the values in the plot are not necessarily integers.

Scanning Cathodoluminescence Studies of GaN Thin Films

N. Missert, C. H. Seager, J. Han, D. M. Follstaedt, M. H. Crawford, and R. G. Copeland

Motivation--GaN-based thin films have recently shown great promise as sources for both blue and ultraviolet light emission. The fabrication of low-cost, efficient LEDs and lasers relies on the ability to grow high quality films on commercially available substrates. So far, the substrate of choice has been c-plane sapphire, which has a 12% lattice mismatch to GaN. This large lattice mismatch results in a high density of dislocations which thread from the interface between the film and substrate to the surface of the film in order to accommodate small tilts and rotations between neighboring crystalline grains. Such crystalline imperfections may provide sites for non-radiative recombination and/or trap impurities which allow light emission at lower energy. Understanding how the efficiency, spatial distribution and spectral content of the luminescence correlate with the threading dislocation density is therefore important in order to optimize film growth for device applications.

Accomplishment--We have used scanning cathodoluminescence to study the lateral and vertical distribution of radiative and non-radiative recombination sites in GaN thin films grown by MOCVD. Our system uses the electron beam in a conventional scanning electron microscope to excite electron-hole pairs. An optical fiber coupled to a photomultiplier tube or spectrometer detects the light emitted as the pairs recombine. Digital imaging of the light emitted as the electron beam scans across the film surface provides a two dimensional map of the luminescence with submicron spatial resolution for low beam energies. Increasing the electron beam energy probes greater depths within the film, allowing a three dimensional map of the luminescence efficiency. Unintentionally doped films reveal two spectral components to the luminescence; a UV contribution from band-edge emission and a yellow contribution from a deep level defect band. Our scanning technique shows that the UV luminescence from a film with a relatively low dislocation density of $10^9/cm^2$ is highly non-uniform. Equally distributed areas of radiative and non-radiative recombination are evident on a submicron scale as shown in Fig. 1. An image of the yellow luminescence shown in Fig. 2 displays the same heterogeneity, in fact the yellow luminescence comes from the same spatial locations as the UV. A film with a factor of two higher dislocation density has a luminescence efficiency lower by a factor of two in the UV and lower by a factor of ten in the yellow. These results imply that dislocations alone are not the source of yellow luminescence. In addition, the magnitude and spatial distribution of the UV and yellow luminescence do not change significantly with depth, suggesting that the threading dislocations provide non-radiative recombination sites.

Significance--These studies of the spatial distribution and spectral content of the cathodoluminescence in GaN thin films show that the crystalline quality and impurity content can dramatically influence the efficiency of light emission. Our results indicate that because threading dislocations likely provide non-radiative recombination sites, a decrease in the dislocation density will lead to more efficient UV sources. Furthermore, because the yellow luminescence originates from the same spatial location as the UV with a magnitude that is not correlated with the dislocation density, an independent defect such as an impurity must be responsible.

Sponsors for various phases of this work include: LDRD, DARPA
Contact: Nancy Missert, Nanostructure and Semiconductor Physics Dept., 1112
Phone: (505) 844-2234, Fax: (505) 844-1197, E-mail: namisse@sandia.gov

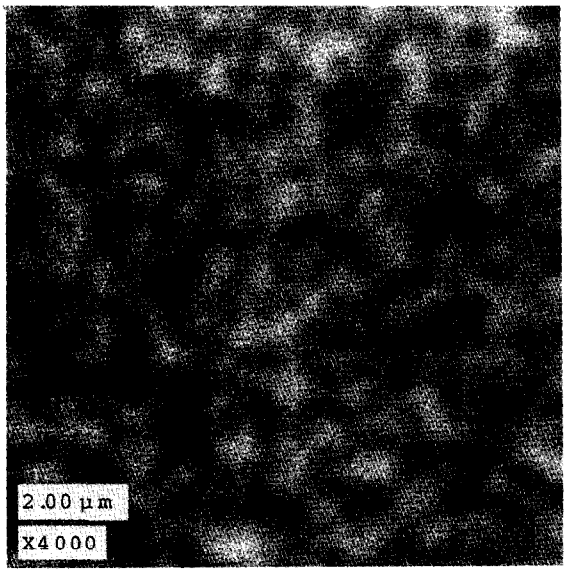

Figure 1. Scanning cathodoluminescence image of GaN film in UV taken at 5 kV and 300 pA.

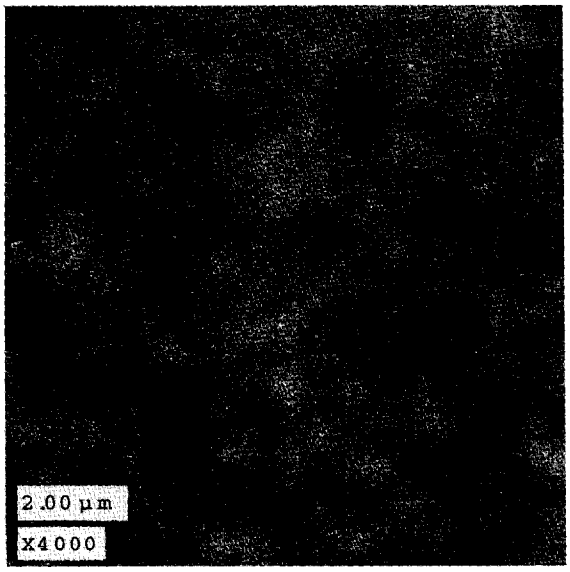

Figure 2. Scanning cathodoluminescence image of GaN film in yellow taken at 5 kV and 300 pA.

Localized Versus Extended States in InGaAsN Photovoltaic Materials

*E. D. Jones, A. A. Allerman, S. R. Kurtz, N. A. Modine, and A. F. Wright**

Motivation--A new semiconductor alloy system, InGaAsN, has been identified as a key candidate material for multi-junction solar cells with efficiencies greater than 40%. The introduction of small amounts of nitrogen (~2%) in the InGaAs alloy system greatly reduces the band gap energy, with reductions approaching 0.5 eV! With the appropriate ratio of indium to nitrogen concentrations, InGaAsN can be lattice matched to GaAs. Lattice matching allows the design of multi-junction cells without the inherent problems found in strained cells. The initial portion of this research program is thus aimed at understanding the fundamental nature of the effect of adding substitutional isoelectronic nitrogen atoms for arsenic.

Accomplishment--A series of InGaAsN alloys with varying nitrogen concentrations with the indium content adjusted to provide lattice matched conditions were grown using metal organic chemical vapor deposition (MOCVD) reactors. In the first study we investigated the photoluminescence energy and line shape for varying growth conditions. Because of the importance and emphasis on materials exhibiting 1 eV band gap energies, we found that nitrogen and indium concentrations of about 2% and 6% respectively, gave the desired results, i.e., correct band gap energy and lattice matched conditions. Studies of the photoluminescence line width and intensity for these samples were performed in order to determine the optimum growth parameters and conditions. Significant increase in the photoluminescence intensity was observed from these samples following a post-growth anneal. A 4-K photoluminescence spectrum is shown in Fig. 1. The 4-K band gap energy is about 1150 meV and at 300K, the band gap energy decreases to about 1100 meV. In order to differentiate impurity from band-to-band luminescence transitions, low temperature (4K) photoluminescence studies were made as a function of pressure. The pressure dependence of the band gap energy between ambient and 108 kbar is shown in Fig. 2. A miniature diamond anvil cell with a methanol/ethanol/water pressure medium in the ratio of 16/3/1 was used to generate the pressure. Also shown in the figure is a theoretical calculation for the change in band gap energy dependence of the lowest energy conduction band using a first principles local density approximation to density functional for 2% nitrogen in GaAsN. The agreement between theory and experiment is good considering that theoretical refinements to the calculation are necessary, i.e., addition of indium, etc. However, the pressure results shown in Fig. 2 indicate band-to-band and not impurity behavior.

Significance--Modern satellite performance depends critically on the development of high efficiency solar cells. Calculations show that incorporating a 1 eV band gap material into existing GaAs-based multi-junction tandem solar cells can increase the overall solar cell efficiency by as much as 10%, with maximum theoretical efficiencies for the multi-junction cell greater than 40%. These increased efficiencies will lead to smaller (and lighter) solar cell panels for spaced-based applications.

*In collaboration with NREL, LBNL, USAF/Phillips, EMCORE

Sponsors for various phases of this work include: BES, LDRD, CRADA

Contact: Eric D. Jones, Semiconductor Material and Device Sciences, 1113
Phone: (505) 844-8752, Fax: (505) 844-3211, E-mail: edjones@sandia.gov

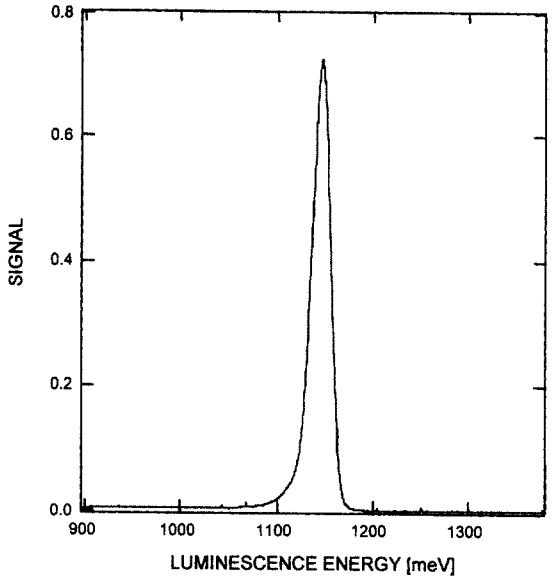

Figure 1. Low temperature (4K) photoluminescence spectrum for an $In_{0.06}Ga_{0.94}As_{0.98}N_{0.02}$ epilayer film lattice matched to GaAs. The band gap energy is 1150 meV and the full-width-at-half-maximum is about 22 meV.

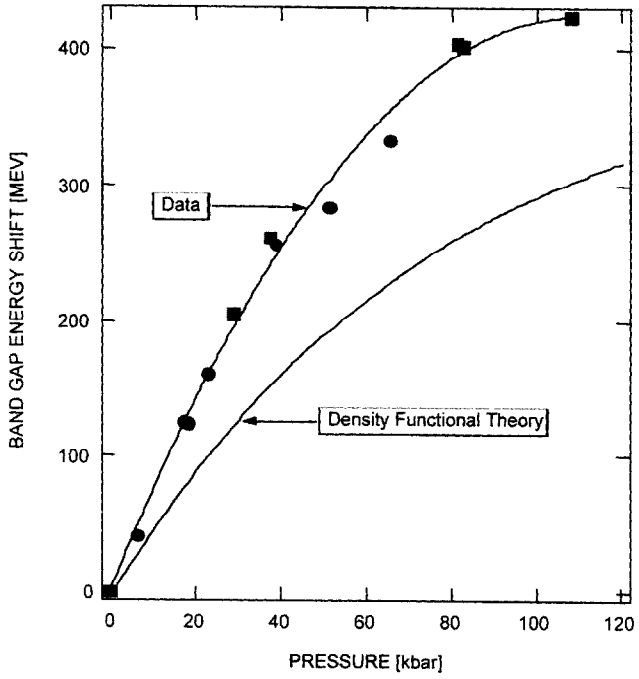

Figure 2. Experimental and theoretical comparisons of the change in the low temperature band gap energy versus pressure.

The Ion Electron Emission Microscope, or Nuclear Microscopy without Focusing the Beam

B. Doyle, D. S. Walsh, and G. Vizkelethy

Motivation--Nuclear microprobe analysis (NMA) is currently performed by focusing MeV ions onto a sample and then scanning the beam in a flying spot analysis. Nuclear, atomic or charge collection signals that are generated by the beam are the detected signal. Analytical NMA has reached a 0.3-0.9 μm limit of beam-spot resolution that can be obtained using a variety of magnetic and electrostatic focusing lenses. No significant improvements in resolution have been reported in over 5 years. The reasons for lack of improvement in NMA resolution are numerous and include: 1) difficulties in manufacturing ion optic lenses with required accuracy; 2) difficulties in vibration isolation; and 3) difficulties in focusing high magnetic rigidity and/or poor chromaticity ions from cyclotrons, linacs or older Van de Graaff style electrostatic accelerators. A method of performing high spatial resolution nuclear microprobe analyses is needed to extend Sandia's radiation effects nuclear microscopy program into higher energy regimes where our scanning microprobe system cannot operate.

Accomplishment--We have developed an entirely different way to perform NMA which does not require focusing of the MeV ions at all, but rather, records the position where the ions strike the sample by imaging the secondary electrons that they generate. With this new approach, one uses the MeV ions as a flood beam, and image by projecting the secondary electrons generated by each ion using a Photon Electron Emission Microscope (PEEM). These position signals are recorded with a channeltron+resistive anode Position Sensitive Detector (PSD) and then put into coincidence with the IBA signals caused by the ions as they penetrate the sample. This new technique is called Ion-Electron Emission Microscopy or IEEM. We have demonstrated IEEM for secondary electron emission intensity imaging of simple targets. The Ion Electron Emission Microscope or IEEM concept was shown to clearly work in a 1-μm resolution mode. This resolution and system efficiency (10s of %) are reasonably close to those predicted by theory. IBICC measurements were also performed on Au-coated PIN diodes. IEEM-based IBICC required coincidence of the charge collection signal with the X-Y signal of the SEs, and this measurement therefore represented a successful proof of principle experiment for the new IEEM technique.

Significance--This project was started at Sandia because of the need to perform radiation effects microscopy measurements on a 1.9 MeV/amu heavy ion RFQ linac booster which was recently added to our tandem. IEEM makes this project possible, and extends the use of radiation effects microscopy into ion energy regimes more like those of space environments. IEEM with high-energy ions can be used, for example, to directly compare charge-collection and single event upset maps of radiation-tolerant devices with broad-beam upset cross-section measurements of those same devices. This kind of information will provide more insight into upset phenomena, and invaluable feedback to Sandia's design and development processes for radiation hardened microelectronics devices.

Sponsors for various phases of this work include: DP - Phys. Sci. & Tech., LDRD
Contact: Barney L. Doyle, Radiation Solid Interactions and Processing Dept., 1111
Phone: (505) 844-7588, Fax: (505) 844-7775, E-mail: bldoyle@sandia.gov

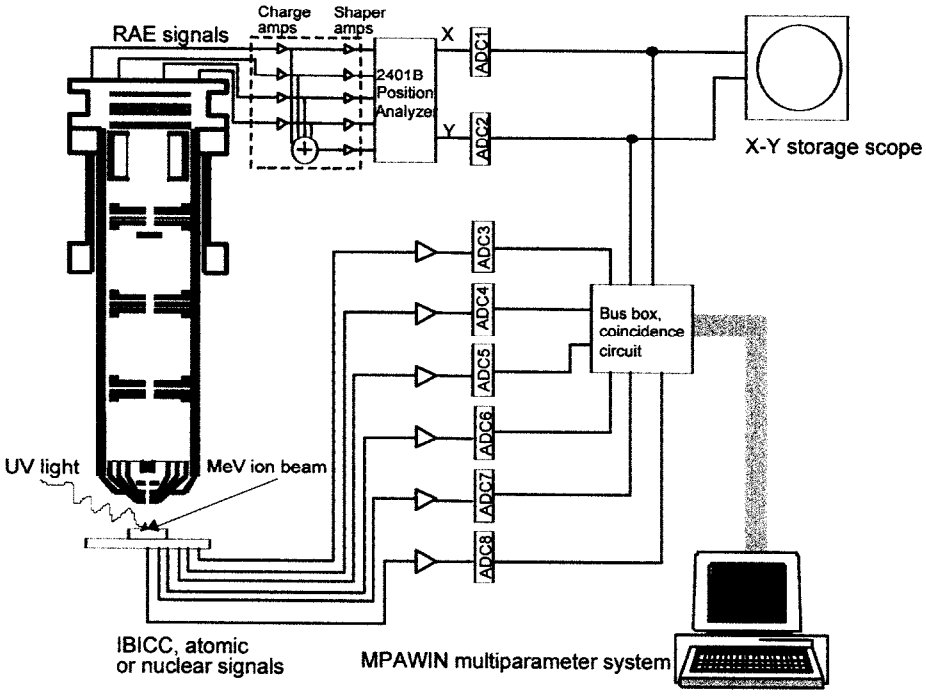

Figure 1. Schematic of the Ion Electron Emission Microscope system showing the target, PEEM and Position Sensitive Detector, the Position Analyzer and Multi-Parameter data acquisition system.

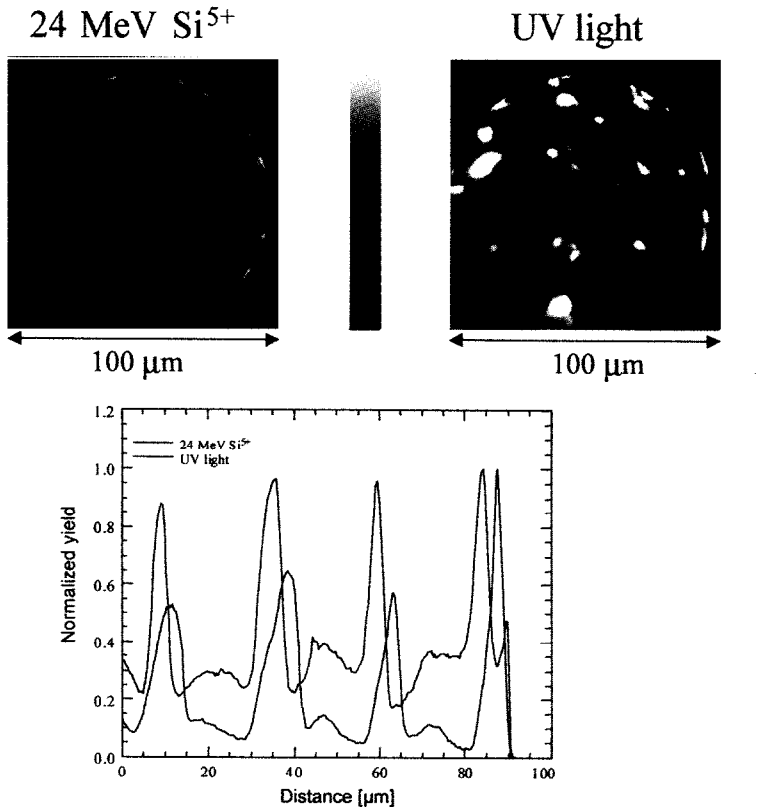

Figure 2. IEEM and PEEM secondary electron intensity images and line scans of a 1000 mesh Cu TEM grid. Line scans demonstrate the resolution of ~1.1 μm. Considerably less contrast is observed in the IEEM image, which is advantageous to the technique.

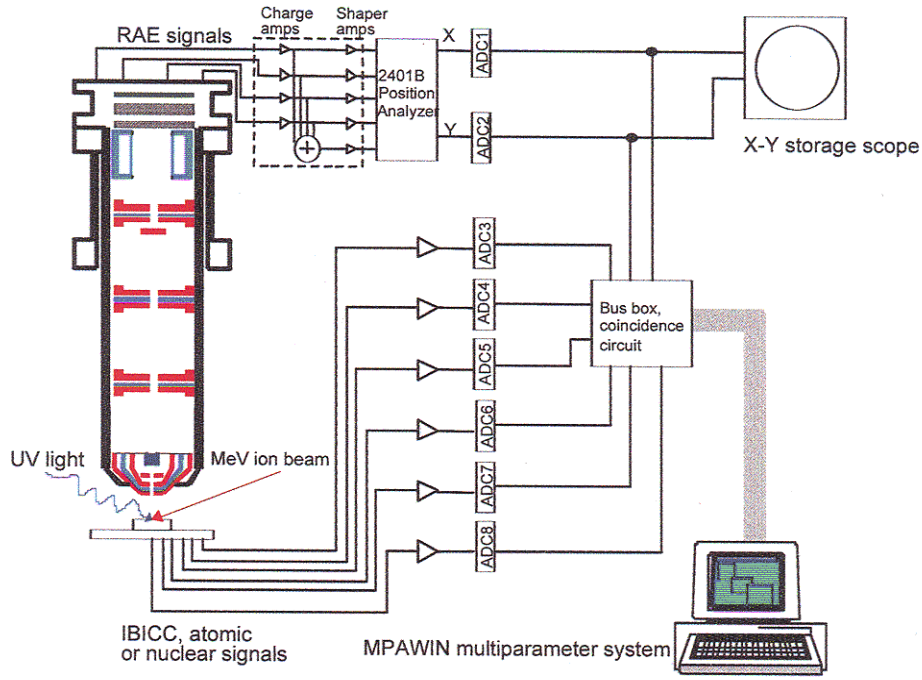

Figure 1. Schematic of the Ion Electron Emission Microscope system showing the target, PEEM and Position Sensitive Detector, the Position Analyzer and Multi-Parameter data acquisition system.

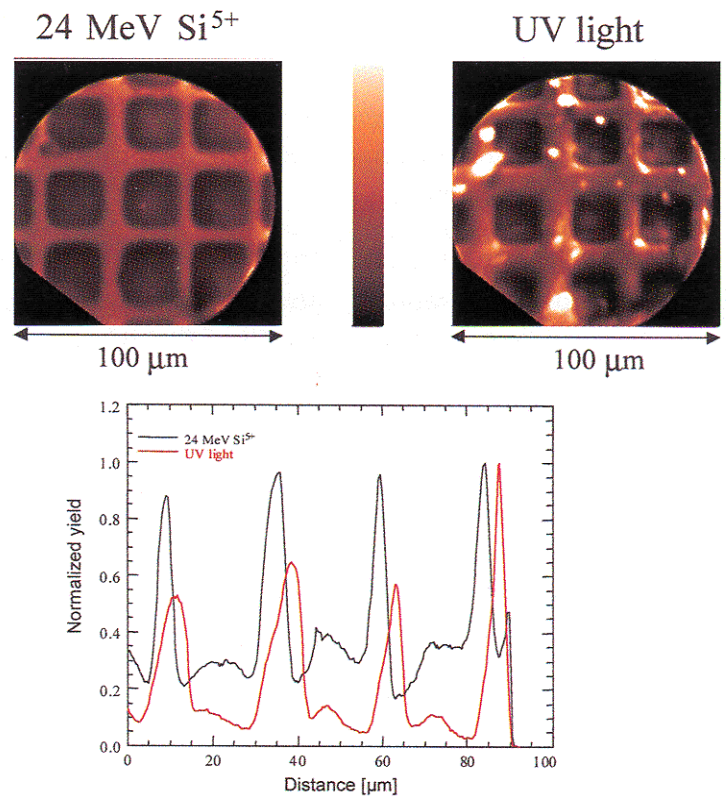

Figure 2. IEEM and PEEM secondary electron intensity images and line scans of a 1000 mesh Cu TEM grid. Line scans demonstrate the resolution of ~1.1 µm. Considerably less contrast is observed in the IEEM image, which is advantageous to the technique.

Using Heavy Ion Backscattering (HIBS) to Solve IC Manufacturing Problems

*J. C. Banks, B. L. Doyle,a nd J. A. Knapp**

Motivation--The control of metallic contamination on wafer surfaces is extremely important during semiconductor manufacturing. For instance, in starting materials, metallic contamination levels above $2.5x10^{10}$ atoms/cm2 are detrimental to devices used in 0.25 μm technology and can limit wafer yield. A new ion beam analysis technique has been developed and patented at Sandia that can accurately measure this ultra-trace level of metallic contamination on wafer surfaces. Using this technique, a Sandia/SEMATECH Heavy Ion Backscattering Spectrometry (HIBS) User Facility has been made available to U.S. industry, national laboratories, and universities for conducting contamination control studies.

Accomplishment--We have worked with Motorola using the HIBS facility to help solve problems in the calibration of Total Reflection X-ray Fluorescence (TXRF) instruments. TXRF instruments are used for detecting trace levels of transition metals introduced by semiconductor processing procedures and equipment. These instruments are typically calibrated using the manufacturer's data supplied with the instrument. This instrument-specific calibration has led to inaccuracies and a resulting lack of interchangeability in TXRF data. To illustrate the problem caused by independent calibration, the average error in measuring the same contamination standard wafers by different lab sites during a round robin conducted at Motorola is shown in Fig. 1. To solve the problem, HIBS was used to non-destructively verify the amount of contaminant on commercially obtained contamination standard wafers. The HIBS data was then used to create a universal sensitivity factor curve for recalibration of all the TXRF instruments used in the study. The success of this recalibration is also shown in Fig. 1.

We have worked with Texas Instruments using the HIBS facility to help solve problems in the development of cleaning processes for the removal of high-Z metallic contamination. To decrease the size of capacitors used in ULSI dynamic random access memories (DRAMs), Texas Instruments has been studying the use of a high-k dielectric, barium-strontium-titanate (or BST) between platinum electrodes (Pt/BST/Pt). Because of the concern about cross contamination of wafers and processing tools with these materials, several questions had to be answered, including how effective present cleaning methods were for removing these heavy metals. To begin answering this question, wafers were uniformly dosed with the contaminates and the areal density measured. The wafers were then subjected to various cleaning methods and measured again. The comparison in Fig. 2 shows the efficacy of a cleaning process for barium.

Significance--With Motorola we have produced a universal method for calibrating TXRF instruments that has led to improved quality control during IC manufacturing. The calibration method has international applicability, since the lack of interchangeability of data between TXRF instruments is a problem that has been reported world wide. With Texas Instruments we have successfully used HIBS technology to evaluate handling and processing of new materials which can be used in the manufacture of ULSI DRAMs.

*In collaboration with D. Werho and R. B. Gregory, Motorola; M. Anthony, T. Q. Hurd, Texas Instruments; and A. C. Diebold, SEMATECH

Sponsors for various phases of this work include: TPP, SEMATECH, CRADA, LDRD

Contact: James C. Banks, Radiation Solid Interactions and Processing Dept., 1111
Phone: (505) 844-8824, Fax: (505) 844-7775, E-mail: jcbanks@sandia.gov

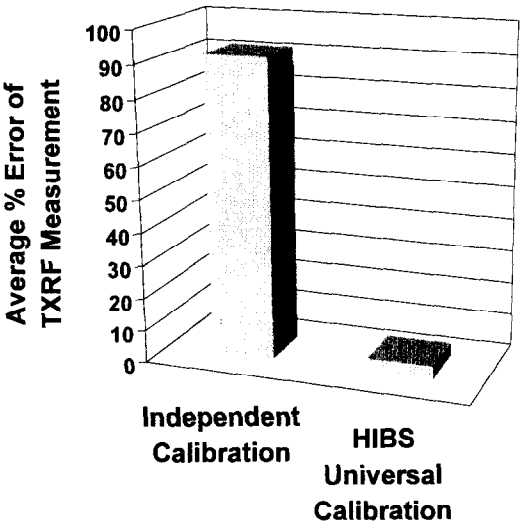

Figure 1. The average error between measurements made on the same contamination standard wafers by TXRF instruments at Motorola illustrate the problem of instrument-specific (independent) calibration. Further comparisons, after recalibration using HIBS data, show the success of universal calibration.

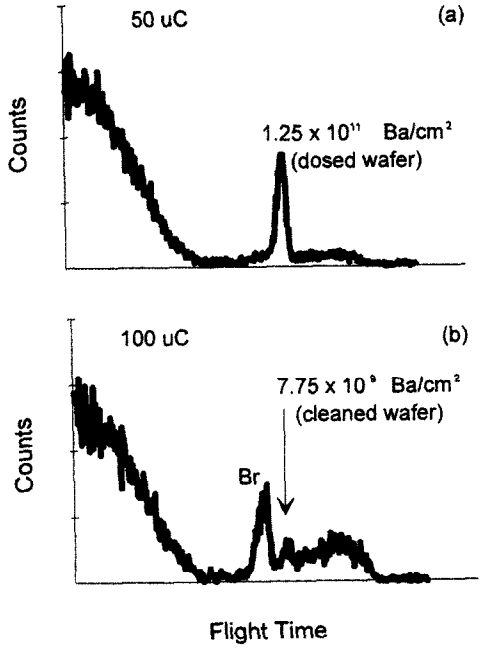

Figure 2. HIBS analysis before (a) and after (b) the clean shows that 0.49% HF is effective in removing trace levels of Ba contamination.

GaAs Surface Phase Diagram During MOCVD

J. R. Creighton and K. C. Baucom

Motivation--High quality thin films of III-V compound semiconductors are routinely synthesized using metalorganic chemical vapor deposition (MOCVD). The structure and stoichiometry of the III-V surfaces during deposition are of fundamental interest because the surface condition strongly affects the **crystallinity, morphology**, and **purity** of the deposited film. The surface condition, or phase, will also reflect the interactions of the reactor conditions with the complex chemistry of the deposition process. As the model compound semiconductor surface, GaAs(100) is considerably more complex than elemental semiconductor surfaces such as Si(100) and Ge(100). As a consequence, unraveling the structure of the GaAs(100) surface during growth has been difficult, particularly under the broad range of conditions associated with MOCVD.

Accomplishment--We have used a combination of UHV and near-atmospheric-pressure surface science techniques with *in-situ* spectroscopic measurements to map the surface phase diagram (see Fig. 1) of GaAs(100) during MOCVD from trimethylgallium and arsine, and, for the first time, to identify the structures of all observed phases. We have found that there are three "basic" types of surfaces: two arsenic terminated and one, unexpectedly, methyl terminated, although still arsenic rich.

The Type I and II phases are due to reconstructions terminated with more than one monolayer of arsenic, and are generally correlated with the growth of high quality GaAs. The Type III phase was found to be due to a newly discovered methyl-terminated arsenic-rich reconstruction (see Fig. 2). This phase correlates with the deposition of GaAs epilayers containing a high level of carbon doping. The Type I surface is the only phase that is also created during MBE, with the Type II and III phases being unique to the MOCVD environment.

Another interesting observation is that all surfaces appear to be laterally heterogeneous superpositions of the three basic surface types, with the degree of admixing varying with distance from our measured phase boundaries.

Significance--Epitaxially grown thin layers of GaAs and other III-V compound semiconductors are the foundation of advanced optoelectronic technology and they have enabled exciting scientific discoveries such as the quantum Hall effect. Knowledge of the GaAs(100) MOCVD surface phase diagram and understanding of various possible surface ***structures*** are crucial to controlling the growth of high quality epitaxial layers with the desired physical ***properties***. Armed with this knowledge of structure, it will now be possible to create an atomistic and molecular understanding of properties, both thermodynamic and kinetic, that characterize the growth and morphology of this important class of semiconductor materials. This has ramifications on many science and technology issues, including microscopic lateral compositional uniformity, microscopic vertical abruptness of heterointerfaces, and morphology evolution of patterned surfaces. The phase diagram also provides a mechanism for comparing results across different laboratories and different MOCVD reactors, a factor that is important for the continued advancement of the field.

Sponsors for various phases of this work include: BES, DP - Phys. Sci & Tech.
Contact: J. Randall Creighton, Chemical Processing Sciences Dept., 1126
Phone: (505) 844-3955, Fax: (505) 844-3211, E-mail: jrcreig@sandia.gov

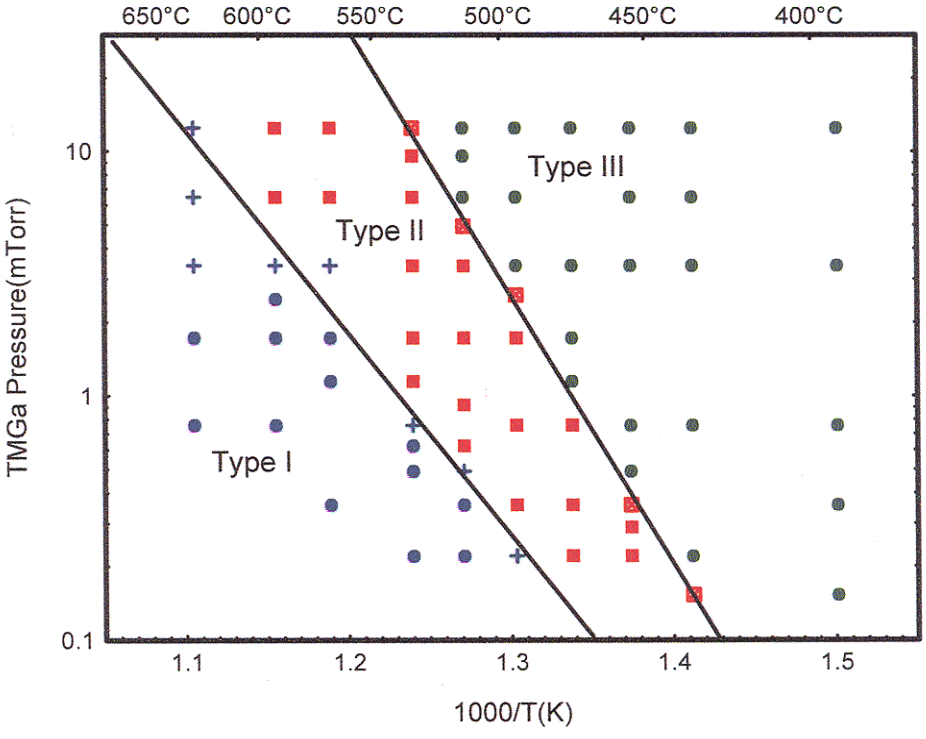

Figure 1. GaAs (100) MOCVD Phase Diagram, + symbols represent intermediate phases.

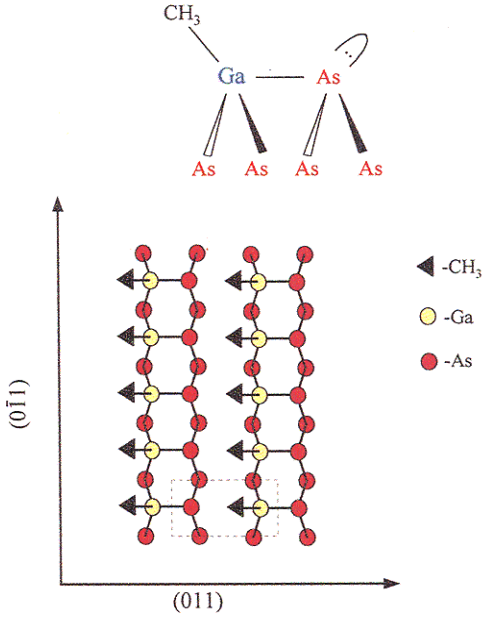

Figure 2. Structure of the Type III surface phase, a methyl-terminated (1x2) arsenic-rich reconstruction

Selective Area MOCVD Growth for Vertical Cavity Laser Arrays

M. E. Coltrin, H. Q. Hou, and K. D. Choquette

Motivation--Many III-V materials will not grow on top of oxide or nitride layers, allowing for selective area growth. In this technique, a patterned oxide or nitride (dielectric) mask is deposited on a pre-grown epitaxial layer. When the growth of InGaAs or AlGaAs, for example, is continued, it only occurs on the exposed epitaxial layer and not on the mask. There is a greater supply of the gas-phase reactants over the masked region, because there is no deposition there. This pool of excess reactants diffuses to the unmasked deposition areas, enhancing the local growth rates there. Reagents of differing mass, e.g., In vs. Ga, diffuse at different rates, resulting in thickness and composition variations across the growth zone, which can potentially be manipulated to tailor optoelectronic properties.

Accomplishment--Selective area growth by metalorganic chemical vapor deposition (MOCVD) has been used to make vertical-cavity surface-emitting laser (VCSEL) arrays with different emitting wavelengths. A 2-D, gas-phase reaction/diffusion model was developed to design and optimize growth conditions. The model predicts thickness and composition variations as a function of the dimensions of the masked and unmasked regions. Quantum wells approximately 80 Angstroms thick of $In_xGa_{1-x}As$ ($x \sim 0.1$) were grown, with $Al_xGa_{1-x}As$ ($x=0.1$) barrier layers. Figure 1 illustrates an array of different masking patterns in which the inner diameter of the unmasked region was kept constant, and the width of the masked region was varied. The growth-rate enhancement effect is greater as the masked region is increased. Four room-temperature cathodo-luminescence spectra are shown, which illustrate the shift to longer wavelength, due to increased In content, as the mask width is increased. Indium has a smaller diffusion coefficient (due to its greater mass) than gallium, which magnifies its growth-rate enhancement and thus its composition. Figure 2 shows a comparison of measured and calculated laser cavity wavelength (a metric of deposition thickness) and quantum-well gain wavelength (a metric of composition), showing good agreement between theory and experiment. Laser performance at 920-nm wavelength was comparable to standard, 1-step epitaxial processing. The emitting wavelength variation from a 2D VCSEL array was achieved as designed.

Significance--Vertical-cavity resonance opto-electronic devices, such as vertical-cavity surface-emitting lasers (VCSELs), resonance-cavity photodetectors (RCPDs), and Fabry-Perot cavity modulators (FPCMs), are very important for a wide range of applications in optical communications and sensing. A 1- or 2-dimensional (2D) device array emitting, detecting, or modulating light at different wavelengths enables many unique applications. For instance, a VCSEL array with different wavelengths can be used for wavelength-division multiplexing (WDM) fiber-optic communication systems. Different wavelengths from different array elements can be coupled into a single fiber for transmission over a distance. Each wavelength can be differently encoded and a de-multiplexing system in the receiving end can separate the different channels, greatly enhancing the transmission capacity.

Sponsors for various phases of this work include: BES, DP - Phys. Sci & Tech.
Contact: Michael E. Coltrin, Chemical Processing Sciences Dept., 1126
Phone: (505) 844-7843, Fax: (505) 844-3211, E-mail: mecoltr@sandia.gov

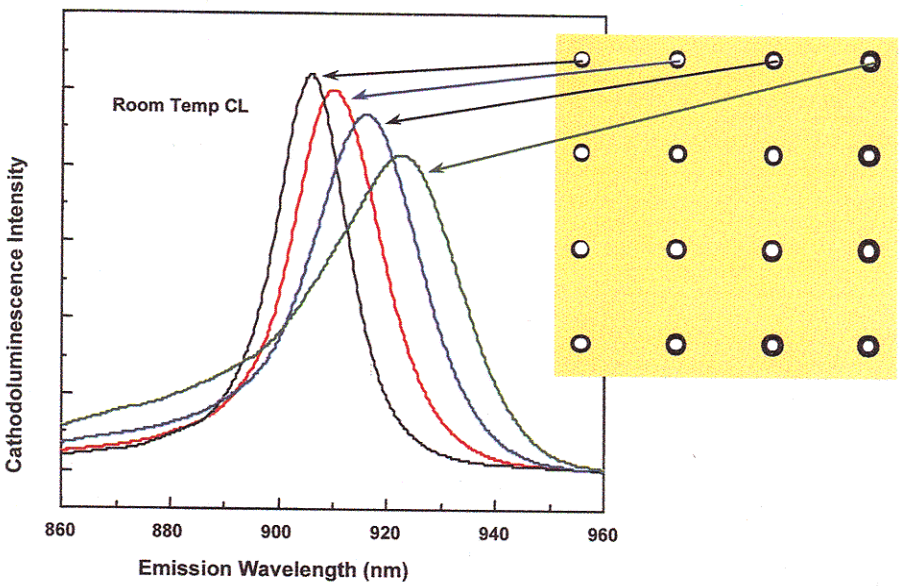

Figure 1. Cathodoluminescence measured from selective area growth in deposition zones of varying mask widths.

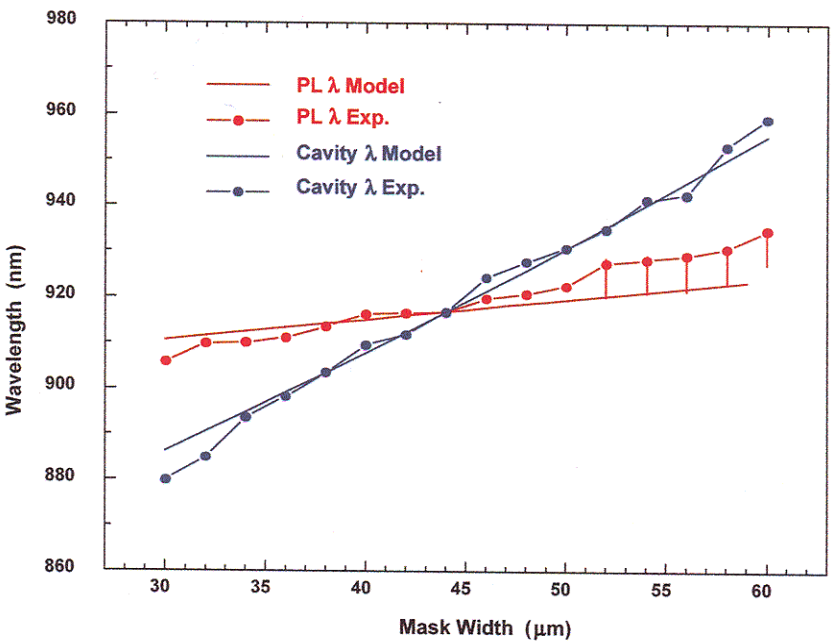

Figure 2. Comparison between experimental and calculated quantum-well wavelengths (a measure of composition) and cavity wavelengths (a measure of thickness).

Chemical Mechanisms for Modeling $BCl_3/Cl_2/Ar$ Plasmas

*P. Ho, E. Meeks, and R. J. Buss**

Motivation--Plasma processing has become increasingly important in the microelectronics industry and is routinely used for etching silicon, insulator, and metallization layers. Plasma processes offer the advantage over thermal processes of low wafer temperatures combined with high processing rates.

Computational modeling, especially when closely coordinated with experiment, is an increasingly important tool for improving equipment and process development. A detailed model of the chemistry and physics for a given processing plasma allows questions of scale-up and geometry changes to be investigated in a simulation rather than by cutting metal. However, this requires the development of a gas-phase chemistry mechanism (reaction paths plus rate parameters), a surface chemistry mechanism, and a set of transport-property data (if transport effects are included).

Accomplishment--We have developed a chemical reaction mechanism that describes $BCl_3/Cl_2/Ar$ plasmas used in the etching of metal lines in microelectronics fabrication processes. A reasonable set of reaction paths and rate coefficients has been derived to describe low-pressure reactors with high plasma density. The mechanism describes 59 gas-phase and 18 plasma-surface reactions. We used a well mixed reactor (0-D) model to develop the reaction set and to validate it with absolute experimental measurements of electron and Cl- densities, as well as relative measurements of BCl and Cl radicals by Hebner and coworkers in a research reactor.

Figure 1 illustrates the excellent agreement attained between model and experiment for the cases of electron densities and Cl- densities with varying Cl_2/Ar and BCl_3/Cl_2 gas mixtures. However, the diagnostic measurements cover a much wider range of operating conditions and gas mixtures than shown here, and the model agreed well with experiment over the entire set, capturing most of the observed trends. The model also reproduces relative ion ratios measured by Woodworth and coworkers, as well as Cl/Cl_2 density ratios measured by molecular beam mass spectrometry. A sensitivity analysis (Fig. 2) shows the relative importance of the various reactions to the model predictions of species densities that were measured in the experiments. We also compared results from the 0-D model and a 2-D continuum plasma model, using the same reaction mechanism, to further validate the chemistry set.

Significance--The kinetics of the competing chemical reactions that occur within a plasma affect almost every metric of the wafer process, including etch rate, uniformity, selectivity, and profile evolution. The chemistry occurring in a plasma reactor also controls reactor emissions, and thus the need for abatement of the exhaust streams, gas-utilization requirements, and the frequency and method of reactor cleaning. These latter effects directly affect the costs of reactor usage. This demonstration that we can realistically model the reactions in a complex, technologically important system, should accelerate the use of modeling for equipment design and process development.

*In collaboration with G. A. Hebner, P. A. Miller, J. R. Woodworth (1128), C. B. Fleddermann (UNM), S. J. Choi (9114), A. Ting, J. W. Shon (8345), Applied Materials
Sponsors for various phases of this work include: SEMATECH CRADA, TPP, BES
Contact: Pauline Ho, Chemical Processing Sciences Dept., 1126
Phone: (505) 844-3759, Fax: (505) 844-3211, E-mail: pho@sandia.gov

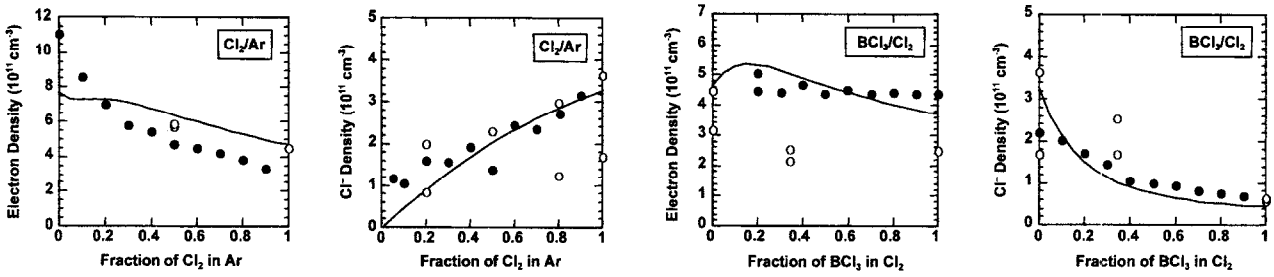

Figure 1. Example of comparisons between model predictions (curves) and data of Hebner, et al. (points) for the inductively coupled GEC-ICP reference cell, 300W input power, 20 mTorr pressure.

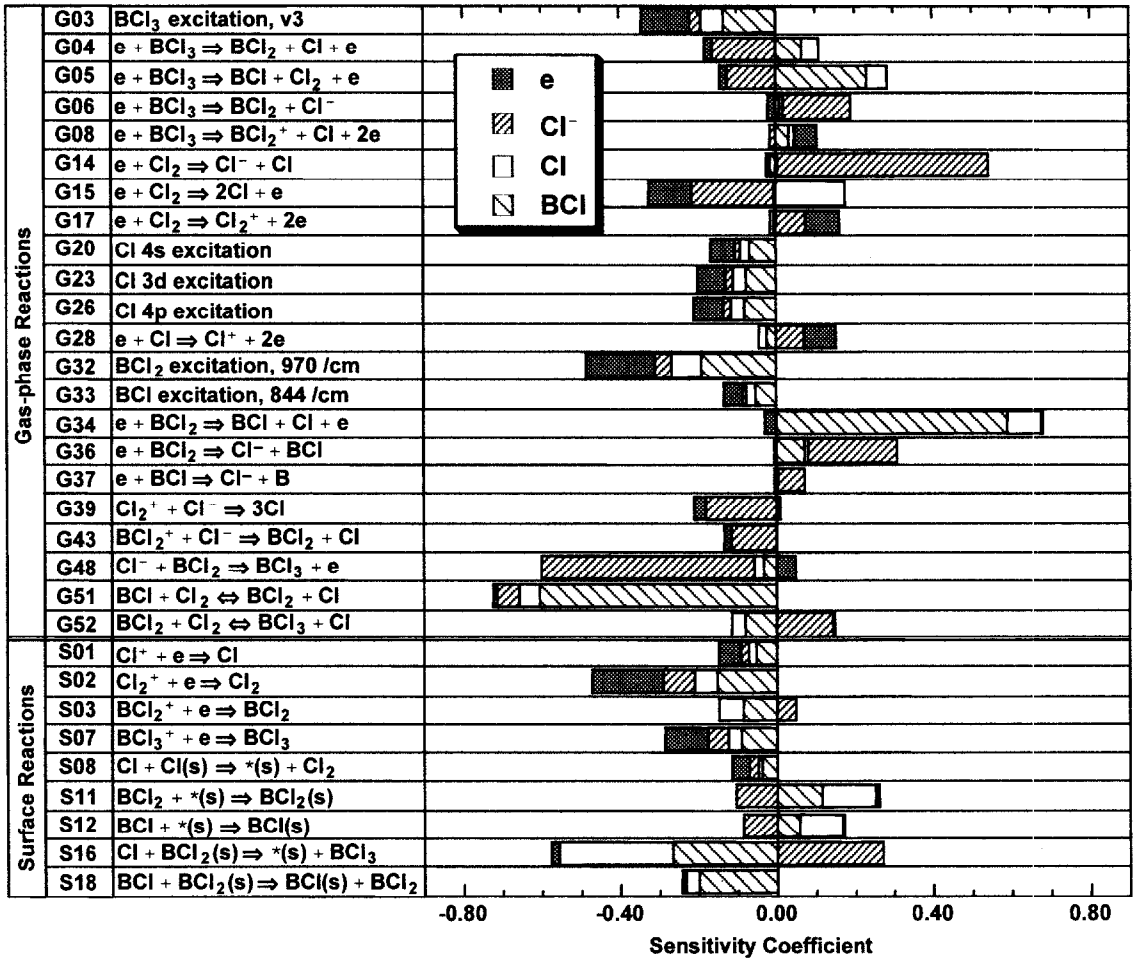

Figure 2. Sensitivity coefficients show which reactions in the model are important for the comparisons with experimental data. In the reaction numbers, 'G' specifies a gas-phase reaction and 'S' specifies a surface reaction.

Development of Advanced Diagnostics in support of Microelectronic Processing

*B. P. Aragon, T. A. Hamilton, G. A. Hebner, M. E. Riley, and J. R. Woodworth**

Motivation--Plasma discharges are currently used to etch sub-micron patterns in integrated circuits for both defense and commercial electronics. The rapid rate of improvement in these devices is dependent on the ability to develop new techniques to etch ever-smaller patterns in these circuits. We are developing a variety of diagnostics to provide the detailed experimental measurements needed to understand both how to etch smaller patterns in the microchips and how to avoid damaging the thin insulating layers in the circuits as the patterns are being etched. In this research brief, we describe two of these diagnostics, which measure electric fields in the discharge and absolute fluxes of hard ultraviolet photons near the wafer surface.

Accomplishment--Details of the anisotropic etching process are critically dependent on ion trajectories near the wafer. These ion trajectories are controlled by the electric fields near the wafer. In collaboration with U. Czarnetzki and H. F. Döbele at the Universität GH Essen, Germany, we have determined spatially-resolved electric fields in a plasma close to a patterned surface. This was accomplished by measuring the electric-field-induced splitting of the hydrogen Rydberg levels using a novel two-color, laser induced fluorescence technique (Fig. 1). For these discharge conditions, the electric field modulation extends approximately 4 mm away from the surface, independent of the surface condition, before becoming approximately uniform. The rounded contours of the electric fields indicate that there are significant transverse E-fields which will perturb the trajectories of the ions as they approach the grooves. Electric field strengths were also calculated using a 2D Poisson solver developed at Sandia. In general, the model predictions shown in Fig. 1 capture the major structure of the measured electric field.

Microelectronic devices contain thin insulating layers of silicon dioxide which may be stressed close to their breakdown limits during normal operation. Hence, any process which damages the silicon dioxide thereby lowering its breakdown strength, can have serious consequences. Vacuum ultraviolet photons having energies greater than 8.8 eV (or wavelengths shorter than 140 nm) can damage silicon dioxide. We have made the first measurements in a commercial metal-etch plasma reactor of the absolute intensities of vacuum ultraviolet photons striking a microelectronic wafer during the etching process. We find that the photon flux to the wafer from our Cl_2/BCl_3 discharges is about 7×10^{13} photons/cm^2/sec and that many of the photons will penetrate deeply into the SiO_2. This work must now be included in model studies to understand the impact on integrated circuit reliability.

Significance--This work improves our fundamental understanding of electric fields in discharges and allows discharge numerical models to be tested at a much more rigorous level of detail. This work also gives important information to researchers attempting to minimize device damage in new generations of microelectronics.

*In collaboration with SEMATECH, Applied Materials Corp., Univ. of Essen, Germany
Sponsors for various phases of this work include: DP - Phys. Sci. & Tech.
Contact: Joseph R. Woodworth, Laser, Optics, and Remote-Sensing Dept., 1128
Phone: (505) 844-1243, Fax: (505) 844-5459, E-mail: jrwoodw@sandia.gov

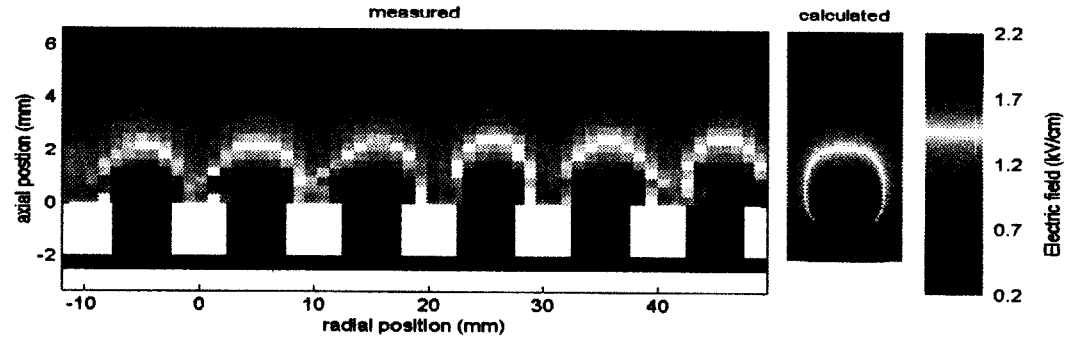

Figure 1. Magnitude of the electric field strength above an aluminum grooved electrode. The black represents the grooved electrode. Discharge conditions were 50 Pa of hydrogen, 80 W rf power, -330 V_{dc} bias and 720 V_{p-p} rf voltage. For the calculated field, the potential drop was 750 V, and the volumetric charge density above the surface was 1.2 x 10^9 cm^{-3} or 1.95 x 10^{-4} C/m^3.

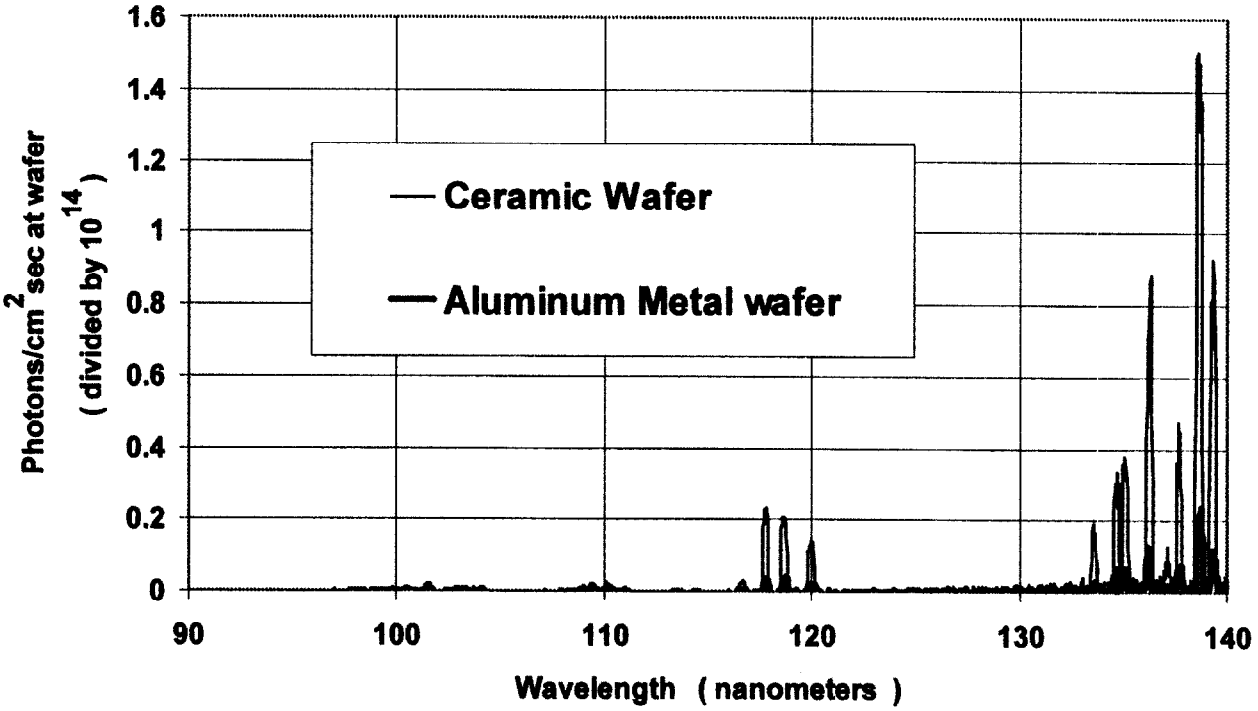

Figure 2. Absolute photon fluxes at the center of a 15-cm wafer in a Cl_2/BCl_3 plasma processing discharge as a function of wavelength. Data is shown for cases with an aluminum oxide ceramic wafer and an aluminum metal wafer. The emission features between 110 and 140 nm are due to transitions in neutral atomic chlorine. All the emission features at wavelengths shorter than 140 nm can damage SiO_2. Most studies assume that VUV light is absorbed in a thin surface layer of the SiO_2. However, the emission features seen between 130 and 140 nm will penetrate deeply into SiO_2.

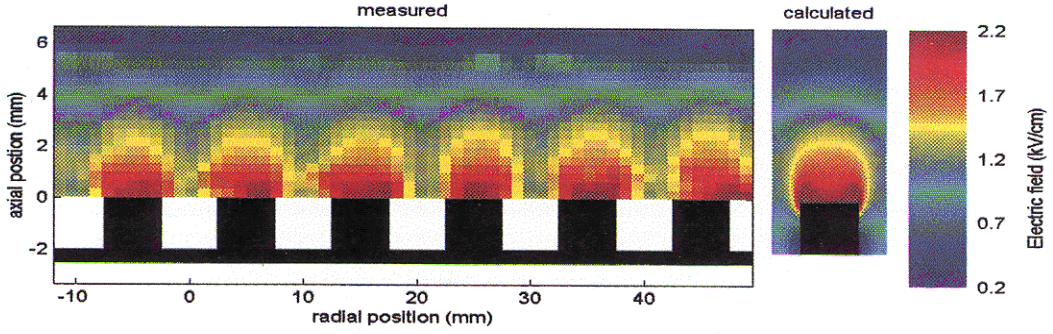

Figure 1. Magnitude of the electric field strength above an aluminum grooved electrode. The black represents the grooved electrode. Discharge conditions were 50 Pa of hydrogen, 80 W rf power, -330 V_{dc} bias and 720 V_{p-p} rf voltage. For the calculated field, the potential drop was 750 V, and the volumetric charge density above the surface was 1.2 x 10^{9} cm^{-3} or 1.95 x 10^{-4} C/m^{3}.

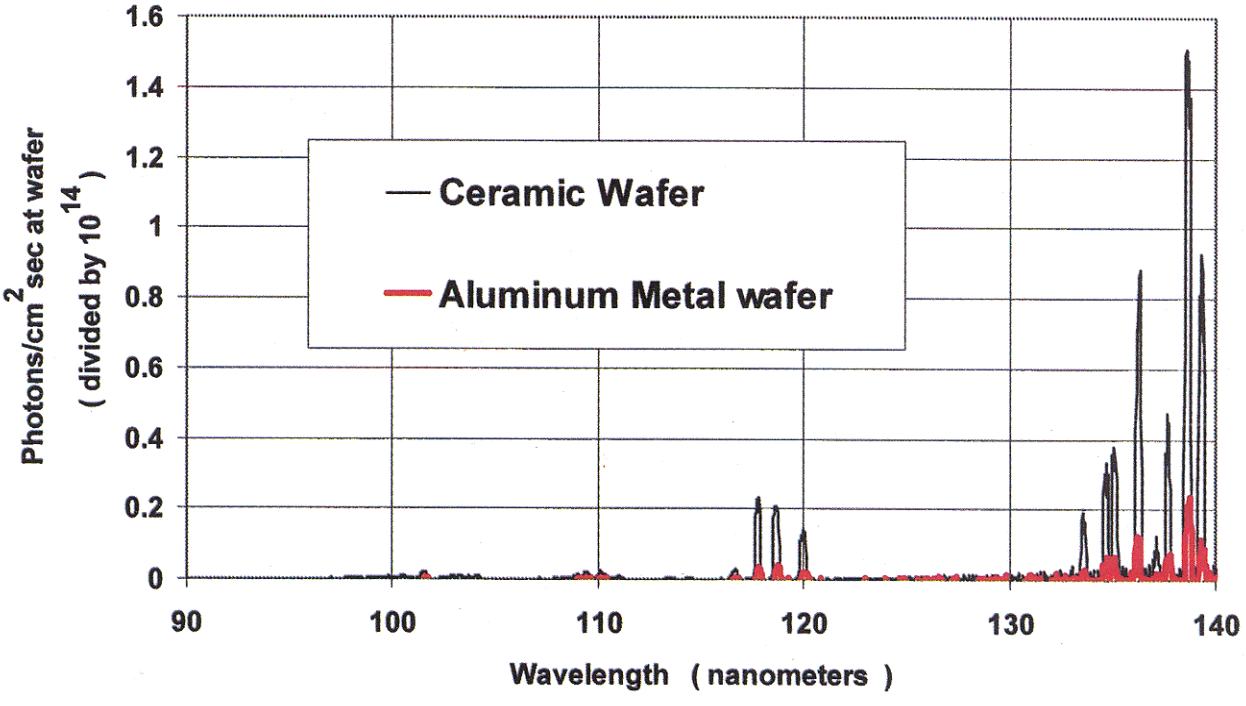

Figure 2. Absolute photon fluxes at the center of a 15-cm wafer in a Cl_2/BCl_3 plasma processing discharge as a function of wavelength. Data is shown for cases with an aluminum oxide ceramic wafer and an aluminum metal wafer. The emission features between 110 and 140 nm are due to transitions in neutral atomic chlorine. All the emission features at wavelengths shorter than 140 nm can damage SiO_2. Most studies assume that VUV light is absorbed in a thin surface layer of the SiO_2. However, the emission features seen between 130 and 140 nm will penetrate deeply into SiO_2.

The Ontogeny of Plasma from a Pulsed Vacuum Arc

B. P. Aragon, T. A. Hamilton, G. A. Hebner, P. A. Miller, and J. R. Woodworth

Motivation--Pulsed electrical discharges between electrodes in vacuum give rise to transient "vacuum-arc" plasmas containing high densities of many different materials emanating from the walls of the vacuum envelope as well as from the electrodes. The behavior of these arcs is complex because they involve dynamical phenomena at densities spanning the range from solid density to high vacuum. Such arcs have been studied for decades and, in one particular application, they have served as the ion source for some neutron tubes. Now they are being studied in greater detail both experimentally and theoretically as part of Sandia's stockpile-stewardship effort. We are applying to these studies many diagnostic techniques and computational tools that were not available to previous workers in an attempt to understand quantitatively the entire life cycle of the arc, from initiation to extinction, based largely on first-principles-based models.

Accomplishment--We have developed a laboratory diagnostic testbed and a suite of diagnostics and we are applying them to studies of pulsed vacuum arcs. Some of the diagnostics are replications of techniques used in previous work, which allows us to compare directly to earlier experiments. Descriptions of two newer diagnostic techniques follow.

Laser deflection measurements, related to schlieren and interferometric techniques, allow measurement of plasma density gradients. A focused, low-power laser beam is passed through the plasma plume and the time-dependent position of the transmitted beam is recorded. The beam is deflected because the plasma acts as a lens. The plasma refractivity is dominated by the contribution from electrons for our conditions. Using a stabilized, low-noise, helium-neon laser and a four-element silicon detector, we obtained deflection-detection thresholds near 30 nanoradians. Typically, the plasma deflects the laser beam by 1 microradian when it passes within 0.3 mm of an electrode. Figure 1 shows the technique and a false-color image of the beam deflection transverse to the axis of the plume. This measurement technique complements Langmuir probes that are used to measure ion current many millimeters from the arc electrodes.

In some experiments, the electrodes consist of scandium loaded with deuterium. In these cases, scandium can be an undesired impurity in the plasma. To quantify the impurity level, a cw frequency-doubled diode laser system was developed to detect scandium atoms by measuring absorption from the ground state at 402 nm. The technique is very sensitive and can detect scandium atom densities near $10^{12}/cm^3$ over path lengths of 1 mm. Furthermore, because the laser line width is less than the Doppler width of the absorbing transition, the technique can measure the velocity distribution function of the scandium atoms. Figure 2 shows the absorption fraction at one time in the plasma pulse as a function of the laser frequency. In this case, the asymmetric line shape indicates that the scandium atoms had a net drift velocity away from the laser.

Significance--Experimental measurements of plasma properties as functions of space and time improve our fundamental understanding of arc physics and provide validation data required for testing and for developing confidence in ASCI neutron-tube models that support stockpile stewardship.

Sponsors for various phases of this work include: DP - ASCI, DP - MAVEN, DP - Phys. Sci. & Tech.
Contact: Paul A. Miller, Laser, Optics, and Remote-Sensing Dept., 1128
Phone: (505) 844-8879, Fax: (505) 844-5459, E-mail: pamille@sandia.gov

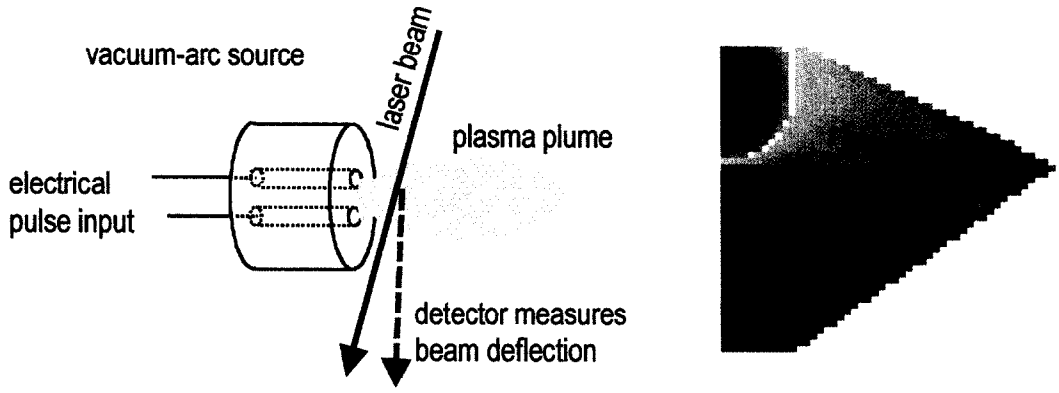

Figure 1. Schematic of experiment and false-color representation of laser-deflection data showing beam deflection transverse to the expansion direction of the plasma plume. The image is a spatial map of deflection at one instant in time, generated from measurements at 18 different spatial positions on 18 different pulses. The deflection is nominally symmetric about the plume axis, as expected. The data will be compared to predictions based on post-processed output from simulations of the plasma plume.

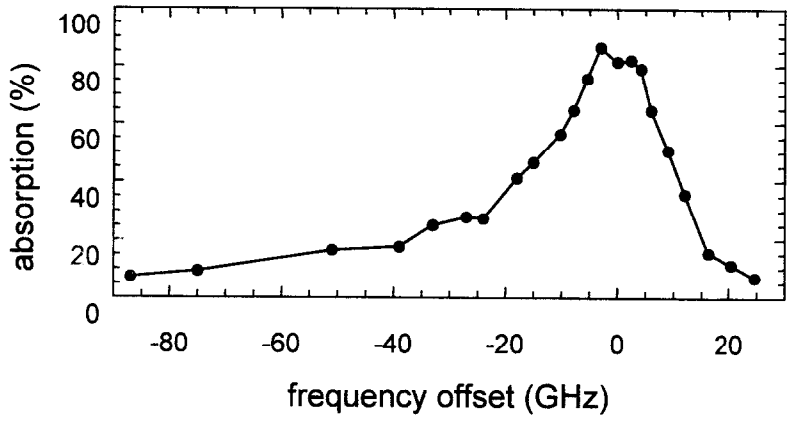

Figure 2. Frequency dependence of line-integrated optical absorption by scandium atoms at 402 nm. These data represent the absorption at one spatial position and at one time in the plasma pulse, as measured with the cw laser tuned to different frequencies on 22 different pulses. The asymmetric line shape shows that the scandium atoms, on average, had a net drift velocity away from the laser. Note that the absolute absorption is high, approaching 100%.

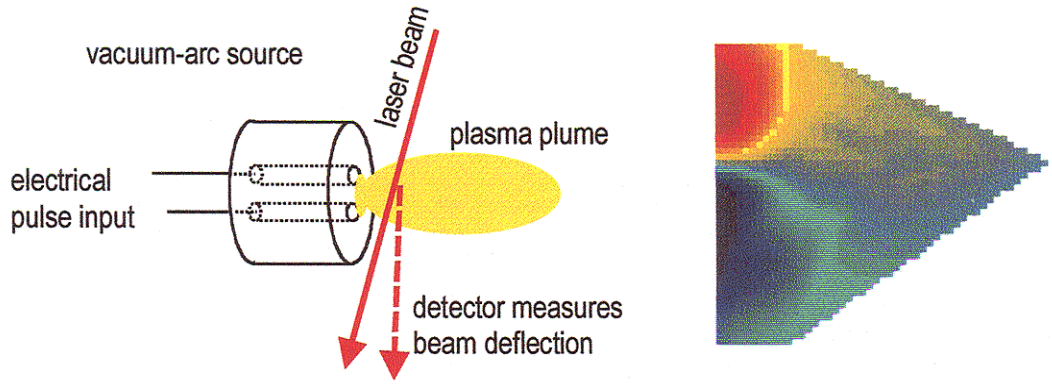

Figure 1. Schematic of experiment and false-color representation of laser-deflection data showing beam deflection transverse to the expansion direction of the plasma plume. The image is a spatial map of deflection at one instant in time, generated from measurements at 18 different spatial positions on 18 different pulses. The deflection is nominally symmetric about the plume axis, as expected. The data will be compared to predictions based on post-processed output from simulations of the plasma plume.

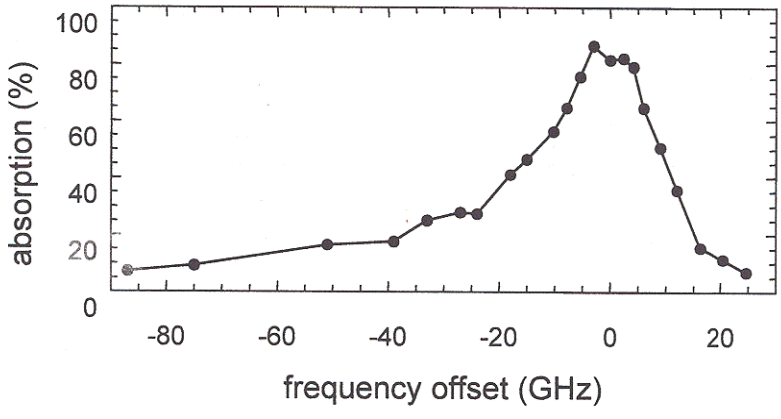

Figure 2. Frequency dependence of line-integrated optical absorption by scandium atoms at 402 nm. These data represent the absorption at one spatial position and at one time in the plasma pulse, as measured with the cw laser tuned to different frequencies on 22 different pulses. The asymmetric line shape shows that the scandium atoms, on average, had a net drift velocity away from the laser. Note that the absolute absorption is high, approaching 100%.

Recent Awards and Prizes

Recent Awards and Prizes

National and International Awards

1997 — Peter Mark Award for "Pioneering studies of atomic-scale, kinetic and thermodynamic aspects of the morphology of Si Surfaces, and significant innovations in scanning tunneling microscopy that make such measurements possible" - American Vacuum Society (B. S. Swartzentruber)
— Edward Orton, Jr., Memorial Lecturer Award - American Ceramics Society (T. A. Michalske)
1996 — DOE Young Independent Scientist Award (B. S. Swartzentruber)
— The Medard W. Welch Award for "His insightful predictions and explanations of surface phenomena based on first principles calculations" - American Vacuum Society (P. J. Feibelman)
1993 — International New Materials Prize for "Originating the Field of Strained-Layer Superlattice Electronics and Optoelectronics" - American Physical Society (G. C. Osbourn)
— Shock Compression Science Award - The American Physical Society (R. A. Graham)
1990 — E. O. Lawrence Award, Materials Science - DOE (S. T. Picraux)
1989 — Davisson-Germer Prize "For his pioneering work in developing the theory of electromagnetic fields at surfaces" - American Physical Society (P. J. Feibelman)
— Weyl International Glass Science Award - International Glass Commission (T. A. Michalske)

DOE Basic Energy Sciences, Material Science Awards

1998 — Sustained Outstanding Research in Condensed Matter Physics "Quantitative Measurements and New Mechanisms of Atom and Cluster Diffusion on Surfaces" (G. L. Kellogg)
— Significant Implications for DOE Related Technologies in Condensed Matter Physics "Semiconductor Materials Science Enables a Biological Microcavity Laser for Early Detection of Disease"(P. L. Gourley, M. H. Crawford, W. Chow, M. Sinclair and A. E. McDonald)
1996 — Outstanding Scientific Accomplishment--Solid State Physics "Development of Atom-Tracking Scanning Tunneling Microscopy for Direct Measurements of Surface Dynamics" (B. W. Swartzentruber)
— Significant Implication for Department of Energy Related Technologies--Materials Chemistry "Nanoclusters for Energy Applications" (J. P. Wilcoxon, P. P. Newcomer, D. E. Bliss,G. A. Samara, and A. Martino)
1994 — Sustained Outstanding Research--Solid State Physics "Surface Atom Energetics" (P. J. Feibelman)
— Sustained Outstanding Research--Metallurgy and Ceramics "Science of Surface Processes in Beam-Enhanced Growth" (E. Chason, J. Y. Tsao, J. A. Floro, K. M. Horn, T. M. Mayer, P. Bedrossian, D. K. Brice, A. J. Howard, S. T. Picraux, D. L. Buller, and K. J. Penn)

— Significant Implication for Department of Energy Related Technologies--Materials Chemistry "Real Time, In Situ Materials Growth Monitors Using Remote Optical Probes" (K. P. Killeen, S. A. Chalmers, W. G. Breiland, and T. M. Kerley)

1993 — Sustained Outstanding Research--Metallurgy and Ceramics "Strained Layer Superlattices and Artificially Structured Semiconductors" (P. Gourley, I. Fritz, E. Jones, K. Lyo, J. Nelson, R. Schneider, G. Osbourn, B. Biefeld, and R. Dawson)

— Significant Implication for Department of Energy Related Technologies--Metallurgy and Ceramics "Interfacial Force Microscope" (J. Houston and T. Michalske)

1992 — Sustained Outstanding Research--Materials Chemistry "CVD Sciences" (W. G. Brieland, M. E. Coltrin G. H. Evans, P. Ho, and R. Kee)

1991 — Sustained Outstanding Research--Metallurgy and Ceramics "Advanced Ion Beam Techniques for Materials Analysis" (B. L. Doyle, S. T. Picraux, J. A. Knapp, and S. M. Myers)

— Outstanding Scientific Accomplishment--Solid State Physics "Surface Diffusion by Atomic Substitution" (G. L. Kellogg and P. J. Feibelman)

— Significant Implication for Department of Energy Related Technologies--Metallurgy and Ceramics "Exceptionally High-Strength Aluminum Alloys" (D. M. Follstaedt, R. J. Bourcier, M. T. Dugger, and S. M. Myers)

1990 — Sustained Outstanding Research--Metallurgy and Ceramics "Model of Hydrogen-Defect Interactions in SiO2 and at the SiO2-Si Interface" (K. L. Brower, S. M. Myers, P. M. Richards, and H. J. Stein)

1989 — Significant Implication for Department of Energy Related Technologies--Solid State Physics "Development of Tl-Ca-Ba-Cu-O High Temperature Superconducting Thin Films and Demonstration of Novel High-Performance Devices" (R. J. Baughman, D. S. Ginley, J. F. Kwak, B. Morosin, and E. L. Venturini)

Other Awards

1998 — Technology of the Year Award, Industry Week Magazine for the Double Electron Layer Tunneling Transistor (J. A. Simmons)

— NM Software Author of the Year Finalist (M. E. Coltrin)

1997 — R&D Award for "Development of a Biological Microcavity Laser" (P. L. Gourley)

— R&D Award for "Bringing to the market one of the top 100 technologically significant new products of 1997" (W. G. Breiland)

1995 — Norbert J. Kreidl Award from the New Mexico Ceramics Society Glass Division (K. S. Simmons-Potter)

1994 — R&D 100 Award for "Interfacial Force Microscope" (J. E. Houston and T. A. Michalske)

1993/1994 — J. J. Thomson Award for "Temporal and Spectral Gain Dynamics in an Actively Modelocked Semiconductor Laser" (W. W. Chow)

Resources and Capabilities

Resources and Capabilities
Physical and Chemical Sciences Center

-- Diagnostics and Characterization --

Atomic-Level Imaging and Spectroscopy

We have developed technical capabilities in:

- Scanning Tunneling Microscopy (STM) in terms of ability to track single atoms;
- Low Energy Electron Microscopy (LEEM) in terms of spatial resolution and spectroscopic imaging capability;
- Field Ion Microscopy (FIM) in terms of single atom resolution and accurate temperature control 1 Kelvin;
- Atom Probe Microscopy (APM) in terms of pulsed laser desorption capability; and
- Interfacial Force Microscopy (IFM) with feedback for accurate force profile measurements.

Ion Accelerator Nuclear Microprobe

We have facilities for nuclear microscopy and radiation effects microscopy based on a 6 MV tandem Van de Graaff ion accelerator. We generate ion species from hydrogen to bismuth for both radiation effects research and quantitative high-energy ion beam analysis of materials containing light elements (hydrogen to fluorine) using heavy ion elastic recoil detection (ERD) and heavy elements using high-energy backscattering spectrometry, and Heavy Ion Backscattering (HIBS) (Includes Patent 3 5059785 issued October, 1991). An external Micro Ion Beam Analysis (X-MIBA) capability enables multi-elemental analysis and ion irradiation of samples which are vacuum incompatible or extraordinarily large. The Sandia Nuclear Microprobe with micrometer size high energy ion beams is used to study materials and devices. Special emphasis is given to the evaluation of the radiation hardness of microelectronic devices using three new advanced diagnostic techniques invented at Sandia: Single-Event-Upset Imaging, Ion-Beam-Induced-Charge-Collection Imaging (IBICC), and time-resolved IBICC.

Materials Microcharacterization

Our capabilities in this area include optical microscopy, scanning, electron microscopy, analytical transmission electron microscopy, double crystal x-ray diffraction, ion beam analysis of materials (RBS, channeling, ERD, PIXE, NRA), Hall measurements, microcaloremetry, photoluminescence, light scattering, electronic transport, deep level spectroscopy, magnetization, and dielectric and magnetic susceptiblities.

Surface and Interface Spectroscopies

We maintain strong capabilities in Auger electron spectroscopy (AES), x-ray photoelectron spectroscopy (XPS), low energy electron diffraction (LEED), ultraviolet photoelectron spectroscopy (UPS), thermal desorption spectroscopy (TDS), infrared reflectance-absorption spectroscopy (IRAS), and quantum state resolved laser surface probes.

Vision-Science Laboratory

The vision science laboratory consists of state-of-the-art hardware and software capabilities for carrying out video inspection, multi-spectral image analysis, and sensor-based pattern recognition. (Includes Imaging Processing System, Patent # 5495536.) These capabilities are used in applications ranging from microsensor-based chemical detection and recognition to automated video/SEM inspection of semiconductor materials and circuits. (Patent applied for December, 1996 for "a new cluster analysis method"). This is a new approach to pattern recognition, coupling perception-oriented research with machine algorithms.

Chemical Vapor Deposition (CVD)

Our experimental tools for investigating CVD include optical probes (such as reflectance-difference spectroscopy) for gas-phase and surface processes, a range of surface analytic techniques, molecular beam methods for gas/surface kinetics, and flow visualization techniques. These tools are integrated in a unique manner with research CVD reactors and with advanced chemistry and fluid models.

Growth Science Laboratory

Capabilities for in situ characterization of materials during thin film deposition, molecular beam epitaxial growth, and low energy ion beam simulated growth, include intensity profile sensitive reflection high energy electron diffraction (RHEED) for surface structure, energy dispersive x-ray reflectrometry for in situ surface and interface structure, multibeam wafer curvature for strain (Patent filed 1997), and Auger electron spectroscopy for surface composition.

KMAP X-ray Diffractometer

Based on double crystal x-ray diffractometry in combination with position sensitive x-ray detection, our KMAP x-ray diffraction analysis is used to determine the lattice constant, strain relaxation, composition, layer orientation, and mosaic spread for a large variety of advanced epitaxial semiconductor material systems.

Nanoelectronics Laboratory

We have the capabilities for fabrication of nanoscale quantum device structures together with capabilities for ultra-low-noise measurement of transport from 0.3 Kelvin to ambient at high magnetic fields.

Lasers and Optics

We provide characterization and advanced understanding in the area of solid-state lasers and non-linear optics, especially as coherent sources of broadly tunable light in rugged, compact geometries. We also have established expertise in long-term and transient radiation effects characterization of optical materials. (Includes patented Wavefront Sensor Patent 3 5493391, and Monolithic Optical Amplification Devices Patent # 5463649). Capabilities include the combined modeling and laboratory validation of the performance of non-linear optical materials as well as their radiation response characterization (pulsed nuclear reactor, and X-ray generators).

Laser and Optical Spectroscopies

Our capabilities in characterizing semiconductor materials by photoluminescence and magnetoluminescence extend down to low temperatures by optical laser imaging and laser microscopy, by laser excitation spectroscopy, and by the time-resolved measurements of optical emission. We also have developed a high lateral resolution, near-field scanning optical microscopy (NSOM) capability with time and frequency resolution. (Patent filed June, 1994 for Chemical Recognition Software.)

Low-Temperature Plasma Analysis

We have state-of-the-art capabilities for the analysis of low-temperature plasmas as found in commercial processing reactors. These include emission spectroscopy, electrical characterization, laser and microwave-based measurements of species concentrations, in situ electric field measurements, and others. Sandia is the only lab which combines new diagnostics, relevant process chemistries (complex mixtures), and massively parallel (MP) computer models for simulation of continuous and transient plasmas.

-- Synthesis and Processing --

Nanocluster Laboratory
We have developed and patented a process based on the use of inverse micelles for the synthesis of large quantities of monodisperse clusters of metals, semiconductors, and oxides.

Electron Cyclotron Resonance (ECR)
This plasma facility has been built for studying fundamental processes governing the growth of oxide and nitride dielectric films used in optoelectronics and used as hard coatings. This is the only system in the U.S. which combines ECR plus e-beam evaproation.

Molecular Beam Epitaxy (MBE)
We have research semiconductor growth laboratories for ultra-pure and ultra-flexible MBE growth of III-V materials. In addition, we have research systems for Group IV semiconductor growth.

Metal-Organic Chemical Vapor Deposition (MOCVD)
We maintain research facilities with capabilities in MOCVD of compound semiconductor materials. These capabilities include research reactors designed specifically for studies of CVD chemistry, fluid dynamics, the development of advanced in situ diagnostics, and the development of advanced semiconductor heterostructures.

Crystal and Thin Film Growth
Capabilities in this area include a pulsed laser deposition chambers, a high vacuum metal deposition chamber, a thin film oxide deposition chamber, a diamond-like carbon deposition chamber, a hot filament chemical vapor deposition chamber, and various apparati for single crystal growth. Our capabilities for stress relief of diamond-like carbon films and structures produced by pulsed laser deposition are not available elsewhere.

400 kV and 180 keV Ion Implanters
These systems are equipped with a variety of sources (gas, sputter, and metal vapor). This facility provides ion species from hydrogen to bismuth which can be used for studying fundamental irradiation mechanisms and selective chemical doping in semiconductors, metals, ferroelectrics, and superconductors.

High Pressure and Shock Wave Physics and Chemistry Laboratories
Our capabilities in this area include large volume static high pressure apparatus which can be operated at temperatures ranging from 2° to 700° K and in magnetic fields, as well as gas gun and explosive loading facilities with state-of-the-art, time-resolved diagnostics. Recovery fixtures have been developed for use with the gas gun and explosive shock loading facilities which allow unique Material synthesis over broad ranges of shock pressures and temperatures.

-- Theory and Simulation --

Electronic Structure and Linear Scaling

We have developed state-of-the-art massively parallel electronic structure algorithims, based on ab initio pseudopotentials and plane-wave/Gaussian basis functions. These codes are used to develop a fundamental understanding of physical phenomena and materials, including compound semiconductor band structure, diffusion of point defects, dopants and impurities, optoelectronic properties of extended defects, adsorbate interactions on surfaces, bonding at metal-oxide interfaces, and enhanced reactivity of nanoparticles. To allow the investigation of more complex systems and phenomena, we have developed new computationally efficient algorithms, e.g., self-consistent linear scaling density functional theory, and variable and real-space gridding.

Chemical Processes

We have extensive capabilities, including massively-parallel computation, to model complex chemically reacting flows such as occur in chemical vapor deposition manufacturing processes. Our numerical simulations can include the coupled gas-phase and gas-surface chemistry, fluid dynamics, heat, and mass transfer to provide predictive models of a chemical process.

Low-Temperature Plasmas

We have extensive capabilities in massively parallel codes to simulate the time and space evolution of low-temperature plasmas, focusing on new theoretical techniques for achieving rapid convergence and on direct comparisons with experimental results.

Optical and Wave Propagation

We have developed advanced simulation codes for understanding wave propagation in optical parametric oscillators and amplifiers for the purpose of designing highly efficient, tunable laser sources. We also have capabilities in novel optical designs, including resonators for compact laser geometries. These capabilities are coupled to in-house micro-optics construction facilities and state-of-the-art optics testing.

Physical & Chemical Sciences Center
FY99 Budget-By Customer

Physical & Chemical Sciences Center
FY99 Budget - By Customer

Capital ($1.7M)

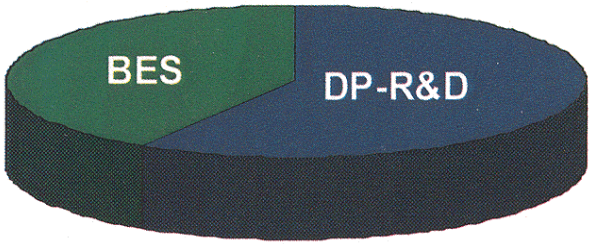

Operating ($32M)

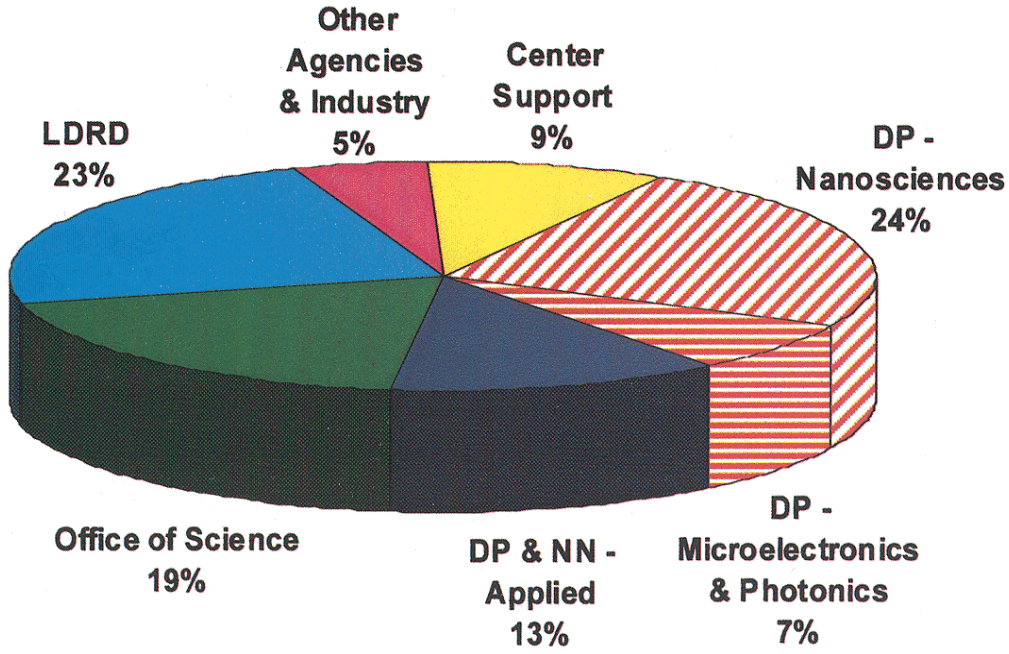

SAND99-0153: Prepared by Sandia National Laboratories, Albuquerque, New Mexico 87185 and Livermore, California 94550. Sandia is a multiprogram laboratory operated by Sandia Corporation, a Lockheed Martin Company, for the United States Department of Energy under Contract DE-AC04-94AL85000

Printed January 1999